Universiteit Gent
Faculteit Wetenschappen

First-principles study of radiation-induced radicals in solid-state amino acids and sugars: confrontation of density-functional calculations with experimental results.

Ewald Pauwels

Promotor: Prof. Dr. M. Waroquier

Proefschrift tot het verkrijgen van de graad van
Doctor in de Wetenschappen: scheikunde
Academiejaar 2003-2004

Contents

List of Figures

List of Tables

Chapter 1. General introduction

In this work, we present an extensive computational study of several radiation-induced radicals of biomolecules. In particular, two specific types of molecular systems will be highlighted: amino acids and sugars. Both systems are abundantly present in the natural world and are vital to the existence of life in all its forms. Amino acids are the building blocks of polypeptides and proteins, which are involved in nearly all biochemical processes. Sugars (or carbohydrates) also play a key role, not merely as sweeteners but rather as essential components in the biological energy storage and transport systems of animals and as chief structural material in plants.

As can be expected, the radical adducts of these compounds have an equal importance in biochemistry. These radicals can arise in chemical reactions or can be induced as the result of radiation damage. Such species are normally very short-living in gas phase or solution. In crystals on the other hand, the radicals become "trapped" inside the amino-acid or carbohydrate lattice and their reactivity will be sharply reduced. The solid state therefore offers the opportunity to extensively study the nature and structure of the (radiation-)induced organic radicals using various experimental techniques, of which Electron Paramagnetic Resonance spectroscopy (EPR) can be favoured as it can access an abundance of structural information about the radical. However, this technique does not provide the information as such, instead it has to be deduced from the EPR spectroscopic parameters, an analysis that is often complex and open to ambiguity.

In addition, the radiation chemistry of sugars and especially amino acids in the solid state is an elaborate field of study and requires a profound understanding of the different physical and chemical processes taking place inside the crystal. This area of interest has received considerable attention in view of interesting applications in EPR dosimetry. Within this respect, we refer to the success of the alanine dosimeter for reference- and routine dosimetry in radiation therapy, biological research and industrial high-dose irradiation facilities. However, it was only after the publication of a detailed EPR study on this amino acid that an enhanced understanding of its radiation chemistry was established. Three radical species were in this way identified as contributing significantly to the observed composite spectrum and hence also to the overall dosimetric characteristics of the alanine system.

As a result of the often-cumbersome analysis of the EPR parameters and the complexity of the associated radiation chemistry, the experimentalist is faced with a delicate task to propose appropriate models for the paramagnetic species present in the crystals. Over the last few years, it has become increasingly popular to rely on ab-initio molecular modeling techniques for this purpose. This success is in part due to the spectacular expansion of recent computer capabilities but is not in the least a result of the ongoing development of theoretical models and numerical algorithms in the field of quantum chemistry. Especially since the introduction of Density Functional Theory (DFT), a sharp quantitative as well as qualitative increase of theoretical calculations has been witnessed. The effectiveness of DFT can be largely attributed to a better incorporation of electron correlation as compared to more conventional ab-initio methods (such as e.g. Hartree Fock). Furthermore, this DFT algorithm does not require considerably more computer time as compared to conventional HF calculations but, in contrast, is significantly faster in comparison with other high-level correlation calculations (e.g. post HF), which renders it a very cost-effective method. Not only can these types of ab-initio calculations identify and verify proposed radical structures with the aid of optimization routines, predictions can also be made founded on entirely theoretical grounds. In addition, these methods offer the possibility to reproduce EPR quantities based on first principles. Evidently this presents a powerful tool to the experimentalist for the interpretation and analysis of EPR spectra. By now comparing measured and predicted spectroscopic parameters with each other, the true identity of an experimentally observed paramagnetic species can be linked directly to the structural characteristics of a theoretical model proposed for the specified radical.

In this work, we will specifically make use of the link with experiment to characterize the radiation-induced radicals of amino acids and sugars from a theoretical point of view. A general computational strategy is reported, which outlines a basic procedure for the theoretical treatment and simulation of radicals in a solid state. This strategy is composed of four main steps. In an initial step, one or more radical models are proposed that might be consistent with the experimental EPR data of an observed paramagnetic species. The structures of these radical models are subsequently optimized within a well-defined model space, in either a DFT or semi-empirical framework. A third step concerns the determination of EPR parameters for the optimized structures, adopting an ab-initio level of theory. The results of these EPR calculations can also be sensitive to the used model space. In the final step, a conclusive analysis between calculated and measured EPR parameters is then possible.

Applied on amino-acid and sugar systems, the drafted procedure will enable us to formulate specific conclusions with regard to the nature and identity of the radiation-induced radicals, on the condition that an appropriate approximation is made for the solid-state environment of the radical. The extent of the model space during the optimization and EPR calculations is therefore of particular importance. In this work, it is examined what effect the size of the model space and the applied level of theory have on the calculated structural and spectroscopic properties of a simulated radical. This is achieved by introducing several model space approaches – classified from "single molecule", over "cluster" to "periodic" – which incorporate an increasing amount of intermolecular interactions between the radical and its crystalline environment. Eventually, it is argued that the model space indeed plays a considerable role for the determination of a radical geometry and its associated EPR parameters. This aspect must therefore be carefully considered when initiating a computational study of radicals in the solid state.

This work is organized in two main sections. The first section contains chapters 2 to 4 and outlines the conceptual framework of this thesis. In chapter 2, a concise overview is presented of some general principles in molecular modeling that are relevant to this work. The subsequent chapter deals with the basic concepts and theory of EPR spectroscopy. In the fourth chapter, we will introduce a general computational strategy that will be followed in the applications-section to determine EPR parameters on theoretical grounds.

In the second, applied section (chapters 5 to 10), several investigations are made of radiation-induced radicals in solid-state systems. Chapters 5 and 6 deal with the amino-acid systems, alanine and glycine, respectively. After a general introduction into the applications and occurrence of radicals in sugar crystals (chapter 7), a report is given on the radicals in β-D-fructose (chapter 8), α-D-glucose (chapter 9) and α-L-sorbose (chapter 10). In the final chapter, some general conclusions are formulated.

Chapter 2. General principles of Molecular Modeling

GENERAL REFERENCES: [1], [2], [3], [4]

2.1 INTRODUCTION

Molecular systems consist of electrons and nuclei and the essence in quantum chemistry is to solve the Schrödinger equation for this system. Since we are interested in a static description of the molecular system, we can restrict ourselves to the time-independent, non-relativistic Schrödinger equation:

$$\hat{H}\left|\Phi\right\rangle = E\left|\Phi\right\rangle \tag{1}$$

The Hamilton operator $\hat{H}$ describes the different interactions between M nuclei and N electrons in a molecular system in the absence of external magnetic or electric fields:

$$\begin{aligned}\hat{H} = &-\frac{1}{2}\sum_{i=1}^{N}\hat{\nabla}_i^2 - \frac{1}{2}\sum_{A=1}^{M}\frac{\hat{\nabla}_A^2}{M_A} - \sum_{i=1}^{N}\sum_{A=1}^{M}\frac{Z_A}{r_{iA}} \\ &+\frac{1}{2}\sum_{i=1}^{N}\sum_{\substack{j=1 \\ i\neq j}}^{N}\frac{1}{r_{ij}} + \frac{1}{2}\sum_{A=1}^{M}\sum_{\substack{B=1 \\ A\neq B}}^{M}\frac{Z_A Z_B}{R_{AB}}\end{aligned} \tag{2}$$

The first two terms express the electronic and nuclear kinetic energy operators, respectively. The potential energy of the system is described by the last three terms, the nucleus-electron attraction (the external potential V_{ext}), and the electron-electron and nucleus-nucleus Coulomb interactions. In the above equation, $\hat{\nabla}_i^2$ and $\hat{\nabla}_A^2$ are the Laplacian differential operators with respect to the electronic and nuclear coordinates. M_A is the mass-ratio of nucleus A to the mass of an electron and Z_A is the atomic number of nucleus A.

If we take into consideration the significant difference in mass between electrons and nuclei (one proton weighs roughly 1800 times more than one electron), we can simplify the above Schrödinger equation by what is known as the Born-Oppenheimer approximation. This principle states that the electrons of a molecular system can be considered as moving in the field of fixed nuclei, since these move much slower due to their larger mass. This then reduces equation (2) to an electronic Hamiltonian:

$$\hat{H}_{elec} = -\frac{1}{2}\sum_{i=1}^{N}\hat{\nabla}_i^2 - \sum_{i=1}^{N}\sum_{A=1}^{M}\frac{Z_A}{r_{iA}} + \frac{1}{2}\sum_{i=1}^{N}\sum_{\substack{j=1 \\ i\neq j}}^{N}\frac{1}{r_{ij}} \tag{3}$$

and what remains is to solve the electronic Schrödinger equation:

$$\hat{H}_{elec}\left|\Psi_{elec}\right\rangle = E_{elec}\left|\Psi_{elec}\right\rangle \tag{4}$$

in which the electronic wavefunction Ψ_{elec} and energy E_{elec} depend parametrically on the nuclear coordinates and the associated external potential V_{ext}. To solve this equation, we must resort to the variational principle that the true energy E_0 of the ground state will be a lower bound to the expectation value of the Hamilton operator (which equals the "trial" energy) for a trial wavefunction:

$$\left\langle\Psi_{trial}\right|\hat{H}\left|\Psi_{trial}\right\rangle = E_{trial} \geq E_0 = \left\langle\Psi_0\right|\hat{H}\left|\Psi_0\right\rangle \tag{5}$$

So, in order to find the (electronic) ground-state energy corresponding to a set of nuclear coordinates, we need to minimize the energy as a functional of Ψ by searching through all possible (and acceptable) N-electron wave functions. It is of course impossible to search over all functions, and therefore the variational principle is usually restricted to a subset of possible functions; this implies another approximation (e.g. the use of Slater determinants in Hartree Fock). This subset is very often split up further in basis sets, which make the calculation of (two-electron) integrals faster and easier. The search itself is often performed self-consistently.

Once the electronic problem has been solved (or rather approximated), the total Hamiltonian is easily obtained and we get an energy value for the ensemble of nuclei generating the external potential V_{ext}. By iteratively solving the electronic Schrödinger equation for different coordinates of the nuclei, a potential energy surface is created for the molecular system under study. By expanding this surface, it is ideally possible to locate the absolute minimum, corresponding to the most stable molecular conformation. This optimization procedure is vital in molecular modeling. It allows us to postulate an initial guess for a molecular conformation which we can then optimise to a (local) minimum on the potential energy hypersurface. Only for these minimal conformations it is interesting to assess the molecular or nuclear properties, since they will determine the macroscopic observables of the system. As the validity of a calculated molecular conformation is determined by the solution of the electronic Schrödinger equation, we will now look in detail at different ways to approximate this solution.

2.2 OVERVIEW OF APPROXIMATE METHODS

As the title of this section reveals, there is no exact method to solve the electronic Schrödinger equation. Instead, there is a vast amount of approximate methods and the first job in molecular modeling is to choose a level of theory that is able to describe the molecular system of interest with as less computational effort as possible. For static solutions of the molecular systems, three main groups of methods can be identified.

(1) Molecular mechanics
(2) Ab-initio methods
(3) Semi-empirical methods

2.2.1 Molecular mechanics

The most crude approximation is simply to neglect any electronic effects. In that case, we end up with a purely classical system, in which the molecules are simplified to ensembles of interconnecting “balls” (nuclei) and “springs”. How the nuclei interact (the “springs”) is described by a force field, which comprises a set of potential energy functions describing all bonding and non-bonding interactions between atoms. The force field itself is a parametric function of only the nuclear coordinates and these parameters are fitted to experimental data. A plethora of different force fields exist, each often with specific parameter sets for different types of compounds. Some prominent and widely-used examples are the Amber [5] and MM2/MM3 [6] force fields. But even though some quantum chemical effects can be parameterised, molecular mechanics have hardly anything to do with quantum mechanics. Furthermore, the empirical input limits the general applicability of the method. It is mainly used to obtain geometries for extremely large (organic) molecular systems – such as polypeptides or polysaccharides – due to the high speed of these calculations. Spectroscopic properties or electronic effects can of course not be determined, although some efforts have been made to introduce force-field parameters for open-shell peptide residues [7].

2.2.2 Ab-initio methods

The Hartree-Fock approximation

In the Hartree-Fock approach, a first approximation is introduced in the search over all acceptable N-electron wave functions Ψ in equation (5). More specifically, the search is limited to a subset of functions that are antisymmetrised products of N one-electron wave functions $\chi_i\left(\overline{x}_i\right)$. These products are usually referred to as Slater determinants Φ_{SD}:

$$\Psi \approx \Phi_{SD}\left(\overline{x}_1,\overline{x}_2,\ldots\overline{x}_N\right) = \frac{1}{\sqrt{N!}}\begin{vmatrix} \chi_1\left(\overline{x}_1\right) & \chi_2\left(\overline{x}_1\right) & \cdots & \chi_N\left(\overline{x}_1\right) \\ \chi_1\left(\overline{x}_2\right) & \chi_2\left(\overline{x}_2\right) & \cdots & \chi_N\left(\overline{x}_2\right) \\ \vdots & \vdots & & \vdots \\ \chi_1\left(\overline{x}_N\right) & \chi_2\left(\overline{x}_N\right) & \cdots & \chi_N\left(\overline{x}_N\right) \end{vmatrix} \quad (6)$$

Since an electron is not only described by its spatial coordinates $\overline{r}_i$ but also by its spin coordinate s_i, the one-electron wave functions $\chi_k\left(\overline{x}_i\right)$ are called spin orbitals (or molecular orbitals) and they are composed of a spatial orbital $\phi_k\left(\overline{r}_i\right)$ and a spin function, $\alpha\left(s_i\right)$ or $\beta\left(s_i\right)$:

$$\chi_k\left(\overline{x}_i\right) = \begin{cases} \phi_k\left(\overline{r}_i\right)\cdot\alpha\left(s_i\right) \\ \phi_k\left(\overline{r}_i\right)\cdot\beta\left(s_i\right) \end{cases} \quad (7)$$

Slater determinants are antisymmetric, which means that they change sign when two electrons are interchanged:

$$\Phi_{SD}\left(\overline{x}_1,\overline{x}_2,\ldots\overline{x}_N\right) = -\Phi_{SD}\left(\overline{x}_2,\overline{x}_1,\ldots\overline{x}_N\right) \quad (8)$$

This is in fact a more general statement of the Pauli exclusion principle, which states that no two fermions are allowed to have the same spatial- and spin coordinates. Evidently, when $\overline{x}_1$ and $\overline{x}_2$ are equal in the above equation, the wave function must vanish.

Within the assumption that the wave function can be written as a single Slater determinant, the Hartree-Fock energy is obviously a functional of the N spin orbitals, and we again can apply the variational theorem. In order to minimize the energy, we vary the molecular orbitals subject to the constraint that they remain orthonormal:

$$\left\langle \chi_k \middle| \chi_l \right\rangle = \int \chi_k^*(\overline{x})\chi_l(\overline{x})\,d\overline{x} = \delta_{kl} \quad (9)$$

which introduces Lagrangian multipliers in the resulting N Hartree-Fock equations.

$$\hat{f}_i\left|\chi_k\right\rangle = \varepsilon_i\left|\chi_k\right\rangle \quad (10)$$

In these equations – which are solved in a self-consistent way – the multipliers ε_i represent the molecular orbital energies and the one-electron Fock operator $\hat{f}_i$ is defined as:

$$\hat{f}_i = -\frac{1}{2}\nabla_i^2 - \sum_{A=1}^{M}\frac{Z_A}{r_{iA}} + \upsilon_{HF}\left(\overline{x}_i\right) \quad (11)$$

with $\upsilon_{HF}\left(\overline{x}_i\right)$ the Hartree-Fock potential, representing the average potential that one electron is subject to due to all other electrons. This potential is composed of two parts, which can be best understood when considering an expectation value of the Hartree-Fock potential:

$$\begin{aligned}
&\left\langle \chi_k \middle| \upsilon_{HF}\left(\overline{x}_i\right) \middle| \chi_k \right\rangle \\
&= \sum_{l=1}^{N} \left[\underbrace{\int_j \left|\chi_k\left(\overline{x}_i\right)\right|^2 \frac{1}{r_{ij}} \left|\chi_l\left(\overline{x}_j\right)\right|^2 d\overline{x}_j}_{\text{Coulomb}} - \underbrace{\int_j \chi_k^*\left(\overline{x}_i\right)\chi_l^*\left(\overline{x}_j\right)\frac{1}{r_{ij}}\chi_k\left(\overline{x}_j\right)\chi_l\left(\overline{x}_i\right)d\overline{x}_j}_{\text{Exchange}} \right]
\end{aligned} \tag{12}$$

The Coulomb part in equation (12) represents the local contribution to the total electron interaction energy due to the electrostatic repulsion between electron i and the averaged charge density of all electrons in the molecular system. Exchange effects have no classical interpretation. In the resulting interaction, the variables are exchanged in the two spin orbitals χ_k and χ_l, which complicates matters since the expectation value for the i-th electron on spin orbital $\chi_k\left(\overline{x}_i\right)$ now depends on the value of $\chi_k\left(\overline{x}_j\right)$ over all space through the integrand $\overline{x}_j$. For this reason, the exchange interaction is called non-local. These so-called two-electron four-center integrals are difficult to solve and very time-consuming and are therefore prone to approximation. The resulting methodologies are termed semi-empirical and will be briefly treated in section 2.2.3. As exchange effects arise merely due to the antisymmetry prerequisite in Slater determinants, only electrons with parallel spins give rise to these effects. For electrons with antiparallel spins the integral vanishes.

Self-interaction does not occur in the Hartree-Fock scheme. This is obvious if we take $k = l$ in equation (12). The Coulomb integral then describes the interaction of an electron with itself, which is clearly nonsense. The problem is elegantly solved however, since for $k = l$, the exchange integral cancels out the Coulomb integral exactly.

HF correlation and higher order methods

Due to the different approximations introduced, the Hartree-Fock ground-state energy of a molecular system will never be equal to the exact energy E_{exact} of the system. According to the variational principle, E_{HF} will always be higher. The remainder part E_{corr}

$$E_{corr} = E_{exact} - E_{HF}$$

is called the correlation energy and can be considered as a measure for the error introduced through the approximations inherent to the HF scheme. The lack of electron correlation in HF is mainly the result of the only average treatment of electron-electron interaction (via υ_{HF}). Unfortunately, electron correlation effects (sometimes called "nature's glue" [8]) are often very important in the treatment of molecular systems.

To deal with this problem, a variety of wave function based computational schemes have been introduced, among which Moller-Plesset (MP2-4), Configuration Interaction (CI) or Coupled Cluster (CC) treatments are probably the most popular. An in-depth description of these methods is beyond the scope of this work and we refer to [1] for a more detailed description. Most of the higher order methods fall back on perturbation theory and therefore produce correction terms to the Hartree-Fock energy. This perturbative approach, although it often delivers (more) correct energies, is extremely expensive in computer time, since both the HF and higher order routines have to be processed.

Density Functional Theory (DFT)

GENERAL REFERENCES: [9], [10], [11], [12], [13]

The main problem with wavefunction-based theories is that calculations are very extensive. The fact that, for an N electron molecular system, Ψ depends on 3N spatial and N spin variables, makes these methods extremely time-consuming (and therefore expensive in computer time) if adequate accuracy is to be expected for large molecular systems. The basis of Density Functional Theory is to replace this complicated wavefunction by a much simpler quantity, the one particle electron density $\rho(\bar{r})$. This in fact reduces the number of variables to only 3 spatial variables, with the result that DFT 'in se' offers a more cost-effective treatment of electron correlation than Hartree-Fock and its systematic perturbative improvements.

The transition to a density-based method comes of course at a price: practically, all information about excited states is lost! However, we lose no information about ground-state properties and this is exactly what we are interested in for a time-independent, static description of molecular systems. The only thing we have to do to determine the energy or other properties of the molecular system, is to express them as a functional of the electron density. This density is defined as a multiplicative integral over the spin coordinates of all electrons and over the spatial variables of all but one electron:

$$\rho\left(\bar{r}_i\right) = N\int d\bar{x}_1 \int d\bar{x}_2 \ldots \int d\bar{x}_{i-1} \int ds_i \int d\bar{x}_{i+1} \ldots \int d\bar{x}_N \left|\Psi\left(\bar{x}_1, \bar{x}_2 \ldots \bar{x}_N\right)\right|^2 \tag{13}$$

which represents the probability of finding any electron with arbitrary spin at position $\bar{r}_i$. Historically, Thomas and Fermi [14] were the first to express the ground-state energy of a system as a functional of $\rho\left(\bar{r}\right)$. Their approach, dating back to 1927, was mainly aimed at solid-state physics and will be briefly discussed later on.

The Hohenberg-Kohn theorems

The main breakthrough of DFT came about when Hohenberg and Kohn published the proofs of two theorems [15]. These "Hohenberg-Kohn theorems" – as they are commonly called – are the basis on which all of modern density functional theory is founded. In the next section, these theorems and their implications are briefly discussed. For more elaborate treatments on this subject, we integrally refer to standard works [9, 13].

The first HK theorem

The first theorem actually provides the proof that the electron density uniquely determines the ground-state properties of a (molecular) system. In other words, it proofs the validity of the switch from wavefunction to electron density, when dealing with the ground state.

If we rewrite the electronic Hamiltonian in equation (3) as:

$$\hat{H} = \hat{T} + \hat{V}_{Ne} + \hat{V}_{ee} \tag{14}$$

with $\hat{T}$ the kinetic electron energy operator, $\hat{V}_{ee}$ the electron-electron interaction operator and $\hat{V}_{Ne}$ the operator for the external (observable) potential $V_{ext}\left(\bar{r}\right)$, it is clear that through the Schrödinger equation for the (non-degenerate) ground state:

$$\hat{H}\left|\Psi_0\right\rangle = E_0\left|\Psi_0\right\rangle \tag{15}$$

the wavefunction Ψ_0 and consequently the energy E_0 for the ground state are exclusively dependent on the external potential $V_{ext}\left(\bar{r}\right)$. We summarize this by:

$$V_{ext} \Leftrightarrow \Psi_0 \Leftrightarrow E_0 \tag{16}$$

The first Hohenberg-Kohn theorem now states that the ground-state density $\rho_0\left(\bar{r}\right)$ uniquely determines the external potential $V_{ext}\left(\bar{r}\right)$, which – considering equation (16) – amounts to:

$$\rho_0 \Leftrightarrow V_{ext} \Leftrightarrow \Psi_0 \Leftrightarrow E_0 \tag{17}$$

This implies that Ψ_0 and E_0 are functionals of the electron density and we rewrite the expression for the ground-state energy:

$$\begin{aligned} E_0[\rho_0] &= \langle \Psi_0[\rho_0] | \hat{H} | \Psi_0[\rho_0] \rangle \\ &= \langle \Psi_0[\rho_0] | \hat{V}_{Ne} | \Psi_0[\rho_0] \rangle + \langle \Psi_0[\rho_0] | \hat{T} + \hat{V}_{ee} | \Psi_0[\rho_0] \rangle \\ &= \int \rho_0(\bar{r}) V_{ext}(\bar{r}) d\bar{r} + F_{HK}[\rho_0] \end{aligned} \tag{18}$$

The first term in the above equation represents the interaction between the electrons and the external field generated by the nuclei in the molecular system (optionally it also includes contributions due to other external fields, either electric or magnetic). This term obviously depends on the actual system at hand. The second term, however, is system independent and is called the (universal) Hohenberg-Kohn functional, often divided into a functional for the electronic kinetic energy $T[\rho_0]$ and one for the electron-electron interaction $E_{ee}[\rho_0]$:

$$F_{HK}[\rho_0] = T[\rho_0] + E_{ee}[\rho_0] \tag{19}$$

The $E_{ee}[\rho_0]$ functional can be further divided into the classical Coulomb part $J[\rho]$, which is known exactly, and a remaining non-classical functional $E_{nCl}[\rho]$.

The second HK theorem

The second Hohenberg-Kohn theorem simply states that the energy functional $E[\rho_{trial}]$ for a trial density ρ_{trial} will yield an energy for the (molecular) system that is upper bound to the true ground-state energy $E_0[\rho_0]$ of that system:

$$\langle \Psi_{trial} | \hat{H} | \Psi_{trial} \rangle = E[\rho_{trial}] \geq E_0[\rho_0] = \langle \Psi_0 | \hat{H} | \Psi_0 \rangle \tag{20}$$

This is obviously an adaptation of the variational procedure discussed earlier (equation (5)). Evidently, if we were able to search over all allowed antisymmetric wave functions, the trial function that yields the lowest expectation value for equation (20) would be the ground-state wave function. This "constrained search" approach would – in principle – allow us to solve the electronic many body problem exactly. Unfortunately only in principle because, even though these theorems prove that there is a unique mapping between the ground-state density and the ground-state energy, they do not tell us what the energy functional looks like or how it can be constructed. More specifically, the big unknown in equation (18) is the Hohenberg-Kohn functional $F_{HK}[\rho_0]$, in which the form of both $T[\rho_0]$ and $E_{ee}[\rho_0]$ is a mystery. For DFT to have any practical use, these functionals have to be approximated. Another, rather practical problem emerges in connection with the constrained-search approach. It explicitly specifies to search over all possible wave functions, which is obviously impossible.

The Kohn-Sham approach

In short, the variational principle and the constrained-search scheme are only of theoretical value and present no feasible solution to get to the ground state. Shortly after the Hohenberg-Kohn publication, however, an approach was developed that elegantly bypassed these problems. In 1965, Kohn and Sham functionalized DFT by introducing orbitals and a self-consistency scheme to approximate the kinetic energy functional [16].

The essence of this approach is to link the real N-electron molecular system with a fictitious system of N non-interacting electrons. For such a fictitious system, subject to an external potential $V_S\left(\bar{r}\right)$, the Hamiltonian is simply:

$$\hat{H}_S = -\frac{1}{2}\sum_{i=1}^{N}\hat{\nabla}_i^2 + \sum_{i=1}^{N}\hat{V}_{Si}$$

which obviously contains no electron-electron interactions. In analogy with equation (6), the wavefunction that satisfies the Schrödinger equation for this Hamiltonian can be written as a Slater determinant constructed of N spin orbitals or Kohn-Sham (KS) orbitals φ_i, that are determined by the N one-electron eigenvalue equations:

$$\left[-\frac{1}{2}\hat{\nabla}^2 + \hat{V}_S\right]\varphi_i = \varepsilon_i\varphi_i \tag{21}$$

Using these orbitals, we can construct the exact kinetic energy functional for this non-interacting system:

$$T_S = -\frac{1}{2}\sum_{i=1}^{N}\left\langle\varphi_i\left|\nabla^2\right|\varphi_i\right\rangle \tag{22}$$

Since the expression for this functional is known, Kohn and Sham suggested to use (22) as a first approximate for the real kinetic energy of the interacting system. This is only allowed if we choose the external potential $V_S\left(\bar{r}\right)$ such that the electron density of the non-interacting system is mapped exactly onto the ground-state density of the real system.

$$\rho_S\left(\bar{r}\right) = \sum_{i=1}^{N}\left|\varphi_i\left(\bar{r}\right)\right|^2 = \rho_0\left(\bar{r}\right)$$

The Hohenberg-Kohn functional (19) can then be rewritten as:

$$\begin{aligned} F_{HK}\left[\rho\right] &= T_S\left[\rho\right] + T_C\left[\rho\right] + E_{nCl}\left[\rho\right] + J\left[\rho\right] \\ &= T_S\left[\rho\right] + J\left[\rho\right] + E_{XC}\left[\rho\right] \end{aligned}$$

where $T_C\left[\rho\right]$, the residual part of the true kinetic energy, is taken up in the so-called exchange-correlation energy functional $E_{XC}\left[\rho\right]$, along with $E_{nCl}\left[\rho\right]$. Thus, the bypass of the non-interacting system has led to an energy functional that can be expressed as a function of the KS orbitals:

$$\begin{aligned} E\left[\rho\right] = & -\frac{1}{2}\sum_{i=1}^{N}\left\langle\varphi_i\left|\nabla^2\right|\varphi_i\right\rangle \\ & +\frac{1}{2}\sum_{i=1}^{N}\sum_{j=1}^{N}\int_a\int_b\left|\varphi_i\left(\overline{r}_a\right)\right|^2\frac{1}{r_{ab}}\left|\varphi_i\left(\overline{r}_b\right)\right|^2 d\overline{r}_a d\overline{r}_b \\ & +E_{XC}\left[\rho\right]-\sum_{i=1}^{N}\int_a\sum_{A=1}^{M}\frac{Z_A}{r_{aA}}\left|\varphi_i\left(\overline{r}_a\right)\right|^2 d\overline{r}_a \end{aligned} \tag{23}$$

We can now minimise this energy functional by varying the orbitals, which results in N Kohn-Sham equations:

$$\left[-\frac{1}{2}\hat{\nabla}^2+\underbrace{\left(\int_b\frac{\rho\left(\overline{r}_b\right)}{r_{ab}}d\overline{r}_b+V_{XC}\left(\overline{r}_a\right)-\sum_{A=1}^{M}\frac{Z_A}{r_{aA}}\right)}_{\hat{V}_{eff}}\right]\varphi_i=\varepsilon_i\varphi_i \tag{24}$$

where the effective potential $V_{eff}\left(\overline{r}\right)$ simply is the external potential $V_S\left(\overline{r}\right)$ for the non-interacting system of electrons that we have introduced earlier, as is obvious by comparing equations (21) and (24). This clears the path for a self-consistent scheme:

$$\begin{tikzcd} V_S\left(trial\right) \arrow[r] & \left\{\varphi_i\left(trial\right)\right\} \arrow[r] & E\left(trial\right) \arrow[r] & V_{eff}\left(trial\right) \arrow[lll, bend left] \end{tikzcd}$$

Introducing a trial external potential for the non-interacting system, the KS orbitals can be determined through equation (21) and so the density and energy. From the minimization procedure of the energy (23), we can then deduce the effective potential which we reinsert as a new trial external potential. This self-consistent scheme would ultimately provide us with the ground-state energy and electron density for the molecular system, if only the functional form of the exchange-correlation contribution $E_{XC}\left[\rho\right]$ were known. Therefore, again, considered approximations have to be used.

The Functional Zoo

Constructing an approximation for $E_{XC}\left[\rho\right]$ is quite difficult, since it is simply not known what the functional form looks like. Furthermore, this functional must contain a residual kinetic energy part along with the exchange and correlation. As a consequence, better functionals are mainly found by trial-and-error based on physical grounds (and intuition). However, two overall approaches can be discerned for the construction of an exchange correlation functional [17].

Non-empirical approach

Improved functionals are derived by imposing several known exact physical constraints on approximate functionals. Examples of these constraints are e.g. the requirement that the exchange correlation energy is always negative, sum rules for exchange correlation holes, etc.

The resulting functional that satisfies these boundary conditions, is indeed better, although mostly from a purely theoretical point of view only. This does not necessarily mean that they will also give accurate results for specific (molecular) systems within an approximate density functional framework.

Semi-empirical approach

Existing functionals are adapted or new ones constructed to contain parameter sets. These parameterized functionals can then be fitted to exactly known data, such as energies, ionization potentials, … which were determined from experiment or high-level calculation (e.g. Coupled Cluster). Although the resulting functionals will not seldom violate the boundary conditions mentioned earlier, they will often perform better on accuracy, especially for those systems they were fitted to. For chemical systems, this approach is frequently the most successful, since it can draw on the physical improvements of the "non-empirical" approach and add a parameterization, which ensures practical applicability.

Jacob's ladder of approximations

On a conceptual level, a plethora of approximations for $E_{XC}\left[\rho\right]$ has been formulated, obtained through the above approaches. To classify this ever-increasing "Functional Zoo" [8], a useful scheme was introduced by J. Perdew which comprises the better part of all functionals [18]. By analogy with a biblical story, this "Jacob's ladder" of approximations extends up to quantum chemical "heaven", being a functional with chemical accuracy. The rungs along the ladder represent the various approximations, each rung improving the properties and accuracy of the lower rungs, but also increasing the computational cost. A pictorial overview of this concept is given in Figure 2.1:

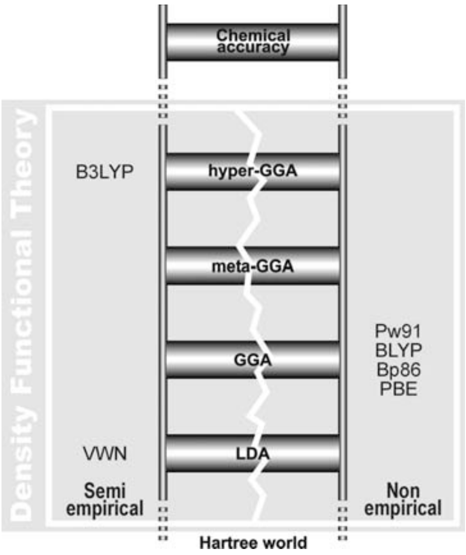

Figure 2.1: “Jacob’s ladder” according to Perdew.

LDA

The lowest rung on the ladder (above the Hartree world) is the Local Density Approximation (LDA). It is the chronologically first, and most elementary model, adapted from the early work of Thomas and Fermi [14]. These researchers formulated a quantum statistical model for simple solid-states (e.g. metals), based on the idea of a hypothetical uniform electron gas. In such a system, the electrons move on a homogeneous positive background charge distribution, such that the total charge of the system is neutral. By extension, a general form was derived for the LDA exchange correlation functional:

$$E_{XC}^{LDA}\left[\rho\right]=\int\rho\left(\bar{r}\right)\varepsilon_{XC}\left(\rho\right)d\bar{r} \tag{25}$$

where $\varepsilon_{XC}\left(\rho\left(\bar{r}\right)\right)$ indicates the exchange and correlation energy per particle of a uniform electron gas of density $\rho\left(\bar{r}\right)$. The LDA scheme implies that each electron interacts with the other electrons as though they would generate a completely homogeneous density and therefore $\varepsilon_{XC}\left(\rho\left(\bar{r}\right)\right)$ is only dependent on the local density for each electron. Various analytical expressions have been proposed for ε_{XC}, often based on (semi-empirical) parameterizations. Perhaps the most widely used is that of the VWN functional, developed by Vosko, Wilk and Nusair [19].

Even though this approximation holds for systems with a locally uniform or slowly-varying electron density (such as various inorganic solids), most chemical systems are characterized by rapidly varying densities. The only moderate accuracy of LDA is therefore clearly insufficient for most applications in chemistry.

Nevertheless it is used as a starting point for other approximate methods, by adding various other local contributions to ε_{XC}.

GGA

Higher on the ladder is the Generalized Gradient Approximation (GGA). In this class of functionals, the inhomogeneity of actual electron systems is approximated to first order by carefully adding information about the local gradient of the density $\nabla\rho$ in equation (25):

$$E_{XC}^{GGA}\left[\rho\right]=\int\rho\left(\overline{r}\right)\varepsilon_{XC}\left(\rho,\nabla\rho\right)d\overline{r} \tag{26}$$

GGA's offer better accuracy for chemical systems than LDA since they account for the non-homogeneity of the electron density to some degree. Some prominent examples are the PW91 [20], BLYP [21, 22], BP86 [23, 24, 25] or PBE [26] (non-empirical) functionals.

meta-GGA

In the Meta-Generalized Gradient Approximation, the integrand in equation (26) is further extended to include additional semi-local information:

$$E_{XC}^{meta-GGA}\left[\rho\right]=\int\rho\left(\overline{r}\right)\varepsilon_{XC}\left(\rho,\nabla\rho,\tau\right)d\overline{r} \tag{27}$$

with

$$\tau\left(\overline{r}\right)=\sum_{i}^{occupied}\left|\nabla\varphi_i\left(\overline{r}\right)\right|^2$$

the Kohn-Sham kinetic energy density as a more efficient alternative for the Laplacian of the density $\nabla^2\rho$.

Meta-GGA functionals are not often applied to study chemical systems but are rather considered as a step-up for the construction of other universal functionals (higher rungs on Jacob's ladder). Applications are therefore mostly situated in purely theoretical systems, although some recent studies have focused on more chemical systems [27].

hyper-GGA

On the fourth rung of Jacob's ladder, exact exchange is introduced in the functional. This seems straightforward, since it is possible to calculate the exact exchange contribution to the energy via an adaptation of the Hartree-Fock equation (equation (12)) that fits within the Kohn-Sham scheme. One could then naively construct an exchange-correlation functional, where only the correlation contribution to the energy is expressed through an approximate functional:

$$E_{XC}=E_X^{exact}+E_C$$

Unfortunately, this approach does not perform well for molecular systems, which illustrates that the separation of E_{XC} in an exchange and correlation part is totally artificial and that in fact a cancellation of errors occurs for (meta-)GGA's between the exchange and correlation contributions.

A subset of functionals – known as hybrid functionals – rely on an adaptation of the hyper-GGA principle that does perform well. As a consequence, they are highly popular and widely used with success. The key concept here is to include only a certain amount of exact (HF) exchange besides the built-in (DFT) exchange in the functional (hence the term hybrid). Exactly how much exchange of both is included is determined by semi-empirical parameters, as illustrated in the expression for the popular B3LYP functional [28], which depends on 3 parameters:

$$E_{XC}^{B3LYP} = \left(1-a\right)E_X^{LDA} + aE_X^{exact} + bE_X^{B88} + cE_C^{LYP} + \left(1-c\right)E_C^{LDA}$$

This functional contains contributions from various existing exchange and correlation (DFT) functionals, apart from an amount of exact (HF) exchange. The fact that the values of the parameters were optimized on a large set of molecules, makes this functional very successful for molecular systems. Throughout this work, we will therefore often fall back on B3LYP.

Summary

It is clear from the sections above that DFT is a very useful theory which does provide us with a functional tool to do quantum chemistry. A lot of problems are still associated with the construction of the functional $E_{XC}\left[\rho\right]$, which is probably the most delicate point in the theory. Things like self-interaction, semi-empirical fittings and the mere fact that we do not know what the exchange-correlation functional looks like, deserve an ungoing study. It is also clear that this theory is far from complete and other ab-initio theories (e.g. DMFT, see [13]) have been proposed to solve several problems in DFT. Surely, more accurate computational schemes exist (e.g. Coupled-Cluster methods), but DFT offers the most cost-effective incorporation of electron correlation. Therefore, up till now (and presumably for a long time to come), DFT is the method of choice that allows quantum chemists to accurately study molecular and chemical systems in an acceptable timeframe.

Basis sets

Since almost all quantum chemical ab-initio methods are based on self-consistent schemes, we must be able to obtain a relatively good initial trial wavefunction to start the iterative process with. Usually, a linear combination of atomic orbitals (LCAO) is chosen as a first approximation to the molecular orbitals, which is then gradually improved self-consistently. Either way, the molecular orbitals are expanded in a so-called basis set of L initial, predefined functions η_μ :

$$\left|\chi_i\right\rangle = \sum_{\mu=1}^{L} C_{\mu i}\eta_\mu \qquad (28)$$

This effectively reduces the solution of the Hartree-Fock or Kohn-Sham equations to calculating the coefficients $C_{\mu i}$, being the only variables left.

If the basis set were complete (i.e. $L = \infty$), every possible function $\left|\chi_i\right\rangle$ could be expressed exactly through equation (28). In reality, L is finite and we must carefully chose the number and form of the η_μ basis functions. Two types of basis functions have found common use, known as Slater type orbitals (STO) or Gaussian type orbitals (GTO). While some ab-initio packages – such as the Amsterdam Density Functional program (ADF) [29] – rely on STO orbitals, most programs (e.g. Gaussian98 [30] or Gaussian03 [31]) use contracted GTO basis sets. These are usually referred to with a cryptic shorthand, such as: 3-21G, 6-31G*, cc-pVQZ, etc.

For the calculations with the Gaussian software package in this work, we will mainly rely on the double-ζ 6-31G** [32] and triple-ζ 6-311G*(*) [33] basis sets. Both are in fact split-valence sets, in which the core orbitals are described by one contraction each of six primitive Gaussian functions, while more contractions are considered to treat the valence shells. In the case of the 6-311G** basis for instance, there are three contractions of 3, 1 and 1 primitives, respectively, augmented with additional polarization functions (**). In some cases, the EPR-III basis set will be used, which was specifically designed by Barone for the calculation of hyperfine coupling constants with DFT methods [34]. In essence, it is also a triple-ζ set augmented with diffuse and polarization functions (including d and f type functions). Its functionality however is largely due to an enhancement of the s-part describing the core region: 8 contractions of Gaussian primitives in total. This would make this basis set very suitable to calculate hyperfine coupling constants, since these depend directly on the unpaired spin density at the nucleus, as will be mentioned later on (see Chapter 3). Unfortunately, the vast size of the basis goes along with an expensive computational cost.

2.2.3 Semi-empirical methods

Semi-empirical methods can be situated on an intermediate level between ab-initio and purely empirical methodologies (e.g. force fields). In general, they rely on a kernel based on ab-initio theory, in which (often severe) approximations are introduced, complemented with empirical input. As a result, these approximate methods are considerably faster than pure ab-initio calculations and sometimes even more accurate, due to the incorporation of parameters derived from experimental data. However, they lack a general applicability and can sometimes lead to serious errors, as will become apparent later on.

The semi-empirical formalisms that are applied in this work invariably rely on a simplified Hartree-Fock Hamiltonian that is solved self-consistently, but in which only valence electrons are considered. All other electrons are accounted for in a "nuclear core" contribution that does not influence chemical bonding. Limited basis sets comprising Slater-type functions are used, but only s- and p-type orbitals are employed. More specifically, we will make use of the AM1 (Austin Model 1) [35] and PM3 [36] methods. Both are alternative parameterizations of the MNDO scheme (Modified Neglect of Diatomic Overlap) which, in turn, falls back on the NDDO (Neglect of Diatomic Differential Overlap). This last approximation means that differential overlap is neglected between atomic orbitals that are centered on different atoms:

$$\int \eta_r^*\left(\bar{x}_1\right)\eta_s\left(\bar{x}_1\right)d\bar{x}_1 = 0$$

if η_r and η_s are on different atoms. Hence, NDDO effectively ignores all three- and four-center integrals resulting from (12). MNDO, AM1 and PM3 are mere adaptations of this scheme, in which mono-atomic parameters have been introduced. In addition, the remaining two- and one-center integrals are evaluated using approximate means, speeding up calculations tremendously. In AM1 (and MNDO) the values for these integrals are derived from atomic spectra, while in PM3 they are treated as an additional set of parameters and optimized to reproduce experimental molecular properties.

We further refer to [37] for an elaborate discussion of these and other semi-empirical methods.

Chapter 3. Electron Paramagnetic Resonance

Probably the best method to study the chemical and structural nature of (organic) radicals is Electron Paramagnetic Resonance spectroscopy (EPR). In this section, we will discuss some relevant topics on this matter but we integrally refer to standard works for an in-depth treatment [38, 39, 40, 41, 42].

3.1 INTRODUCTION – RESONANCE CONDITION

Even though the first EPR spectrum was made in 1945 by Zavoisky [43], the basis of the technique hinges on the much earlier discovery of an odd electron property known as spin. After the Stern-Gerlach [44] experiment and the work of Goudsmit and Uhlenbeck [45], it was recognised in the early 1920s that the electron was to have some sort of intrinsic angular momentum. Classically, this could be depicted as though the electron would rotate about its own axis. Quantum mechanically, the magnitude of the electron spin is defined through the observables $S(S+1)$ and M_S, associated respectively with the spin angular momentum operator $\hat{\bar{S}}^2$ and its projected operator $\hat{S}_Z$ along an arbitrary direction of quantization. This is represented in the following eigenvalue equations for the wavefunction $\chi_{M_S}^S$

$$\begin{aligned} \hat{\bar{S}}^2\chi_{M_S}^S &= S(S+1)\chi_{M_S}^S \\ \hat{S}_z\,\chi_{M_S}^S &= M_S\,\chi_{M_S}^S \end{aligned} \tag{29}$$

where M_S can take on the values ranging from $-S$ to $+S$. As a consequence of this angular momentum, a magnetic spinmoment $\hat{\bar{\mu}}_S$ arises for the electron:

$$\hat{\bar{\mu}}_S = -g_e\beta_e\hat{\bar{S}}$$

with g_e the free electron g-value (2.0023) and β_e the Bohr magneton. If now this electron is placed in a magnetic field $\bar{B}$, the spinmoment will interact:

$$\begin{aligned} E &= \left\langle \chi_{M_S}^S \middle| -\hat{\bar{\mu}}_S\cdot\bar{B} \middle| \chi_{M_S}^S \right\rangle \\ &= g_e\beta_e M_S B \end{aligned}$$

and the introduction of a direction of quantization (along $\overline{B}$) lifts the degeneracy of the $\hat{S}_Z$ operator. Since $S = \frac{1}{2}$ for the electron, two spinstates result from this Zeeman splitting corresponding with $M_S = +\frac{1}{2}$ (α- or spin-up state) and $M_S = -\frac{1}{2}$ (β- or spin-down state), separated by an energy difference ΔE that increases with the field strength $B = \left\|\hat{\overline{B}}\right\|$, as illustrated in Figure 3.1.

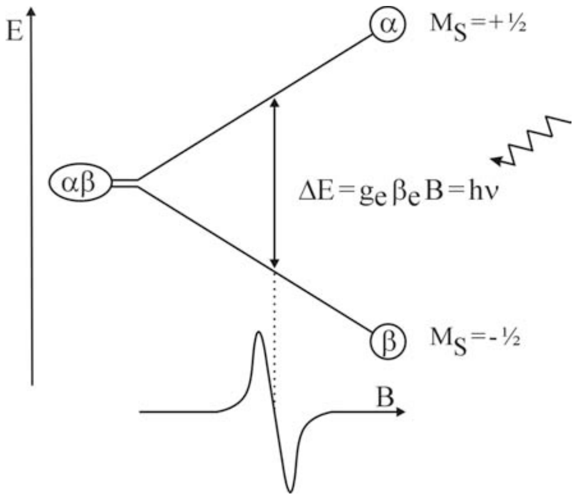

Figure 3.1: Resonance condition for a free electron.

A transition from the lower β- to the higher α-state can be induced by an electromagnetic field (perpendicular to the direction of the magnetic field) whose energy quanta $h\nu$ match the energy gap ΔE:

$$\Delta E = g_e \beta_e B = h\nu \tag{30}$$

This resonance condition can, in principle, be met in two ways:

- by applying a constant magnetic field and varying the frequency ν of the electromagnetic field
- by subjecting the electron to an electromagnetic field with constant frequency an varying the magnitude B of the applied magnetic field.

As most EPR experiments are carried out with electromagnetic field frequencies within the microwave region, the latter method is most often used for practical reasons. When a magnetic field sweep is performed within this regime, an absorption in microwave power is observed when the electron is in resonance with the electromagnetic field. This absorptive peak is recorded in a first derivative spectrum, as illustrated in Figure 3.1.

3.2 OVERVIEW OF AN EPR SPECTROMETER

A typical setup to perform continuous-wave EPR experiments is shown in Figure 3.2. It basically consists of a frequency-stable microwave source (in the figure, a "klystron"), a resonant cavity, which contains the sample, a magnet that is capable to produce an adjustable, but homogeneous magnetic field and a detection device to monitor and record the energy absorption in the EPR spectrum.

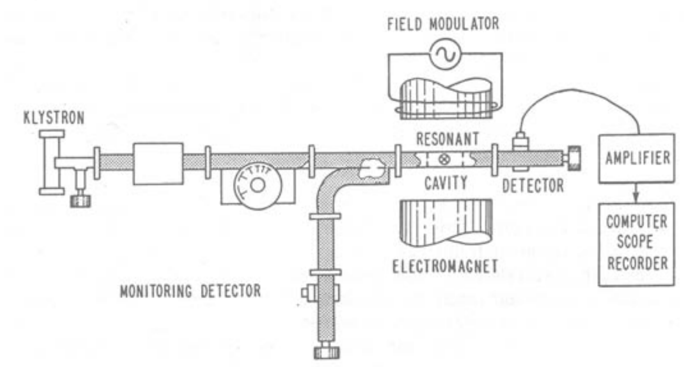

Figure 3.2: Block diagram of a continuous wave electron paramagnetic resonance spectrometer (after Weil et al. [**41**]).

Experiments can be performed at various frequencies, commonly called microwave bands. Some of the most used are the X-band (9.5 GHz), Q-band (35 GHz) and W-band (95 GHz). Even though higher frequencies offer more sensitivity and better resolution, they impose severe restrictions on the dimensions of the resonant cavity, which is specifically designed to match the microwave wavelength to build up a standing wave pattern in it. A permanent magnetic field is applied perpendicular to the direction of the microwave field wave guide and is made adjustable by additional electromagnetic coils. Typical field values range from 820 mT for K-band to 3.4 T in W-band (for g=2). As the magnetic field is swept, microwave power absorption will occur in the cavity at the resonant field value. A mismatch between wave-guide and cavity results in reflection of microwave power, which is registered in the monitoring detector, passing through a directional coupler.

3.3 GENERAL HAMILTONIAN

In the case of a free electron, its spin magnetic moment would indeed only interact with the external magnetic field. In a (paramagnetic) molecular system however, several electrons and nuclei are present, which will all interact with the field and with each other, leading to various interaction effects that have to be considered. To further complicate things, as the electrons will move in the field of nuclei, an additional magnetic moment $\hat{\mu}_L$ can be associated with the orbital momentum $\hat{L}$ of the electron:

$$\hat{\mu}_L = -\beta_e \hat{L}$$

This moment interacts with the spin moment through the so-called spin-orbit coupling interaction:

$$\hat{H}_{SO} = \lambda \hat{L} \cdot \hat{S}$$

which can be considered as an added perturbative term to the electronic Hamiltonian (with λ the spin-orbit coupling constant). This energy term will cause only the total electronic angular momentum $\hat{J} = \hat{L} + \hat{S}$ to be an observable. Within the Russell-Saunders coupling scheme, the magnetic moment $\hat{\mu}_L$ must then be combined with the spin moment $\hat{\mu}_S$ to form a resultant effective electron spin magnetic moment $\hat{\mu}_J$:

$$\hat{\mu}_J = \hat{\mu}_L + \hat{\mu}_S = -\beta_e \left(\hat{L} + g_e \hat{S} \right) = -\beta_e g_J \hat{J} \qquad (31)$$

In fact, it is this $\hat{\mu}_J$ operator that should have been used in the above discussion of the Zeeman splitting and it is the effective g_J factor – usually just slightly different from the ideal g_e – that is observed in experiments. But since we were then dealing with a non-interacting electron, the quantum number L would be 0 for $\hat{L}$, and $\hat{\mu}_J$ simply equaled $\hat{\mu}_S$.

Nevertheless, for other systems, higher multiplicities would be possible, ranging from $|L - S|$ to $L + S$. In the systems that will be discussed in this work, strong crystal fields or covalent bonds are present that will lift the orbital degeneracy (formally $2L+1$), leaving orbital sub-states that are widely separated as compared to normal Zeeman splittings. Consequently, no EPR transitions will be induced between these energy levels. The orbital ground state in these systems will usually be non-degenerate, in which only the electron spin is allowed to become oriented in the applied field, with resolvable components $M_S = \pm \frac{1}{2}$. This is illustrated for the three p orbitals (*L=1* so *2L+1=3*-fold degenerate) of carbon in a $^{\bullet}CH_3$ radical in Figure 3.3.

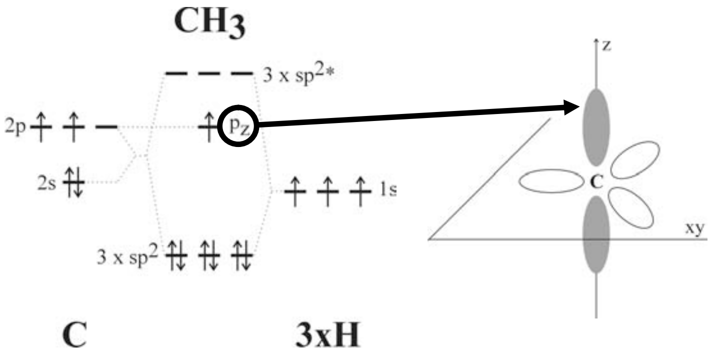

Figure 3.3: The covalent bond of carbon with the three hydrogens, gives rise to three bonding sp^2 orbitals, three antibonding sp^{2*} orbitals and one non-bonding orbital p_z. The unpaired electron is localised on the latter orbital, giving rise to a single EPR transition, similar to that of Figure 3.1.

This "a priori" treatment of $\hat{L}$ quenches the effects of orbital momentum and as a result only one EPR transition is taken into account. Even though this approach succeeds in simplifying the complicated coupling scheme, (molecular) systems exist for which it does not hold. Furthermore, various other interactions between electron and nuclear spin- and orbital- magnetic moments are left unaccounted for.

For the proper construction of a Hamiltonian and to unambiguously account for all interactions taking place, we must start from a relativistic treatment of a many-particle (molecular) system in the presence of a magnetic field, since only in the relativistic Dirac equation electron (and nuclear) spin is explicitly introduced. Unfortunately, no fully satisfactory relativistic Hamiltonian has been derived yet, and therefore a perturbative approach to the problem is traditionally used, in which the unperturbed, non-relativistic Hamiltonian $\hat{H}^0$ (see equation (2)) is expanded with additional operators (summed up in $\hat{H}'$) to account for relativistic properties:

$$\hat{H} = \hat{H}^0 + \hat{H}' \tag{32}$$

In addition, the effect of the magnetic field must also be taken up. This is best achieved by expressing the Hamiltonian in terms of the vector potential $\overline{A}$, associated with the magnetic field through:

$$\overline{A} = \frac{1}{2}\left(\overline{B} \times \overline{r}\right)$$

The electron experiences extra momentum due to this magnetic field and the resulting total electron momentum

$$\overline{p} \to \overline{p} + \frac{e}{c}\overline{A}$$

is reinserted in the electronic kinetic energy part of the Hamiltonian (the first term of equation (2)). The complete expansion of this “minimal substitution” on an approximated relativistic Hamiltonian results in additional perturbative operators which are added to $\hat{H}'$ in equation (32). For a more detailed description of the expansion, we refer to [46] and [34]. Here, we will only give a brief overview of the resulting terms and the magnetic interactions they represent:

$$\begin{aligned}\hat{H}'\left(\bar{B},\hat{\bar{\mu}}_N,\hat{\bar{\mu}}_S\right) = {} & \hat{H}^{100}\cdot\bar{B} + \frac{1}{2}\bar{B}\cdot\hat{H}^{200}\cdot\bar{B} + \sum_{A=1}^{M}\hat{\bar{\mu}}_{N,A}\cdot\hat{H}_A^{010} \\ & + \sum_{A=1}^{M}\hat{\bar{\mu}}_{N,A}\cdot\hat{H}_A^{110}\cdot\bar{B} + \frac{1}{2}\sum_{A=1}^{M}\sum_{B=1}^{M}\hat{\bar{\mu}}_{N,A}\cdot\hat{H}_{AB}^{020}\cdot\hat{\bar{\mu}}_{N,B} \qquad (33) \\ & + \sum_{i=1}^{N}\hat{\bar{\mu}}_{S,i}\cdot\hat{H}_i^{001} + \sum_{i=1}^{N}\hat{\bar{\mu}}_{S,i}\cdot\hat{H}_i^{101}\cdot\bar{B} + \sum_{i=1}^{N}\sum_{A=1}^{M}\hat{\bar{\mu}}_{S,i}\cdot\hat{H}_{iA}^{011}\cdot\hat{\bar{\mu}}_{N,A}\end{aligned}$$

The perturbative operators $\hat{H}^{klm}$ in the above equation are expressed as dependent on the external magnetic field $\bar{B}$ (*k*-th order dependency), nuclear magnetic moments $\hat{\bar{\mu}}_N$ (*l*-th order) and electronic spin magnetic moments $\hat{\bar{\mu}}_S$ (*m*-th order).

- The $\hat{H}^{100}$-term describes the interaction of the magnetic field $\bar{B}$ with the electronic orbital angular momentum $\bar{L}$. A possible permanent paramagnetic moment for the molecular system is determined by this interaction.
- The second order $\hat{H}^{020}$-term in $\bar{B}$, represents the diamagnetic response of the electrons (through their orbital momentum $\bar{L}$) to the magnetic field, giving rise to magnetic susceptibility effects. Both the $\hat{H}^{100}$- and $\hat{H}^{020}$-terms in equation (33) establish the overall magnetic characteristics of the molecular system. Since in most molecular systems, the orbital angular momentum $\bar{L}$ will be “quenched” in a non-degenerate state, these terms can be largely ignored for our purposes.
- The governing effects in Nuclear Magnetic Resonance (NMR) spectroscopy [47] are explained by the $\hat{H}^{110}$ and $\hat{H}^{020}$ terms. This technique is very similar to EPR, except that now nuclear spin transitions are induced. The main spectroscopic parameters in NMR are the chemical shielding and the nuclear spin-spin coupling, described by the former and latter operators, respectively. The $\hat{H}^{010}$ term – describing the interaction of the electronic orbital motion with the nuclear spin magnetic moments – can be considered as a minor influence in this respect.
- Finally, the last two terms will play a predominant role in EPR and their operators $\hat{H}^{101}$ and $\hat{H}^{011}$ will be the main components of respectively,

the electronic g-tensor and hyperfine interaction tensor, which will be discussed later on.

- The sixth $\hat{H}^{001}$ term describes the interaction of the electronic orbital motion with the electronic spin magnetic moments, which is the spin-orbit interaction. As mentioned earlier, this term will have an impact on the g-tensor.

In the above, we have assumed that no electronic spin-spin interactions have taken place. Disregarding these is of course only valid if the unpaired electrons in the molecular system are "diluted" so that they are widely separated from each other and do not interact.

3.4 SPIN HAMILTONIAN

The complete expansion of equation (32) with inclusion of $\hat{H}'$ from equation (33) within perturbation theory can be found elsewhere [46]. Obviously, the result is quite massive but nevertheless generally applicable for all sorts of (molecular) systems. For our purposes, however, the above Hamiltonian presents an extreme "overkill", comprising interactions that are irrelevant in the studied biochemical systems. The magnetic resonance effects encountered in this work are therefore more easily interpreted in terms of a "phenomenological" Hamiltonian, which usually includes only electron-spin ($\hat{\bar{S}}$) and nuclear-spin operators ($\hat{\bar{I}}$) together with (numerical) spectroscopic parameters. This so-called "spin Hamiltonian" $\hat{H}_S$ in fact describes a model spin system, for which the solution of the Schrödinger equation:

$$\hat{H}_S \left|\Theta\right\rangle = E\left|\Theta\right\rangle \qquad (34)$$

renders eigenvalues in a basis of spin functions $\left|\Theta\right\rangle$ that will fit the observed energy levels of the real spin system, provided a proper choice for the numerical parameters. One could consider this an analogue of the "Kohn-Sham" approach for paramagnetic spin systems.

For the crystalline biomolecules that are the subject of this work, the molecular system contains only one unpaired electron, i.e. $S = 1/2$. Furthermore, the present nuclei are characterised by an effective nuclear spin magnetic moment:

$$\hat{\bar{\mu}}_N = g_N \beta_N \hat{\bar{I}}$$

where g_N is the nuclear g-value (dependent on the type of nucleus and assumed isotropic) and β_N is a constant, known as the nuclear magneton. The eigenvalue equations for the nuclear spin angular momentum $\hat{\bar{I}}$ are similar to those in equation (29):

$$\hat{I}^2 \chi^I_{M_I} = I(I+1)\chi^I_{M_I}$$
$$\hat{I}_z \chi^I_{M_I} = M_I \chi^I_{M_I}$$

from which it is obvious that in the presence of a magnetic field a nuclear Zeeman effect can occur, lifting the degeneracy of the $M_I = -I, -I+1, \ldots, +I-1, +I$ states. In this work, only Zeeman interactions will occur for nuclear isotopes with $I = 1/2$ (e.g. $^1\mathrm{H}$ or $^{13}\mathrm{C}$). Therefore, since $S = 1/2$ and $I = 1/2$ for all the M interacting nuclei, the spin Hamiltonian will be:

$$\hat{H}_S = \beta_e \hat{\vec{B}} \cdot \overline{\overline{g}} \cdot \hat{\vec{S}} - \beta_N \sum_{K=1}^{M} \hat{\vec{B}} \cdot \overline{\overline{g}}_{N,K} \cdot \hat{\vec{I}}_K + \sum_{K=1}^{M} \hat{\vec{S}} \cdot \overline{\overline{A}}_K \cdot \hat{\vec{I}}_K$$

This simple equation holds all relevant interactions taking place in the molecular system as resulting from the presence of a magnetic field.

Electronic Zeeman interaction

The electronic Zeeman interaction is now expressed by the Hamilton operator:

$$\hat{H}_Z = \beta_e \hat{\vec{B}} \cdot \overline{\overline{g}} \cdot \hat{\vec{S}}$$

where the electron spin $\hat{\vec{S}}$ and the external magnetic field $\hat{\vec{B}}$ are linked together through a tensor $\overline{\overline{g}}$ of rank 2. Experimentally, it is found that the g-factor is dependent on the orientation of the solid-state sample in the magnetic field. The g_J factor from equation (31) is therefore rather a **g-tensor**, the anisotropy arising largely through the spin-orbit interactions from $\hat{H}^{001}$ in equation (33).

In the organic radicals that are the subject of the second part of this work, the g-tensor shows relatively little anisotropy and therefore does not deviate substantially from the free electron value g_e. This EPR parameter will not be very sensitive to (slight) changes in conformation or geometry, up to the point that the principal g-tensor values for two different radicals can be virtually identical. In that case, differentiation will only be possible by looking at the orientations of the g-tensor axes. We have therefore chosen in this work to dismiss the g-tensor altogether as a probe for the structure determination of organic radicals.

Nuclear Zeeman interaction

In the presence of a magnetic field, nuclear Zeeman interactions will also occur in a molecular system. For nuclei with $I = 1/2$ the degeneracy is lifted for the $M_I = +1/2, -1/2$ states, commonly known as (nuclear) spin up and spin down states. The interaction of one nuclear spin angular momentum $\hat{\bar{I}}$ with the magnetic field $\hat{\bar{B}}$:

$$\hat{H}_N = -\beta_N \hat{\bar{B}} \cdot \bar{\bar{g}}_N \cdot \hat{\bar{I}} \tag{35}$$

is parameterised by the **nuclear g-tensor** $\bar{\bar{g}}_N$. The anisotropy effects will be seldom apparent and therefore $\bar{\bar{g}}_N$ is generally replaced by a scalar quantity known as the **nuclear g-factor**. This justified simplification reduces expression (35) to:

$$\hat{H}_N = -\beta_N g_N \hat{\bar{B}} \cdot \hat{\bar{I}}$$

In the related NMR spectroscopic technique, interaction (35) is connected with the "chemical shift" parameter, a measure of the effective field experienced by a nucleus due to the presence of induced currents in the chemical environment.

The nuclear Zeeman interaction(s) will thus cause an additional splitting of the energy levels for the spin functions $|\Theta\rangle$ in equation (34). Nevertheless, it will have no impact on the actual appearance of the EPR spectrum, since both the higher and lower energy levels are shifted with an equal amount of energy. Only in the ENDOR and EI-EPR techniques (briefly discussed further on), the indirect effect of this interaction on the EPR transitions will be exploited.

Hyperfine interaction

Most important from our point of view will be the coupling interaction between the spin angular momentum $\hat{\bar{S}}$ and the angular momentum $\hat{\bar{I}}$ of a nucleus (or nuclei) present in the molecular system:

$$\hat{H}_{hf} = \hat{\bar{S}} \cdot \bar{\bar{A}} \cdot \hat{\bar{I}} \tag{36}$$

The **hyperfine interaction tensor** $\bar{\bar{A}}$ is often divided into an isotropic and an anisotropic part:

$$\bar{\bar{A}} = A_{iso} \bar{\bar{1}} + \bar{\bar{T}} \tag{37}$$

with $\bar{\bar{1}}$ the 3x3 unit matrix and A_{iso} the **hyperfine coupling constant** or Fermi contact term. Diagonalisation of the $\bar{\bar{T}}$-matrix yields three eigenvalues (or principal components) and corresponding eigenvectors (or principal axes) relative to the reference axes system.

The hyperfine interaction arises due to the interaction of the magnetic moment of the unpaired electron $\bar{\mu}_e$ with nearby nuclear magnetic moments. Such a nuclear moment $\bar{\mu}_N$ will induce a local field B_{local} which can either enhance or decrease the intensity of the applied magnetic field B at the position of the unpaired electron.

This classical idea of interacting magnetic dipoles is illustrated in Figure 3.4, where the induced field lines of $\bar{\mu}_N$ counteract the applied magnetic field.

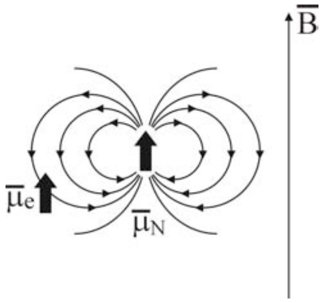

Figure 3.4: The induced local field of the nuclear moment counteracts the intensity of the magnetic field at the position of the electron.

Due to the nuclear moment, the electron will "feel" an effective field B', differing from the applied magnetic field. As a result, the resonance condition in (30) must be rewritten as:

$$h\nu = g_e\beta_e B' = g_e\beta_e\left(B + B_{local}\right)$$

and clearly the value of B required to achieve resonance will depend on B_{local}. As both the electronic and nuclear magnetic moments can assume either spin-up or spin-down states, resonance will occur at different field values for B, causing a splitting in the observed EPR spectrum.

Effect of all interactions on a simulated EPR spectrum

The effect of the hyperfine and electronic/nuclear Zeeman interactions can be best understood by considering their separate contributions to the eigenvalues for a simplified spin Hamiltonian. For a molecular system with one unpaired electron and only one interacting nuclear magnetic moment, a schematic overview of the energy levels is presented in Figure 3.5. Also, the effect on the EPR spectrum is illustrated of "switching on" the separate contributing interaction terms in the spin Hamiltonian.

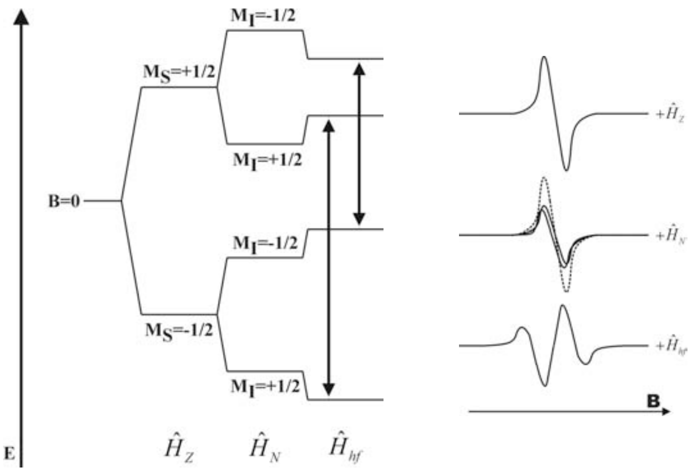

Figure 3.5: Effect of the contributing terms in the spin Hamiltonian on an example EPR spectrum (in which $H_N > H_{hf}$). At the left side, relevant energy levels are represented for a system containing one electron and one nucleus.

If only one electron would be present, the observed spectrum would show a single absorption ($\hat{H}_Z$). The presence of a nucleus, however, introduces two perturbations. The nuclear Zeeman interaction $\hat{H}_N$ in itself only causes an additional splitting of the individual energy levels for the spin Hamiltonian, which is not directly apparent in the spectrum. Only now, the single peak should be considered as the additive result of two peaks with half the original intensity that occur at the same field value. These are generated by absorptive transitions between the equally spaced energy levels, in compliance with the selection rules $\Delta M_S = 1$ and $\Delta M_I = 0$. By switching on the hyperfine interaction $\hat{H}_{hf}$, the energy levels are shifted with respect to each other and the splitting becomes visible, since the two smaller peaks are now observed at different field values.

3.5 ADVANCED MAGNETIC RESONANCE EXPERIMENTS

Ever since the introduction of EPR, a variety of derivative experimental techniques has been established. As some of them will be mentioned in the course of this work, we report some key concepts behind these methods. For a more thorough discussion, we refer to other works [41, 48].

3.5.1 ENDOR (Electron Nuclear Double Resonance)

This technique is typically applied to improve the spectral resolution or to disentangle between superimposed component spectra. Basically, an additional radiofrequent field (typically of the order of MHz) is applied to the sample cavity, which allows the excitation of nuclear Zeeman energy levels. These transitions are labelled "NMR" in Figure 3.6, where the energy levels of Figure 3.5 are reproduced.

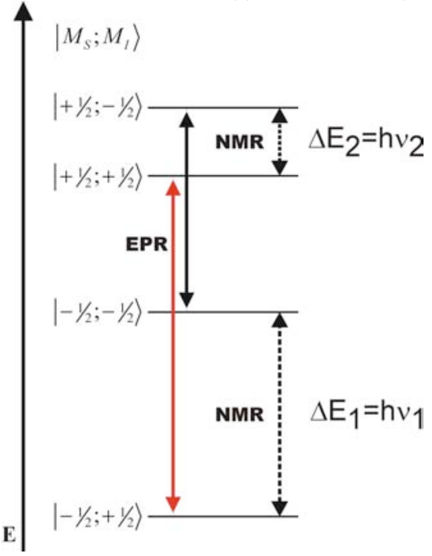

Figure 3.6: EPR and NMR transitions in an ENDOR experiment.

By applying sufficient microwave power, the EPR absorptions are saturated and the population difference between the corresponding states is driven toward zero. For the red transition in figure 3.6, this means that the $\left|-\tfrac{1}{2};+\tfrac{1}{2}\right\rangle$ and $\left|+\tfrac{1}{2};+\tfrac{1}{2}\right\rangle$ states are equally occupied. Consecutively, the radiofrequent (NMR) field is swept with the objective of detecting a change in the EPR absorption. When now, for instance, the ν_1 frequency is reached, additional transitions will be induced between the $\left|-\tfrac{1}{2};+\tfrac{1}{2}\right\rangle$ and $\left|-\tfrac{1}{2};-\tfrac{1}{2}\right\rangle$ states. As a result, the population difference between the $\left|-\tfrac{1}{2};+\tfrac{1}{2}\right\rangle$ and $\left|+\tfrac{1}{2};+\tfrac{1}{2}\right\rangle$ states will become non-zero and an increased EPR absorption will be apparent. Since the same will occur at frequency ν_2, two lines will be observed in the ENDOR spectrum. It can be shown that:

$$h\nu_1 = \left|\frac{1}{2}A + g_N\beta_N B\right|$$

$$h\nu_2 = \left|\frac{1}{2}A - g_N\beta_N B\right|$$

and therefore the ENDOR lines are separated by an amount A/h. The correlation between the observed ENDOR line separation and the hyperfine coupling allows a more accurate measurement of the latter parameter. Accordingly, this technique is often used to examine the anisotropic hyperfine tensor in a crystalline sample, by consequently recording the hyperfine coupling while rotating the crystal e.g. about the a, b or c crystal axes.

3.5.2 EI-EPR (ENDOR induced EPR)

In a composite spectrum, where the EPR resonances of different species are overlapping, it is sometimes difficult to accurately resolve the individual spectra of these species separately. The EI-EPR method enables the experimentalist to single out the spectrum of one component species. To achieve this, one of the NMR transitions – obtained in an earlier ENDOR experiment – is saturated, by setting the applied radiofrequent field to that particular ENDOR frequency. The magnetic field is then swept while the intensity of the ENDOR transition is monitored. This way, an enhanced EPR spectrum is obtained but only for the component species of which the NMR transition was induced. EI-EPR is therefore somewhat the reverse of the ENDOR experiment, as it also involves a double-resonance technique.

3.6 INTERPRETING THE HYPERFINE TENSOR

It is clear from the above that the EPR spectrum – a cumulative result of at least three different interactions – contains a lot of information with regard to the paramagnetic species. Through the hyperfine interaction, in particular, the molecular and electronic structure of the radical can be examined. However, the analysis of hyperfine tensor data is quite complicated and rarely straightforward. In this paragraph we therefore present some practical issues regarding the interpretation of this parameter. Throughout, we will concentrate on the hyperfine interaction of a proton within an organic radical in the solid state. As this case will be most commonly encountered in the discussed paramagnetic species, these interactions will yield the majority of all structural evidence.

3.6.1 Theoretical expressions

As already stated in (37), the hyperfine interaction tensor $\overline{\overline{A}}$ can be decomposed into an isotropic coupling constant A_{iso} and an anisotropic $\overline{\overline{T}}$-matrix. The A_{iso} coupling constant is a strictly local property, and depends solely on the unpaired spin density $\sum_{\mu,\nu} P_{\mu,\nu}^{\alpha-\beta}$ at the position of the nucleus concerned. An equation can be derived by incorporating (37) in (36) and expressing this as an expectation value, assuming an isotropic g-tensor:

$$A_{iso}^{N} = \frac{2}{3} g\beta_e g_N \beta_N \mu_0 \sum_{\mu,\nu} P_{\mu,\nu}^{\alpha-\beta} \left\langle \varphi_\mu \left(r_{Ni}\right) \middle| \delta\left(r_{Ni}\right) \middle| \varphi_\nu \left(r_{Ni}\right) \right\rangle$$

The Dirac $\delta\left(r_{Ni}\right)$ function (with r_{Ni} the distance between nucleus *N* and electron *i*) ensures that the integral for the molecular/atomic orbitals $\varphi_\mu\left(r_{Ni}\right)$ is evaluated at the position of nucleus *N* only. The isotropic contact interaction is of a purely quantum mechanical nature and has no classical analogue. The coupling constant is therefore best understood by examining the unpaired spin density at the nucleus. As this center is always located on a nodal plane for the p, d, f, etc. atomic orbitals, only an s-type orbital will contribute to the spin density at this position.

The anisotropic part of the hyperfine matrix, on the other hand, is due to the (classical) interaction of magnetic dipoles, and is described by the following equation:

$$T_{uv}^{N} = -\frac{g\beta_e g_N \beta_N \mu_0}{4\pi} \sum_{\mu,\eta} P_{\mu,\eta}^{\alpha-\beta} \left\langle \varphi_\mu \left(r_{Ni}\right) \middle| r_{Ni}^{-5} \left(r_{Ni}^{2}\delta_{uv} - 3r_{Ni,u} r_{Ni,v}\right) \middle| \varphi_\eta \left(r_{Ni}\right) \right\rangle$$

for the *uv*th component of the $\overline{\overline{T}}$ matrix. Since s-type atomic orbitals are spherically symmetric it is only obvious that the anisotropic contribution to the hyperfine tensor will depend rather on the spin population of valence p, d, etc. orbitals. A conceptual understanding of the anisotropic interaction is best attained by oversimplifying the system at hand, based on symmetry grounds, and by relying on the classical point dipole interaction.

3.6.2 The hyperfine tensor in organic systems

The organic molecules that will be considered in this work typically consist of H, C, N and O atoms. For these compounds, all the induced radicals share a common feature: the paramagnetic electron is located on a carbon atom, where it will mainly occupy a p-orbital (as outlined in Figure 3.3), if we hold on to the basic valence bond picture. The carbon center and the surrounding nuclei in the molecule will then interact with this unpaired p-type spin density to generate different hyperfine interactions. Historically, this type of radical has attracted much attention with regard to the study of π-type radicals in conjugated hydrocarbon molecules, where the unpaired electron is delocalised as a π-system, built up by several adjacent p-orbitals in the molecular skeleton. In fact, it was first in a study of one such system that the true value of the EPR technique in the structural identification of radicals was fully established [49]. To gain a better insight into this link between radical structure and EPR parameters, we discuss in this section the isotropic and anisotropic contributions to the hyperfine tensor of some of the relevant atoms in a typical organic radical. The concepts presented here – although sometimes more intuitive than physical – can be largely extended to the specific molecular systems discussed in the second part of this work.

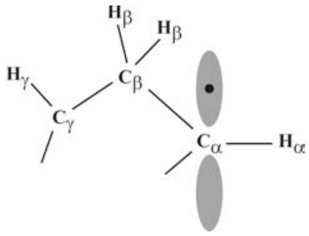

Figure 3.7: Representative structural component of a hydrocarbon radical.

In Figure 3.7, a representative structural component of a typical hydrocarbon radical is presented. The characteristic nomenclature is also given, where an atom is labelled α, β, γ, etc. according to its position with respect to the location of the unpaired electron. The C_α carbon is called as such because it is the direct site for the paramagnetic center, the H_α proton because it is connected to this carbon atom. Similarly, β-, γ-, … carbons and protons can be distinguished, as they are consistently located one atom further away. The unpaired electron will to some extent interact with all these nuclei, provided they have a non-zero nuclear magnetic moment. In practice, this implies that – besides the proton ^1H – only a minority isotope (1.1% natural occurrence) of the carbon atom – ^{13}C – will couple with the electron, as the most abundant isotope ^{12}C does not have a nuclear moment.

Isotropic component

The isotropic hyperfine coupling constants (or the unpaired spin density) for these atoms are the result of two different contributing effects: (1) direct delocalisation and (2) spin polarisation. The first contribution arises whenever the unpaired electron is in some way directly delocalised to the nucleus under consideration. Spin polarisation (or π-σ configuration interaction) refers to the fact that an unpaired electron interacts differently with the two electrons of a filled orbital.

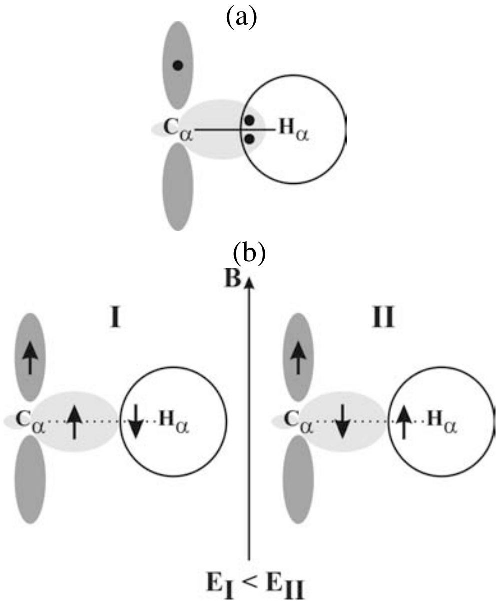

Figure 3.8: **(a)** valence bond description of the C-H bond, **(b)** spin polarization.

The importance of this latter effect becomes apparent when examining the origin of the C_α or H_α hyperfine coupling constant. The C_α-H_α bond is illustrated in Figure 3.8(a) adopting the valence bond theory. While the unpaired electron resides in a 2p non-interacting orbital of carbon, the C-H bond is caused by the constructive overlap between the C_α sp^2 with the H_α 1s orbital. However, both C_α and H_α are in the nodal plane of the 2p orbital and the direct delocalisation of the unpaired electron to H_α is simply non-existent. Yet, both nuclei are found to have considerable isotropic coupling constants and therefore some unpaired spin density must certainly be present. The origin of this density is spin polarisation. As shown in Figure 3.8(b), two configurations can be proposed: one in which the C_α sp^2 spin is parallel to the unpaired p-electron (**I**) and one in which it is anti-parallel (**II**). Taking into account the Pauli principle, the H_α 1s electron spin is always opposite that of the sp^2 orbital. However, both spin configurations do not have equal weights. The spin polarisation gives slightly greater weight to **I**, in which the two electrons at the carbon atom have parallel spins (following Hund's rule). As a result, there is an imbalance between the amount of "up" and "down" electrons in the filled C-H bond orbital, causing a positive spin density in the case of C_α and a negative spin density for H_α. The resulting hyperfine coupling constants will therefore be positive, respectively, negative for C_α and H_α. The above situation only applies to carbon atoms that have perfect sp^2 hybridisation. In reality, of course, this will seldom be the case, and the orbital containing the unpaired electron (sometimes referred to as "Lone Electron

Orbital" or LEO) will retain in part some s-character. In this case, the spin density at any point will be the net resultant of the direct delocalisation and spin polarisation effects.

A β-proton (or γ, δ, … for that matter) is not necessarily located in a nodal plane of the paramagnetic p-orbital. Even though both effects will still play, spin polarisation will be less determining. It is rather direct delocalisation of spin density from the LEO to the sp^3 orbital of the C_β-H_β bond – known as hyperconjugation – that will control the size of the hyperfine coupling for this proton. The magnitude of this hyperconjugation, in turn, depends on the local geometry of the molecular fragment. More specifically, it can be shown [38] to be proportional to $\cos^2\theta$, where θ is the dihedral angle between the H_β-C_β-C_α plane and that containing the C_α p-orbital and the C_α-C_β bond, as illustrated in Figure 3.9. This conformational dependence of the isotropic hyperfine coupling constant highlights the validity of the EPR technique to examine the structure of radicals, from an experimental point of view. Even though significant γ-couplings will be observed in the course of this work (see Chapter 8), in general, the γ-proton and the unpaired electron are too far apart for the hyperfine coupling constant to be measurable. The same, obviously, applies for nuclei located even further away.

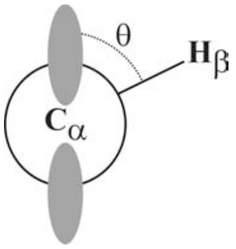

Figure 3.9: Newman projection along the C_α-C_β bond and definition of the dihedral angle θ.

Anisotropic component

Even though the isotropic hyperfine interaction already reveals a considerable link with the radical geometry, experimentalists most often rely on a careful analysis of the anisotropic hyperfine interactions to identify the structure of organic radicals. This is because the $\overline{\overline{T}}$ matrix contains an extensive amount of structural information. Its eigenvalues (T_1, T_2 and T_3) and eigenvectors ($\overline{1}(T_1)$, $\overline{1}(T_2)$ and $\overline{1}(T_3)$) can also be determined for the coupling nuclei in an organic radical. The theoretical derivation (based on symmetry and a simplified treatment of the dipole interaction) is beyond the scope of this work and we only report the derived typical characteristics for C_α, H_α and H_β as given in [39].

Neglecting all perturbative or conjugating interactions in the radical, the p-orbital of a $\mathbf{C}_\alpha$ center is axial symmetrical along its axis (hereafter designated the z-axis). It can therefore also be expected that the anisotropic tensor is axial symmetric, with one principal direction along the z-axis and the other two eigenvectors in the xy plane. This is illustrated in Figure 3.10, where also the characteristic pattern of coupling constants is given for the anisotropic eigenvalues. As the eigenvectors in the xy plane are degenerate, the corresponding anisotropic coupling components will equal an amount $T_{\perp} = -b$, whereas the principal hyperfine axis along z has a major anisotropic eigenvalue of $T_{\parallel} = +2b$. In an actual radical this characteristic pattern will be slightly altered, as bonds or conjugative effects distort the ideal axial symmetry of the p-orbital. Nevertheless, the nearly degenerate nature of the T_2 and T_3 components will still be quite pronounced.

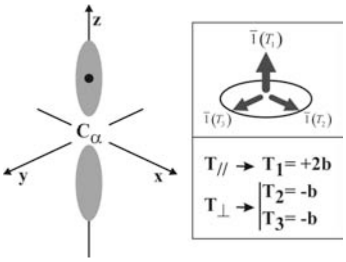

Figure 3.10: Anisotropic hyperfine eigenvectors and eigenvalues for a C_α carbon atom.

When a bond between a proton and the C_α radical center is taken into account, the hyperfine anisotropic tensor for $\mathbf{H}_\alpha$ is far from axial. Three separate, non-degenerate anisotropic components can be distinguished. The largest eigenvalue ($T_1 = +b$) is observed for an eigenvector pointing directly towards the carbon (along x-axis), an intermediate $T_2 = 0$ is obtained for the vector parallel with the z axis and the remaining principal direction is perpendicular to the other two, with an eigenvalue of $T_3 = -b$. Such a pattern of anisotropic coupling constants uniquely characterizes an α-hydrogen atom and can immediately be identified as such when observed from an EPR spectrum. The H_α-tensor is represented in Figure 3.11.

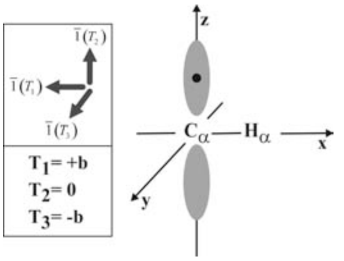

Figure 3.11: Anisotropic hyperfine eigenvectors and eigenvalues for an H_α proton.

Because the **H**$_\beta$ proton is located much further away from the C$_\alpha$ center than the H$_\alpha$ proton, it is acceptable to disregard the asymmetrical shape of the p-orbital. By then approximating the orbital by an s-like structure, the C$_\alpha$-H$_\beta$ fragment becomes axially symmetric. The tensor for the latter proton takes on the same symmetry and the resulting pattern of coupling constants bears a qualitative similarity with that of a C$_\alpha$ anisotropic hyperfine tensor. Again one major component $T_\parallel = +2b$ and two minor, quasi-degenerate $T_\perp = -b$ eigenvalues are encountered. The main difference with the C$_\alpha$ coupling scheme is the magnitude of the eigenvalues, which are usually substantially smaller (often by a factor of ten or more). The eigenvector associated with the major component is parallel with the C$_\alpha$ --- H$_\beta$ direction and the two degenerate vectors lie in the xy plane. In reality, of course, pure axial symmetry will rarely be observed and the two minor principal axes will be non-degenerate. It is difficult however to associate the directions of these two eigenvectors with a specific structural aspect of the radical. Nevertheless, the $\bar{1}\left(T_\parallel\right)$ eigenvector with major anisotropic component will persistently point more or less along C$_\alpha$ --- H$_\beta$, as illustrated in Figure 3.12.

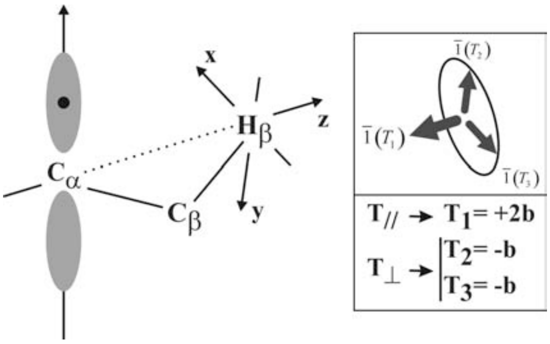

Figure 3.12: Anisotropic hyperfine eigenvectors and eigenvalues for an H$_\beta$ proton.

Chapter 4. General strategy for the calculation of EPR parameters

In this chapter we will outline the general computational strategy that is followed to determine theoretical EPR parameters through DFT calculations. In the second part of this thesis, we will apply this strategy to examine the radiation-induced radicals in amino acids and sugars. Although a detailed account of the computational results for these applied systems will be presented there, we will already refer to some of them in this chapter, as illustrative examples.

In addition, a more general purpose of the specified strategy is to provide a base computational protocol for researchers interested in studying radicals in extended systems from a theoretical point of view. As a consequence, this scheme is – whenever possible – outlined from a general perspective and is therefore not necessarily solely applicable for radiation-induced radicals in amino acids and sugars – although specifically utilized for these systems in the next chapters.

4.1 OVERVIEW

In the experimental setup, structural information regarding a radiation-induced radical species is deduced by thorough analysis of resonance parameters, obtained through EPR, ENDOR and/or EIE studies. In molecular modeling this procedure is rather reversed and one starts out by proposing one or more radical models. This initial step will be called the "**radical model selection**" step throughout this thesis. Subsequently, a stable radical geometry is determined which is a global (or local) energetic minimum in terms of all possible degrees of freedom in the used model space. This is accomplished by a computational optimization procedure – generally known as "**geometry optimization**" – transforming an initial geometry to an optimized geometry for the considered radical model. Next, the EPR parameters can be calculated for these optimized geometries, in the "**EPR calculation**" procedure. These calculated parameters must evidently be subjected to a thorough **analysis**, which adds up to the final step. This general strategy is illustrated in Figure 4.1 for the experimentally observed radical species II of α-D-glucose (which will be discussed at length in Chapter 9). In what follows, we will discuss the separate steps of this general strategy in more detail, using α-D-glucose as an example.

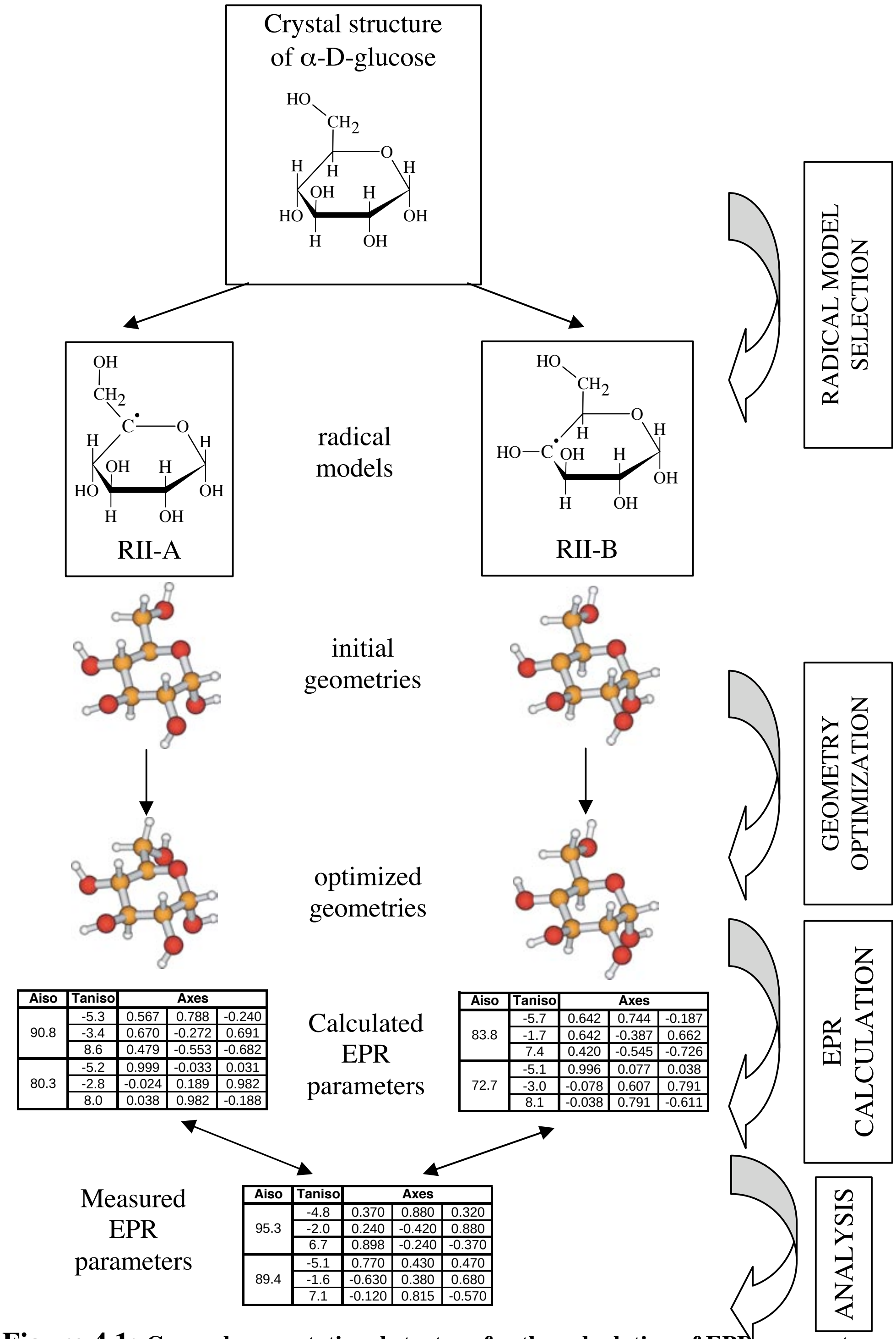

Aiso	Taniso	Axes		
90.8	-5.3	0.567	0.788	-0.240
	-3.4	0.670	-0.272	0.691
	8.6	0.479	-0.553	-0.682
80.3	-5.2	0.999	-0.033	0.031
	-2.8	-0.024	0.189	0.982
	8.0	0.038	0.982	-0.188

Aiso	Taniso	Axes		
83.8	-5.7	0.642	0.744	-0.187
	-1.7	0.642	-0.387	0.662
	7.4	0.420	-0.545	-0.726
72.7	-5.1	0.996	0.077	0.038
	-3.0	-0.078	0.607	0.791
	8.1	-0.038	0.791	-0.611

Aiso	Taniso	Axes		
95.3	-4.8	0.370	0.880	0.320
	-2.0	0.240	-0.420	0.880
	6.7	0.898	-0.240	-0.370
89.4	-5.1	0.770	0.430	0.470
	-1.6	-0.630	0.380	0.680
	7.1	-0.120	0.815	-0.570

Figure 4.1: **General computational strategy for the calculation of EPR parameters.**

4.1.1 Radical model selection

The starting point for the generation of a radical model is always the crystal structure, as determined from X-ray or neutron diffraction studies. Preferably the crystal structures obtained through the latter method are used, mainly because the positions of hydrogen atoms are more accurately determined than through X-ray diffraction. The crystal structure thus provides us with the conformation of an "undamaged" biomolecule in the lattice – before a possible radiation-induced breakdown has taken place.

In accordance with certain observations made in experiments or from other hypotheses, a number of radical models can then be proposed, depending on the goal of the molecular modeling study. If one aims to reproduce or verify the experimentally observed EPR parameters (as will be mostly the case in this work), it is not useful to consider radical models that are a priori incompatible with experimental results. For instance, in the case of glucose – where two β-type hyperfine couplings are observed – it would be pointless to consider a radical model that contains a $C^{\bullet}$-H fragment, as this would give rise to an easily identifiable α-type coupling. Therefore only radical models that could possibly explain the two β-couplings should be considered. Two examples (RII-A and RII-B) conform this criterion are shown in Figure 4.1. On the other hand, if one aims to make predictions for a molecular system for which no (or only incomplete) experimental data is at hand, all possible radical models should be considered. This obviously implies that a huge amount of candidate structures must be examined, depending on the complexity of the system under investigation. The number can be reduced however, by making sound hypotheses based on radiation chemistry [39] or by analogy with existing, similar molecular systems.

As a starting point for the geometry optimization, the undamaged crystal structure is modified to produce initial geometries, in accordance with the configuration of the proposed radical models. In both illustrated models for glucose, the model system differs from the undamaged molecule by the elimination of one hydrogen atom. Correspondingly, initial geometries for both radical models are obtained by selectively removing a hydrogen atom in a certain area of the glucose crystal structure. Obviously, for the radical models of other molecular systems, larger parts of the undamaged molecule – e.g. -OH or -CH_2OH groups – may have to be removed to generate the initial geometries. Possibly, (groups of) atoms may even have to be added to the crystal structure, although this was never encountered in the present work.

One could consider the outlined process of arriving at an initial geometry for a radical model, to be a rough analogy with the actual radiation-induced radical formation occurring in nature. The removed atoms would then correspond to the "waist"-products generated through the radiolysis reaction of the undamaged molecule. In a real organic crystal, these products will most likely diffuse throughout the lattice and either reconnect with another neighbouring molecule or remain trapped. Depending on the distance between this reattached or trapped residue and the studied radiation-induced radical, certain interaction effects could be expected. Even though simulations of these are possible and have been performed (for an example see [50]), we have not treated these interactions throughout this work, as we expect them to be only slightly perturbative and therefore negligible. The removed atom groups in the above are therefore always considered as non-existent.

4.1.2 Geometry optimization

In these calculations, the initial geometry is transformed into an optimized geometry for the radical, by varying its degrees of freedom in the used model space until a conformation with minimal energy is reached. The level of theory at which this search is performed will obviously be a first determining factor for the accuracy of the eventual outcome. A second important factor will be the approach with which the **model space** is simulated. The latter term refers to the ensemble of the radical and the part of its solid-state environment that is explicitly accounted for in the calculation. This is schematically represented in Figure 4.2.

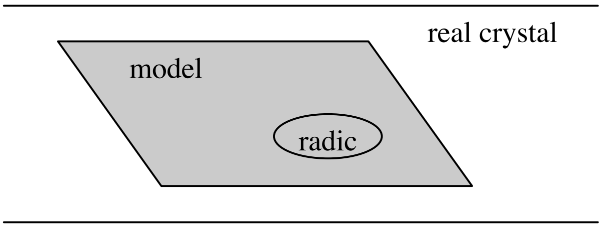

Figure 4.2: **The model space concept.**

The model space approach thus directly determines which interactions between the radiation-induced radical and its solid-state environment are explicitly accounted for, and at what level of theory they are treated. When the complete crystal lattice is chosen as model space, all interactions are – in principle – taken into account while, in contrast, all intermolecular interactions are totally ignored when considering only the radical itself in the model space. Naturally, we can expect calculations with a larger model space to be computationally more demanding. The different approaches that can be followed to treat the model space are discussed in detail in a subsequent paragraph. However, we already remark at this point that whatever approach was used during the different geometry optimizations reported in this work, the part of the model space responsible for mimicking the solid state was treated as completely static. This implies more specifically that during the optimization procedure only the initial radical geometry was allowed to (partly) relax, while the simulated part of the crystalline environment – if included in the calculation – was kept fixed conform the experimental crystal lattice positions.

As a side-step we remark that the determination of a radical conformation with absolute minimal energy is sometimes difficult, depending on the complexity of the studied radical and/or the used model space approach. In these cases, it is sometimes useful to perform as an initial step energy scans, in which the conformational space of the radical is sampled as a function of one or possibly more degrees of freedom. Typically, the repercussion of the rotation of a functional group (such as -OH, -CH_2OH, -NH_3, …) on the total energy is examined. This is done by calculating the energy for radical structures with incrementally rotated functional groups (e.g. at 0°, 15°, 30°, 45°, …). This slice of the energy hypersurface with respect to one degree of freedom, thus gives a good idea of the optimal conformation for this specific rotation. Adjusting this parameter manually and consequently initiating a geometry optimization often speeds up the optimization procedure.

4.1.3 EPR calculation

In a final calculation, the EPR parameters are derived from the electronic wavefunctions or spin densities, determined for the optimized geometry from the previous step. The Gaussian software (versions 1998 [30] and 2003 [31]) was used to perform these calculations, even though other packages (such as ADF [29]) are equally capable. However, since the employed level of theory for the wavefunctions or spin densities is of primordial importance for the accuracy of the EPR calculation, we specifically prefer the Gaussian software, as it offers a wide range of large basis sets and additional polarisation or diffuse functions, among other things.

Even though both Gaussian (2003) and ADF are able to calculate the g-tensors of paramagnetic systems, we have not considered this information, since it shows relatively little anisotropy for organic radicals and therefore does not deviate substantially from the free electron value g_e. In contrast, the hyperfine coupling tensor is a very sensitive probe for these biomolecules. The Gaussian software characterises these tensors by three main parameters (which we shall call EPR parameters from now on): the isotropic hyperfine coupling constant, three anisotropic hyperfine couplings and the associated principal axes. In the tables on Figure 4.1, these parameters are referenced as “A_{iso}”, “T_{aniso}“ and “Axes” respectively.

The accuracy of these calculated EPR parameters will first of all be determined by the accuracy of the optimized geometry. One cannot expect the calculated parameters to accord with e.g. experimental values, if the radical model is incorrect or if the optimized geometry does not correspond with the naturally occurring radical conformation. We also find, however, that the model space approach can be of considerable importance in this type of calculation. This is actually quite plausible, as intermolecular interactions will affect the electron spin density distribution across the radical and consequently will have an effect on the calculated EPR parameters.

As already mentioned, the level of theory argument is of major importance at this step. Numerous studies have been conducted, examining the effect of more elaborate basis sets, different computational approximate methods (e.g. HF, DFT, MP2) or – in the case of DFT – of various functionals [51]. Furthermore, the isotropic hyperfine coupling is directly proportional to the spin density at the point of the corresponding nucleus. As a result, the functions in the basis set describing the core region must be well described.

4.1.4 Analysis

The whole point of the EPR calculation is of course to make use of the resulting theoretical data. One can either compare it with experimentally obtained data, or otherwise predictions can be made. In this work, we will always cross-reference the calculated parameters with experimental ones. Based on the correspondence between theory and experiment, an assessment can then be made of, first, the validity of the proposed radical model and, second, of the accuracy of the optimized radical geometry within the model space.

A comparison between calculated and experimental hyperfine tensor parameters is quite easy for A_{iso} and T_{aniso}, where only values must be compared, but is more tricky for the principal anisotropic axes. We will therefore often present the angle (in degrees) between the experimental and the theoretically predicted directions. Although this angle will constitute an easy estimate for the match between theory and experiment, the actual direction cosines of the principal directions contain more structural information, as was specified in section 3.6.

4.2 MODEL SPACE

The model space determines how the solid-state environment of the radical is described, which intermolecular interactions are considered therein and at what level they are treated. Three types of model space approaches can be distinguished in this work.

4.2.1 Single molecule approach

The easiest way to simulate radicals in a solid-state environment is to simply ignore the solid state. This is the case in the single molecule (or isolated molecule) approach, where the model space solely consists of the studied radical. The crystalline molecular environment surrounding the radical is thus not incorporated in any way and calculations on the radical are performed in the (ideal) gas phase, at 0 K. Several successful applications of this approach appear throughout literature [52]. Despite the attractive computational advantage of dealing with only one molecule (the radical), several problematic issues are associated with this approach. Throughout this work, all calculations involving this approximated model space have been performed with the Gaussian software [30, 31].

Geometry Optimization

Geometry optimization calculations may be often problematic. Indeed, the real structure and conformation of a radical is mostly determined by prevailing intermolecular forces between the radical and its solid-state neighbouring molecules. Since these forces are not accounted for in a single molecule geometry optimization, it is not likely that the radical will attain the correct solid-state conformation. Instead, it will rather assume a conformation with minimal energy in the gas phase. Still, the results of these full optimization calculations can often be satisfactory considering the minimal computational effort. This is mostly the case when mainly intramolecular interactions rather than intermolecular interactions determine the radical conformation, or when the absence of the former intermolecular interactions – possibly by chance – imposes only insignificant changes upon the geometry. For an example, we refer to the discussion of the radiation-induced radicals in glucose (see Chapter 9). Nevertheless, the result of full geometry optimizations within the single molecule approach can sometimes be very poor or even totally unphysical. In the radiation-induced radicals of sorbose, for instance, an incorrect conformation was obtained for the A-conformation of radical model S-I, resulting in bogus EPR parameters (Chapter 10). More dramatic illustrations are the amino acids, where a full geometry optimization of the radicals in the single molecule approach destroys their zwitterionic form in favour of a neutrally charged form (Chapter 5 and 6).

This problem can – only in part – be solved by imposing additional constraints on the radical conformation during the geometry optimization. One could, for instance, impose the constraint that only the atoms in the direct vicinity of the paramagnetic center in the radical are allowed to relax, while all other atoms are kept at their original positions in accordance with the pristine crystal structure. In the case of the above illustrated RII-B glucose radical, this would imply that only the three atoms in the -C$^{\bullet}$-OH fragment are allowed to shift in position during the optimization, while all other atoms remain at their respective coordinates in the initial geometry (which is identical to the original glucose crystal structure, minus one hydrogen atom). In contrast with the **full optimization scheme**, where all atoms are allowed to relax (introduced in the previous paragraph), this rudimentary **partial optimization scheme** accounts in an artificial way for effects that are normally caused by intermolecular interactions. However, it will only render useful results if radical and undamaged molecule are structurally much alike. We refer to the discussion of the radiation-induced radicals of sorbose (Chapter 10), where this scheme was successfully applied. One step further in this line of thought is to constrain all atoms, which actually means that no optimization is performed at all. In this **no optimization scheme**, the optimized geometry for the radical model simply equals the initial geometry. Although the results can hardly be expected to be in good quantitative agreement with the actual solid-state radical conformation, this oversimplified scheme allows for quick and easy initial assessments. We again refer to the discussion in Chapter 10 for an example.

In Figure 4.3, the three optimization schemes are illustrated on the initial geometry of the RII-A glucose radical. Atoms that will be allowed to relax in the optimization calculation are marked green.

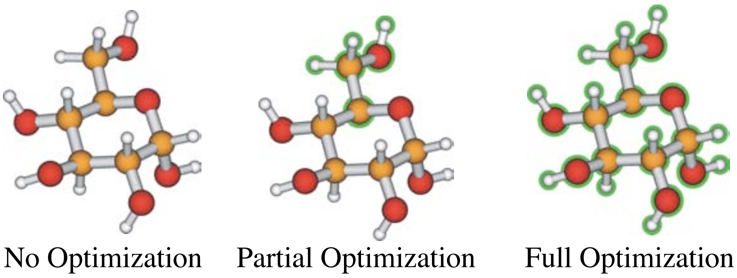

Figure 4.3: **Different Optimization Schemes.**

EPR calculation

Usually, most EPR calculations are performed within the single molecule approach, even when the optimized geometries were obtained in geometry optimizations entailing more complicated model space approaches. Since all intermolecular interactions are neglected in this model space, the most determining factor in these calculations is the employed level of theory, as discussed above.

However, when used for EPR calculations, there are some problems with the single molecule approach, more specifically for the calculation of the hyperfine tensor principal axes. For this particular calculated parameter to be of use, we must be able to compare it with experimental results. Yet, in experiments, the orientations of the measured hyperfine principal axes are specified as direction cosines with respect to a reference frame, usually coinciding with the crystal axes (or an orthogonal projection of them). To allow for a direct comparison between theory and experiment for this parameter, the calculated hyperfine tensor principal axes must therefore also be specified as direction cosines with respect to the same (or a parallel) reference frame. Unfortunately, the model space in a single molecule approach does not contain any explicit information about the crystal axes, including their orientations, and the EPR hyperfine tensor axes are calculated with respect to an arbitrary "standard" reference frame, as determined by the (Gaussian) software. If however, the exact orientation is known of the optimized geometry of the radical with respect to the crystal axes, only a simple coordinate transformation is required to use these axes (or an orthonormal projection) instead as a reference frame. This then, straightforwardly delivers direction cosines that can be directly compared with the experiment. This is schematically illustrated in Figure 4.4 for the hyperfine tensors of one proton in a sugar-like radical.

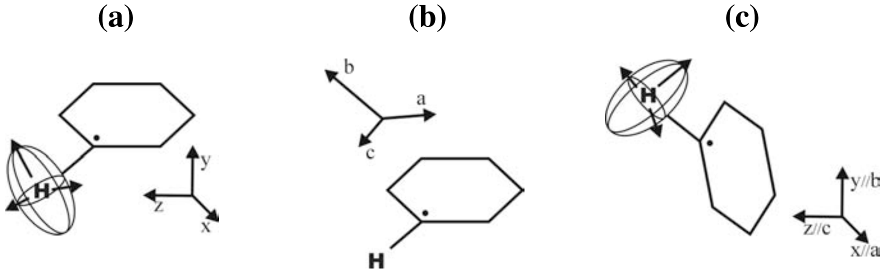

Figure 4.4: **(a)** The hyperfine tensor principal axes (represented by an ellipsoid) are calculated with respect to a standard reference frame <xyz>. **(b)** Only if the absolute orientation of the geometry optimized radical structure is known with respect to the original crystal axes <abc> (e.g. from earlier cluster calculations), **(c)** can the hyperfine tensor principal axes be referenced to the crystal axes reference frame (through a coordinate transformation).

In geometry optimizations with either a periodic or a cluster approach, some part of the undamaged crystal is comprised in the calculation and consequently the orientation of the crystal axes is always known. Thus, whatever conformational changes the initial radical geometry has undergone during the optimization, the absolute orientation of the optimized structure with respect to the crystal axes can at all times be traced. In single molecule optimizations, on the other hand, no information about the crystal axes is retained during the optimization. As a result, the absolute orientation of the optimized radical structure with respect to the crystal axes is unknown, and an analysis of the calculated hyperfine tensor axes becomes problematic.

One way to solve this problem is to artificially introduce the crystal axes in the model space during geometry optimization by imposing the additional constraint that the global orientation of the radical does not change dramatically, compared with that of its pristine molecular structure in the crystal lattice. Practically, this approximation is most easily imposed by adding the NOSYM keyword in a Gaussian (98 or 03) geometry optimization job, forcing the software to maintain the same reference frame throughout the calculation, as specified by the input of the initial geometry for the radical. Since we used the crystal structure coordinates to generate this geometry (by removing one or more atoms), we know exactly the orientation of the <abc> axes with respect to an initial reference frame $<x_{initial}y_{initial}z_{initial}>$. Since the orientation of this axes frame remains fixed during the geometry optimization procedure, we can now also relate the final, optimized geometry of the radical to the crystal axes.

We stress that this **Fixed Axes approximation** only imposes a constraint on the orientation of the radical, but certainly not on its conformation. Indeed, the final optimized radical conformation would be exactly the same conformation as one obtained through a geometry optimization without a NOSYM keyword. Their global orientations on the other hand are not necessarily the same. This approximation is schematically outlined in Figure 4.5.

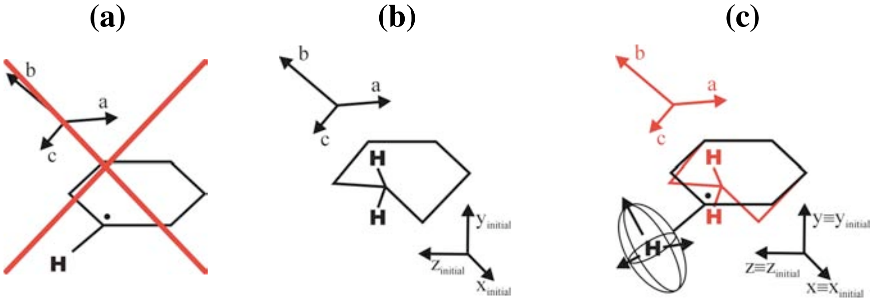

Figure 4.5: (a) In a single molecule approach, the orientation of the optimized radical geometry with respect to the crystal axes is not known. **(b)** The relative orientation of the latter axes frame, on the contrary, is well established for the undamaged crystal structure. **(c)** If the same initial reference frame is maintained throughout the geometry optimization, thus assuming that the global orientation of both radical and undamaged molecular structure are virtually identical, the hyperfine tensor principal directions can now also be calculated with respect to the crystal axes.

The major value of this approximation is that it enables a direct and easy comparison between experimental and calculated hyperfine direction cosines with respect to the crystal axes, despite the use of a single molecule approach. We refer to the discussion on the radiation-induced radicals of glucose (Chapter 9) as a successful example. Unfortunately, the approximation is not universally valid, as it is only relevant when the actual radical species is indeed very much alike the undamaged biomolecule, both in structure and in orientation.

There are biomolecular systems for which the Fixed Axes approximation does not hold and would even result in an unphysical representation of reality, since there are solid-state radicals that differ substantially from the undamaged crystal structure.

Constraining the crystal axes for these systems, would lead to direction cosines for the principal hyperfine directions that are entirely erroneous if, for instance, the radical is in reality rotated away from the original undamaged crystal structure. In this case, we must revert to another methodology to analyse the tensor axes, illustrated in Figure 4.6. The point is to eliminate any choice of a reference axis system and simply determine the mutual angles between the calculated proton tensor axes and consequently compare these with similar mutual angles between the experimental hyperfine axes of the observed radicals.

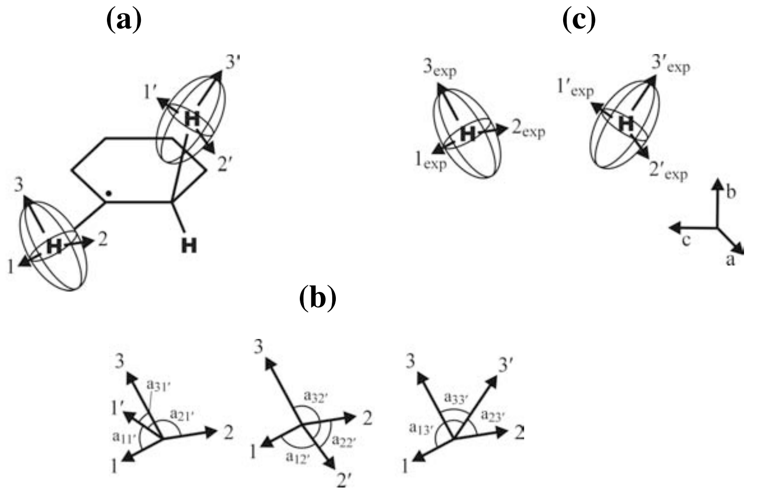

(d)

Theory			
	1'	2'	3'
1	$a_{11'}$	$a_{12'}$	$a_{13'}$
2	$a_{21'}$	$a_{21'}$	$a_{23'}$
3	$a_{31'}$	$a_{32'}$	$a_{33'}$

⇔

Experiment			
	$1'_{exp}$	$2'_{exp}$	$3'_{exp}$
1_{exp}	$a_{11'}$(exp)	$a_{12'}$(exp)	$a_{13'}$(exp)
2_{exp}	$a_{21'}$(exp)	$a_{22'}$(exp)	$a_{23'}$(exp)
3_{exp}	$a_{31'}$(exp)	$a_{32'}$(exp)	$a_{33'}$(exp)

Figure 4.6: (a) In the absence of a known reference frame, the hyperfine principal directions for e.g. two protons in a radical can be considered relative to each other, **(b)** and their mutual angles can be calculated. **(c)** The same procedure can be performed for experimentally determined hyperfine tensors, even though their orientations with respect to the crystal axes are known. **(d)** The resulting angles are best summarised in tables, which must then be subjected to a detailed comparative study.

Analysis of the resulting tables is subject to some ambiguity in fixing the relative angles (φ or φ-π) due to the fact that the absolute sign of direction cosines cannot be determined. Furthermore, if several magnetically distinguishable sites in the crystal lattice are possible for the radical to reside in, the situation becomes even more complicated. The analysis of the calculated EPR parameters within this **relative method** is therefore very complex in comparison with the Fixed Axes approach. In addition, less information remains accessible. For instance, in a radical characterised by two hyperfine coupling nuclei, only one informative parameter is available in the former method (one table with relative angles) while in the latter there are two (the direction cosine values of two separate hyperfine tensors). On the other hand, the approach is generally applicable and does not impose extra constraints.

4.2.2 Cluster approach

In cluster calculations, a part of the crystal lattice is explicitly modeled, by placing discrete molecules around the target radical. The atomic coordinates of the latter molecules are in accordance with experimental crystallographic data. The model space thus consists of a central radical and several neighbouring molecules from the lattice, and the total number of molecules (+radical) finally determines the extent of the model space.

This kind of model was first introduced in the early seventies [53, 54] in its simplest form, where a central molecule was surrounded by atomic point charges, in positions as determined by an X-ray study. The lattice molecules in the cluster were thus reduced to ensembles of point charges, their values determined earlier in a calculation on one molecule. This simple "**point charge cluster model**" was extensively used, with relative success, not only to simulate the effects of the crystal field on the geometry of a central molecule, but also to examine non-structural properties, such as spectroscopic parameters [55]. Nowadays, point charge cluster models are still in use [56] although more commonly to further extend already elaborate clusters to a higher level of theory, as much has changed with regard to computer technology. Whereas in one of the first publications on the cluster model [54], only 4 "point charge" molecules were considered surrounding a "Hartree-Fock" central cyanoformamide molecule, more recent publications report the use of hundreds or even thousands of point charges, surrounding a central entity [57].

The major disadvantage of this point charge based approach is that it can only account for long-range electrostatic interactions, but totally neglects short-range interactions or electronic overlap between the central molecule (or radical) and its nearest neighbours [58]. Since all biomolecular systems considered in this work involve elaborate hydrogen bonding schemes, this counteractive argument definitely applies, and a complete quantum mechanical treatment of both the central radical and the environment is desired to model the intermolecular interactions correctly. This approach is better known as a **"supermolecule or cluster approach"** and is regularly used to determine both structural and spectroscopic properties [59, 60, 61].

Throughout this study, we will always refer to the supermolecule approach, applied to paramagnetic molecular systems. Hardly any studies have been performed on radical species embedded in organic crystals, although the model is somewhat more popular for the description of defects or paramagnetic substances in inorganic systems [57, 61, 62, 63]. However, several issues have to be considered when applying a cluster model space, both for geometry optimization and EPR calculations.

Geometry Optimization

Cluster Size

When performing geometry optimizations within a cluster approach, a first determining factor for the accuracy of the resulting optimized radical geometry, will be the number of molecules taken up in the model space, or **cluster size**. One can expect that, the larger this cluster size is, the more interactions between radical and simulated solid state are accounted for, and consequently the more accurate the modeling of the crystalline system will be. Unfortunately, calculations with larger cluster sizes impose substantially larger demands on computer resources and therefore a compromise between expected accuracy and computational cost has to be searched. The best way to limit the size of the cluster in a meaningful way is by critically evaluating which interactions between radical and crystal matrix are absolutely essential in a correct description of the radical geometry, and which interactions can be eliminated.

These **intermolecular interactions** within the crystal lattice can be (roughly) classified into three types, based on the reach at which they are effective.

Hydrogen bonds

All organic crystals discussed in this work are basically held together by hydrogen bond interactions, forming actual networks between layers of molecules. In the case of amino acids, $^+$N-H----$^-$O-C fragments are involved, while in sugars the hydrogen bonds are strung up in O-H----O-C fragments. Hydrogen bond lengths (H----$^-$O or H----O distances) usually vary between 1.8 Å and 2.0 Å, although they can sometimes be larger in certain sugars, for instance. As these forces are of such importance in the lattice, we can only expect them to have an equally decisive impact on the geometry of the radical. The smallest, relevant cluster for the description of a radical within a crystal lattice is therefore one in which at least all hydrogen bond interactions between radical and lattice are accounted for.

Short-range interactions

Under this interaction type, we catalogue all non-hydrogen bond, intermolecular interactions, that are only significant at relatively close range to the radical site in the crystal. It encompasses dispersion or van der Waals, steric hindrance and other dipole interactions taking place between the radical and closely neighbouring molecules in the crystal matrix.

A problem arises when trying to account for these interactions within a cluster approach, as they are often not as easily identified as hydrogen bonds. Specifically, the number and selection of surrounding lattice molecules that have to be included within the cluster can be arbitrary and to avoid this, objective criteria must be introduced.

Most easy is to consider one pristine crystal molecule as a perfect sphere, and calculate its radius. If we take this sphere as a rough measure for the molecular volume and put its center at the center of mass of a chosen central molecule within the lattice, we can make a selection by including all molecules in the cluster that have at least one atom within this sphere. Adding to this cluster any hydrogen bonding molecules (if necessary) already accounts for a good deal of short-range interactions in most cases, for a fairly limited cluster size. If the volume of the sphere is increased, more molecules will be selected and consequently larger cluster sizes can be reached, although this strategy is prone to bias.

A more elaborate, independent selection criterion is again to choose one molecule of the lattice but now put similar spheres on every atom instead of only at the center of mass. A bigger cluster model space is then obtained by considering all surrounding molecules with at least one atom in one of the spheres. In the latter selection model, one can account for the possible asymmetry of the central radical.

Long-range interactions

Electrostatics and some dispersion effects are the only interactions that can influence the electrons of a central radical at a relatively large distance within the crystal. To account for these in a cluster approach would involve huge clusters, containing several hundreds of molecules. This is obviously computationally unfeasible within a supermolecule approach. Possibly, one could include these interactions by using point charges in addition to an already large supermolecule cluster, as mentioned earlier. In this work, however, we have never applied such schemes.

Level of theory

Of course, even calculations with extremely large clusters will render disappointing results, if they are not treated at a reasonable **level of theory**. In this work, all ab-initio cluster calculations have been performed within Density Functional Theory. Not only does this method provide a cost-effective implementation of electron correlation, it is also acceptable in the description of hydrogen bonds [4], which are of basic importance when dealing with organic crystals. In literature, some Van der Waals interactions have also been treated with

DFT, but this is far from routine, since tailor-made density functionals are often required for a correct description of weakly bound systems [64]. However, even when neglecting long-range interactions, full ab-initio calculations with the considered cluster approach model spaces can become quite intense and are often restricted due to the limits of computational resources. This problem can be circumvented by adopting additional approximations – similar to e.g. the "multiplicative integral" approximation (MIA) for Hartree Fock, which is used quite successfully to study crystals [59, 65] – or by using a simplified Hamiltonian, as in semi-empirical or molecular mechanics methods (see Chapter 2). But although these methods are very attractive from a computational point of view, their empirical input limits their general applicability.

A possible alternative is the use of hybrid methods: the cluster model under study is subdivided into several parts or layers, each described at a different level of theory. The interesting parts of the system – the 'inner' layers – are treated at a high level of theory; the rest of the system – the 'outer' layers – are described by a computationally less demanding method. In this work we have in various cases employed a two-layered ONIOM approach [66] – as implemented in the Gaussian [30, 31] software packages – where the inner layer consists of the central radical and is treated at the ab-initio level. The outer layer, consisting of the other molecules in the cluster surrounding the radical, is treated at a semi-empirical level. The goal of this scheme is to describe the complete cluster at the highest level of theory through extrapolation, as illustrated in Figure 4.7.

Since the calculation of the full ab-initio energy (or wavefunctions/densities for that matter) for the complete cluster (point 4) is computationally very demanding, it is approximated through the energies of points 1 to 3. The energies at these points are easier to determine, either because they can be obtained at a low (semi-empirical) level (1 and 3) or because only the radical is considered (2). This ONIOM extrapolated energy can be easily obtained via the formula

$$E^{ONIOM}_{Extrapolated} = E^{Cluster}_{semi-empirical}\left(2\right) - E^{Radical}_{semi-empirical}\left(1\right) + E^{Radical}_{ab-initio}\left(3\right)$$

and is only an approximation to the true high-level full-cluster energy (point 4), differing from it by an amount D:

$$E^{Cluster}_{ab-initio}\left(4\right) = E^{ONIOM}_{extrapolated} + D\,.$$

However, if the error D of the extrapolation procedure is constant for two different structures (e.g. subsequent steps in a geometry optimization) their relative energy will be evaluated correctly within the ONIOM scheme.

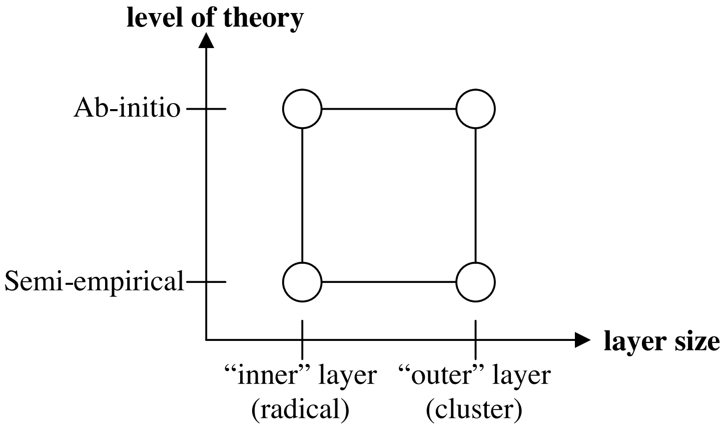

Figure 4.7: **Graphical representation of the ONIOM scheme.**

Convergence problems

Ideally, one could expect the accuracy of the calculation to only increase when the cluster size is expanded. Therefore, one could argue that it is always better to use the largest clusters possible, in terms of available computer time. Unfortunately, quite often convergence problems occur when performing calculations on relatively large clusters. This is mainly caused by pushing the software capabilities to their limits and occurs especially whenever the global minimum on the conformational hyperenergy surface of the radical within the cluster is not easy to locate (e.g. when the energy surface around the minimum is relatively flat). Time, software enhancements and the ever-increasing complexity and availability of computer resources will eventually solve these problems and we have already witnessed such improvements in the transition from Gaussian 98 [30] to Gaussian 03 [31]. In the mean time one must be cautious with all cluster calculations and analyse their results thoroughly and make sure that no inconsistencies occur.

EPR calculations

Once an optimized geometry is obtained in a cluster approach, its spectroscopic parameters can be readily calculated. However, one is left with a choice for the size of the model space for this EPR calculation: either to incorporate the entire cluster, or to consider just the central radical. When adopting the latter strategy, the EPR parameters are actually determined in a single molecule approach, thus drastically reducing the original size of the cluster model space. This reduction is particularly attractive from a purely computational point of view, as it presents an effective way of reducing computer time, without losing too much of a qualitative insight on the EPR parameters of the radical.

Nevertheless, such a single molecule treatment is somewhat naïve because the surrounding molecules of the crystal lattice will exert – at least to some extent – a certain influence on the electronic ground-state configuration of the central radical. For instance, if a radical is subject to one or more hydrogen bonds within the crystal lattice, the unpaired spin density of the involved atom on the radical will be slightly altered by delocalization effects towards the lattice molecules [4]. Hence, it can be expected that the hyperfine coupling constants will change accordingly. Even more spectacular influences can be expected for the orientations of the hyperfine tensor principal axes. As was illustrated in section 3.6, several types of hyperfine tensors are characterized by (quasi-)axial symmetry, in which the two principal directions with intermediate and minor eigenvalues are degenerate. It is primarily the molecular environment of the radical that will break this degeneracy. Hence, if such a crucial part of the crystal is not incorporated in the model space of the EPR calculation, it is likely that the orientations of the latter two eigenvectors will be incorrectly predicted. In that case, only the plane of the degenerate eigenvectors – perpendicular to the principal direction with the major, non-degenerate eigenvalue – will be completely defined and a rotation of the former two principal axes about the latter well determined axis will be necessary. On the other hand, since the non-degenerate eigenvector will not be influenced as much by the intermolecular interactions, this axis is most indicative of the quality of the EPR calculation and the associated radical geometry.

So, in general, an EPR calculation in which the full cluster is considered will normally result in more satisfying results than one that only deals with the central radical. The former model space approach, on the other hand, will require extensive computational resources, whereas the latter approach will be at least a hundred times faster and will usually generate representative EPR parameters that still allow a qualitative analysis.

In any case, information regarding the precise orientation of the optimized radical geometry with respect to the crystal axes is known exactly from the preceding cluster geometry optimization. The determination of the hyperfine tensor axes therefore poses no immediate difficulty, since they can be easily referenced to the crystal axes reference frame by means of a simple coordinate transform, as outlined in Figure 4.4.

4.2.3 Periodic approach

In a periodic approach, the model space consists of the actual crystal lattice, in which a certain amount of radical defects has been introduced. This is usually done by creating, conform the crystal structure, a unit cell that contains one radical and several other intact molecules. This cell rarely corresponds with that of the original crystal (always containing four molecules in the discussed examples), because it must be ensured that the radical defects are well separated from each other.

Consequently, the initial unit cell of the crystal is usually doubled in one or more crystal directions (e.g. along the a- and c axes). This supercell is then repeated periodically in all directions, to simulate a crystal in which all intermolecular interactions between radical and lattice molecules are accounted for. This approach is clearly a more natural way of describing the solid state than the cluster approach, as it does not depend on an arbitrary selection of molecules with which a central radical may interact. As a result, less convergence problems occur. We have therefore applied such methods in this thesis for completeness and to primarily validate single molecule or cluster approach results. However, these methods and the underlying theoretical principles are not the scope of this work. We gladly refer to [10, 67], for more specific, technical details and an exhaustive discussion of this elegant approach.

Geometry Optimization

Throughout this work, we will make use of the “Ab-Initio Quantum Molecular Dynamics (AIMD)” [68] and the “Car-Parrinello Molecular Dynamics (CPMD)” [69] software codes to perform geometry optimizations in a periodic framework. Both methods rely on a simulated annealing technique – proposed by Car and Parrinello [70] – in which the interatomic forces are calculated on the "fly" from the instantaneous electronic potential. This way, the electronic and nuclear degrees of freedom are minimized simultaneously, basing on the DFT formalism. For these very complex calculations to be computationally feasible, pseudopotentials are used to describe the core region of an atom and only valence electrons are treated explicitly. Their corresponding single particle orbitals are expanded in plane waves, which make a maximal advantage of the periodicity of the crystal. The fluctuations that can be described by the plane wave expansion are determined by the energy cutoff in the momentum space of the kinetic energy. The lower this value, the more plane waves are taken into account.

EPR calculation

Up to now, no program packages are available that allow the calculation of EPR data using the full periodic model space. This is regrettable because such an approach would provide spectroscopic parameters that take into account all possible intra- and intermolecular interactions taking place in the crystal. The implementation of such a routine in current periodic codes presents a great challenge in theoretical chemistry.

In absence of such a method, we must perform in the mean time the EPR calculations in a single molecule approach. This is quite easy because the hyperfine tensor axes can again be referenced directly to the crystal axes, which were comprised in the model space during optimization. Evidently, such a treatment implies that all intermolecular interactions in the crystal lattice will be neglected.

Although it could be proposed to incorporate some of the neighbouring molecules along with the radical in a cluster approach for the EPR calculation, the arbitrariness of the selection procedure makes such a method unfavorable. Furthermore, this cluster model space does no longer represent an actual energetic minimum for the conformational space of the radical, because its structure was optimized at a superior level of theory.

Chapter 5. Radiation-induced radicals in L-α-alanine

REFERENCE: [71], [72].

5.1 BACKGROUND

The amino acid L-α-alanine is one of the most intensively studied amino acids, mainly because of the properties it displays in the solid-state form. More specifically, upon irradiation of solid alanine, a variety of stable radicals is produced within the lattice. These radicals are ideally suited for Electron Paramagnetic Resonance (EPR) dosimetry, owing to several interesting dosimetric characterics, such as good dose-yield factors, linear signal response over a wide range of radiation doses, excellent fading characteristics and small dependency of temperature, humidity, and other environmental factors [73]. Due to its overall high quality and small costs, it is therefore widely used for reference and routine dosimetry in radiation therapy, biological research, as well as in industrial facilities for high-dose irradiation, including applications in food preservation or sterilization of medical supplies.

Figure 5.1: An example of an alanine dosimeter system (here in the form of pellets), as supplied by the National Physics Laboratory (http://www.npl.co.uk).

With respect to this application, numerous EPR and ENDOR studies on L-α-alanine have produced large amounts of experimental data concerning the electronic g-factor and the hyperfine coupling constants (hfcc's) of magnetic nuclei in alanine-derived radicals [74].

It has been commonly assumed that the solid-state radical population of L-α-alanine at room temperature consisted of only one radical type, the so-called Stable Alanine Radical (SAR) or R1 as shown in Figure 5.2, and that all variations in the EPR spectrum could be ascribed to various properties of this radical [75]. This radical is formed by deamination from a protonated alanine radical anion, and was first detected in a single crystal by van Roggen et al. [76] and later refined by

Miyagawa et al. [77]. Speculations had been made on the possible co-existence of several stable radical species [78]. Only recently however, Sagstuen et al. [79, 80] presented compelling experimental evidence in a combined EPR, ENDOR and EIE study of irradiated solid-state alanine for the existence of two more radiation-induced radicals, R2 and R3 (Figure 5.2). The figure also includes the primary radical anion, which can only be observed at low temperature (77 K). Radical R2 is a hydrogen-abstraction product, and contributes substantially (40%) to the solid-state radical population, while R1 is the most found species (60%) [79]. Radical R3 is a minority species, which is produced by hydrogen-abstraction followed by proton-transfer.

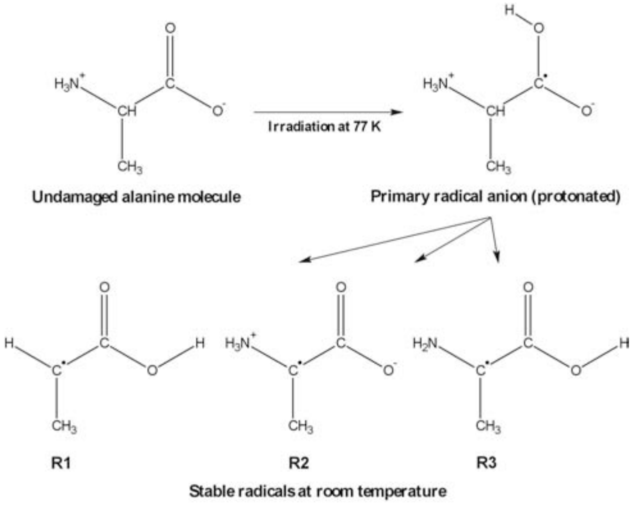

Figure 5.2: L-α-alanine and derived radicals.

Due to the importance and applications of the alanine dosimetric system, quite a few theoretical studies have been performed on their radiation-induced radicals. While some have rather concentrated on the mechanisms of radical formation within the solid state [81, 50], others have tried to reproduce the experimental EPR data and consequently confirm the proposed structures [82, 83]. Here, we also adhere to the second point of view and we will focus on model systems of alanine in the presence of its molecular environment in the crystal lattice. We specifically target the R2 radical, as it is the simplest adduct of alanine, and we can expect the abstracted hydrogen to disturb the crystal lattice in a minor way. We will use the experimental data from [79] to compare our calculations with. These are – in part – reproduced in Table 5.1.

Experimental results for alanine R2					
	Aiso	Taniso	Axes		
N	7.3	-1.8	-	-	-
		0.9	-	-	-
		1.0	-	-	-
β1(NH3)	86.3	-6.9	0.709	0.289	0.643
		-2.7	0.182	0.806	-0.563
		9.5	0.681	-0.516	-0.519
β2(NH3)	30.2	-6.1	0.310	-0.949	0.061
		-4.7	0.314	0.163	0.935
		10.7	0.897	0.270	-0.349
β3(NH3)	10.2	-4.9	0.862	0.481	0.159
		-4.8	0.466	-0.876	0.123
		9.7	0.199	-0.032	-0.980

Table 5.1: Aiso, Taniso are given in MHz; direction cosines with respect to a, b and c crystal axes are also presented here.

Since alanine – as all other amino acids – adopts the zwitterionic form in the crystalline state and in solution, zwitterionic radicals can be formed upon irradiation, such as R2. Numerous theoretical studies have been performed on amino acids and their derived radicals in the zwitterionic form [84]. But high-level ab-initio calculations on the simplest amino acid glycine have shown that the zwitterionic form is not the energetically most favoured structure in vacuo. Instead, the molecule undergoes intramolecular proton transfer from the amino group to one of the oxygen atoms to adopt the non-ionic form [85]. Similar conclusions have been formulated for alanine [86]. Correspondingly, Barone and Adamo showed that the zwitterionic form for an isolated glycine radical does not correspond to a stationary point [87]. Consequently, in order to study amino acids, like alanine or one of its derived radicals in solid state or solution, it is essential to account for intermolecular environmental effects.

In fairly recent ab-initio DFT calculations the hfcc's of selected nuclei in alanine-derived radicals were determined and analysed, consistently based on a single molecule approach. Lahorte et al. [83] performed calculations on alanine radicals in vacuo, where the radical structures were proposed from the experimentally available atomic positions of undamaged alanine and constrained geometry optimizations had to be performed on this structure in order to prevent the intramolecular hydrogen transfer. Ban et al. [82] kept the radicals in their zwitterionic forms during geometry optimization by using a continuum model [88]. In this Onsager model, the radical under study is placed in a cavity surrounded by a continuum with a uniform dielectric constant.

Despite the fact that environmental modeling in both approaches of Ban and Lahorte is inadequately described or even completely omitted, both studies succeed in reproducing in a satisfactory way the experimental isotropic hfcc values, albeit only after adopting some crucial but acceptable assumptions. The agreement is only achieved after rotating the amino group about a specific angle, as will be discussed later. This assumption is justified to account for the missing environmental forces in the models like hydrogen bridges, but they remain speculative and deserve a more elaborate study by taking into account an adequate modeling of the crystalline environment, as the neighbouring molecules will affect the geometry of the radicals in the solid state and hence the hyperfine coupling constants. To this end, we have performed a similar theoretical study of the radiation-induced R2 radical in alanine, but in which enhanced model spaces were used and higher levels of theory were accessed.

5.2 MODEL SELECTION AND COMPUTATIONAL DETAILS

More specifically, an enhanced model space for alanine was obtained by placing discrete molecules around the target radical, either in a cluster approach or using a periodic treatment. In both approaches, full geometry optimizations were performed on the central radical, while keeping the coordinates of the surrounding alanine molecules fixed in space at the experimental geometry.

5.2.1 Cluster approach

One central molecule was surrounded by alanine molecules according to the space group symmetry $P_{2\perp 2\perp 2\perp}$ of the L-α-alanine crystal [89]. The orthorhombic unit cell contains four alanine molecules and has unit cell constants of a=6.025 Å, b=12.324 Å and c=5.783 Å. Both the number of neighbours taken into account and the level of theory at which they are described, were varied. Table 5.2 gives an overview of all applied methods, and their short abbreviations for later reference. The methods used in earlier theoretical calculations [82, 83] are also added for comparison (B3LYP/0/0 and B3LYP/Onsager/0).

Software package	Central radical/molecule	Surrounding alanine cluster	Notation
Gaussian98	PM3	14 molecules, PM3	PM3/PM3/14
Gaussian98	PM3	6 molecules, PM3	PM3/PM3/6
Gaussian98	B3LYP/6-31G**	14 molecules, PM3	B3LYP/PM3/14
Gaussian98	B3LYP/6-31G**	6 molecules, PM3	B3LYP/PM3/6
Gaussian98	B3LYP/6-31G**	14 molecules, AM1	B3LYP/AM1/14
Gaussian98	B3LYP/6-31G**	6 molecules, AM1	B3LYP/AM1/6
ADF1999	BLYP/I	6 molecules, BLYP/I	BLYP/I/6
ADF1999	BLYP/II	6 molecules, BLYP/II	BLYP/II/6
ADF1999	BLYP/III	6 molecules, BLYP/III	BLYP/III/6
AIMD	BP86/PW	15 molecules, BP86/PW	BP86/PW
Gaussian94	B3LYP/6-31G*	0 molecules	B3LYP/0/0
Gaussian94	B3LYP/6-31+G**	Onsager model of water	B3LYP/Onsager/0

Table 5.2: Schematic overview of applied methods.

Two clusters with different sizes were constructed, one containing only 7 alanine molecules and one containing 15 molecules. The small cluster was obtained by considering only those molecules that are engaged in hydrogen bonds with atoms of the central molecule. The structure of the resulting hydrogen bond cluster model is shown in Figure 5.3, where the six hydrogen bonds are apparent between the hydrogen and oxygen atoms of the central alanine and those of the six neighbouring molecules. The methods PM3/PM3/6, B3LYP/PM3/6, B3LYP/AM1/6, BLYP/I/6, BLYP/II/6 and BLYP/III/6 refer to this cluster model.

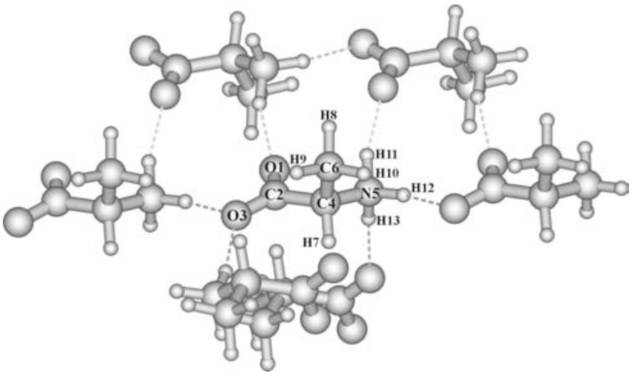

Figure 5.3: Cluster model accounting for all hydrogen bonds with a central alanine molecule.

A larger cluster of 15 L-α-alanine molecules was built by considering all surrounding molecules with at least one atom in one of the spheres with radius 3.7 Å, encircling every atom of the central molecule. The methods labelled PM3/PM3/14, B3LYP/PM3/14 and B3LYP/AM1/14 in Table 5.2 are based on this nearest neighbouring cluster model. To obtain initial geometries for the radical R2, one hydrogen atom (H_7) was abstracted from the central alanine molecule in both clusters.

Considering alanine as a benchmark system for the accuracy of cluster calculations on amino acids, the level of theory describing the central molecule (or radical) and its surrounding molecules was varied to determine its influence on the optimized geometry. A first set of calculations was done using a semi-empirical PM3 Hamiltonian [36], as implemented in the Gaussian 98 package [30]. The methods labelled PM3/PM3/6 and PM3/PM3/14 refer to this level of theory. Although the use of this simplified Hamiltonian circumvents common problems associated with high-level ab-initio modeling of chemical systems with a large number of atoms, their empirical input limits their general applicability [90]. A full ab-initio treatment of the cluster is more widely applicable, but is unfortunately very time consuming due to the limits on computational resources.

Several computations were nevertheless performed at this level, labelled by BLYP/I/6, BLYP/II/6 and BLYP/III/6 but only on the small cluster with six surrounding molecules. We used the Amsterdam Density Functional program (ADF1999) developed by Baerends et al. [29], as similar calculations performed with the Gaussian 98 software package posed some serious convergence problems in the SCF procedure. All the atoms of the system were described within the DFT framework with the use of the BLYP functional, featuring Becke's non-local exchange potential [21], combined with a correlation potential as proposed by Lee, Yang and Parr [22]. The I, II and III notations refer to the increasing size of the basis set in ADF nomenclature, employing Slater type orbitals as basis functions. They roughly correspond roughly to a single-ζ basis set, a double-ζ basis set and a double-ζ basis set extended with polarisation functions, respectively. To accelerate SCF convergence, we used the electron-smearing option [91]: electrons were smeared out in an interval of 0.02 a. u. over orbitals that lie around the Fermi level.

Calculations were also performed using hybrid methods, which contain ingredients of both extreme methods. A two-layered ONIOM approach was used [66] – as implemented in the Gaussian software package – with the inner layer consisting of the central alanine, which was described at the density functional level, engaging Becke's three parameter hybrid B3LYP functional [28] and expanding the molecular orbitals in a double-ζ 6-31G split valence basis augmented with single d and p polarisation functions [32]. Several studies [92] have indicated that this functional gives a reliable description of the geometry. The outer layer, consisting of either 6 or 14 alanine molecules, was treated at the semi-empirical level (PM3 [36] or AM1 Hamiltonian [35]). These ‘layered’ methods are referred to as B3LYP/PM3/6, B3LYP/PM3/14, B3LYP/AM1/6 and B3LYP/AM1/14. Intermolecular interactions (such as hydrogen bridges) between the central alanine molecule and its neighbors are always treated at the semi-empirical level in these methods.

5.2.2 Periodic approach

In the second approach – which shall be referred to as BP86/PW – the crystal phase was modeled by performing periodic calculations. To simulate a radical R2 in the crystal lattice, we doubled the unit cell in the a and c direction to ensure that the radical defects are well separated from each other. The resulting orthorhombic extended unit cell contains 15 alanine molecules and a central R2 radical, as is shown in Figure 5.4.

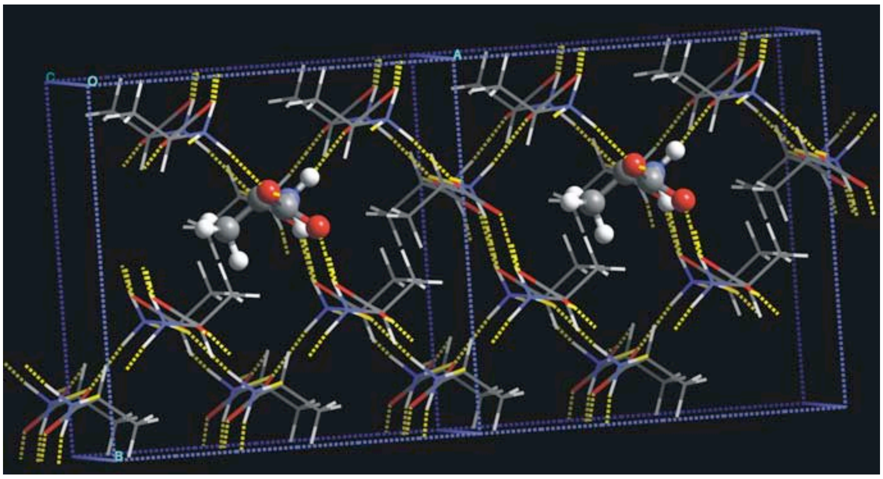

Figure 5.4: Two enlarged unit cells, as applied in the periodic approach.

The software package used for these calculations is the Ab-Initio Quantum Molecular Dynamics (AIMD) Package [93] based on the Car-Parrinello code [94]. This algorithm was first proposed in a broader context of molecular dynamics simulations, with interatomic forces calculated 'on the fly' from the instantaneous electronic potential. The simulated annealing technique was further used for the simultaneous optimization of the electronic and nuclear degrees of freedom towards a global energy minimum. This optimization scheme is based on a conjugate gradient minimisation of the energy functional [95]. In our calculations only the structure of the radical was optimized, while the coordinates of all other atoms of surrounding alanine molecules were kept fixed at the experimental geometry by use of the SHAKE algorithm [96].

The quantum mechanical description of the electronic structure is also based on the DFT formalism. The exchange-correlation energy functional is treated within the local density approximation for which we employed the Perdew-Zunger parameterisation for the homogeneous electron gas [23]. In addition, gradient corrections were included according to the schemes proposed by Perdew [24] and Becke [25], known as BP86. Only valence electrons are treated explicitly and their corresponding single particle orbitals are expanded in plane waves. Very soft pseudopotentials of the Vanderbilt type [97] are used to account for the core. An energy cut-off of 25 Ry (1 Ry = 1314 kJ/mol) is taken for the plane-wave expansion. Several other studies [98] have shown that this value is sufficient to describe the structure accurately.

5.2.3 EPR calculations

For all optimized geometries, the EPR parameters of the central radical have been calculated, using the Gaussian 98 software package within the DFT framework. The B3LYP [28] functional was used and all atoms were assigned a triple-ζ 6-311G basis augmented with single first d and p polarisation functions [33]. The electronic wave functions for the optimized geometries were thus recalculated at a high and uniform level in order to get EPR parameters constructed on the same basis. A DFT procedure with a BLYP or B3LYP functional was chosen in accordance with other studies [99], for the reason that the initial analysis of the EPR parameters will be mainly based on the correspondence between calculated and experimental (isotropic) hyperfine coupling constants.

5.3 VERIFICATION OF THE CLUSTER MODEL SPACE

To test the validity of the proposed cluster models, a first set of calculations was performed, in which the structure of one undamaged (!) L-α-alanine molecule was optimized within a cluster of alanine molecules, adopting the mentioned cluster methods and levels of theory. By mutually comparing the resulting geometrical parameters of the optimized central molecule, the various levels of theory can be assessed on their applicability and accuracy to model the crystal. In particular, those methods will be considered inaccurate or unreliable that drastically alter the geometrical parameters of the original crystal structure during the geometry optimization. In other words, the less structural changes a cluster model exacts during optimization, the better it will be. In Table 5.3, a summary is given of selected geometrical parameters as determined in various levels of theory and in experiment. For the optimized geometries, all values are reported relative to the absolute experimental value (calculated – experimental).

On average, all methods reproduce quite accurately the bond lengths. The PM3/PM3/6-14, B3LYP/PM3/6-14, B3LYP/AM1/6-14 and the BLYP/III/6 optimized geometries have an rms bond length error of about 0.005 Å, which is comparable with the average experimental standard deviation of 0.002 Å. We only notice some quite significant discrepancies in the BLYP/I/6 results; deviations in bond lengths of the order of 0.2 Å with experiment (e.g. N_5-H_{13}) are too high to be acceptable in any way. These large errors are probably due to the small sizes of the employed basis sets. The bond angles are on the average equally well reproduced by all methods, keeping in mind that the average standard deviation is 0.16° for the experimental bond angles.

	Experimental	PM3/PM3/6	PM3/PM3/14	B3LYP/PM3/6	B3LYP/PM3/14	B3LYP/AM1/6	B3LYP/AM1/14	BLYP/I/6	BLYP/II/6	BLYP/III/6
Bond Lenghts										
O1 - C2	1.242	0.011	0.008	0.017	0.014	0.026	0.020	0.061	0.047	0.018
C2 - O3	1.258	0.013	0.008	0.023	0.017	0.008	0.004	0.114	0.063	0.033
C2 - C4	1.531	0.007	0.016	-0.017	-0.009	0.003	0.007	0.134	0.008	0.011
C4 - N5	1.487	0.026	0.026	0.051	0.051	0.029	0.025	0.077	0.031	0.013
C4 - C6	1.524	-0.005	-0.008	0.005	0.002	0.006	0.005	0.048	0.025	0.012
C4 - H7	1.093	0.038	0.032	0.006	0.002	0.007	0.003	0.035	0.003	0.003
N5 - H11	1.029	-0.010	-0.006	0.018	0.025	0.013	0.022	0.054	0.010	0.005
N5 - H12	1.047	-0.026	-0.023	-0.001	0.003	-0.017	-0.016	0.165	0.009	0.006
N5 - H13	1.031	-0.006	-0.009	0.017	0.015	0.000	-0.005	0.194	0.038	0.040
C6 - H8	1.081	0.017	0.021	0.013	0.017	0.015	0.015	0.026	0.020	0.017
C6 - H9	1.082	0.017	0.021	0.009	0.013	0.007	0.011	0.022	0.014	0.012
C6 - H10	1.081	0.019	0.019	0.017	0.018	0.016	0.017	0.025	0.016	0.014
RMS		0.005	0.005	0.006	0.006	0.004	0.004	0.028	0.008	0.005
Bond Angles										
O1 - C2 - O3	125.6	-7.2	-4.9	1.4	2.9	0.9	2.0	-2.5	-2.1	-0.6
O1 - C2 - C4	118.4	2.8	0.9	-0.7	-2.3	-0.6	-2.1	2.8	1.6	0.5
O3 - C2 - C4	116.0	4.4	3.9	-0.6	-0.6	-0.3	0.1	-0.2	0.5	0.1
C2 - C4 - N5	110.0	-0.1	-0.4	-2.0	-2.4	-2.9	-4.6	4.3	-0.7	-1.0
C2 - C4 - C6	111.1	-1.2	-1.3	1.3	1.2	0.2	0.8	-2.4	1.2	1.1
C2 - C4 - H7	108.6	0.5	0.3	2.3	2.1	1.9	1.6	1.0	1.1	1.2
C4 - N5 - H11	111.3	-0.8	-0.3	-4.6	-4.3	-7.7	-8.6	-5.1	-0.7	-1.1
C4 - N5 - H12	109.4	-1.8	-1.8	1.1	1.0	4.0	4.8	0.3	-1.6	-0.2
C4 - N5 - H13	109.1	-0.3	-0.7	-1.2	-1.6	2.4	2.2	-0.5	0.2	0.6
C4 - C6 - H8	110.3	2.1	2.2	0.3	0.1	0.0	0.4	0.1	-0.2	0.0
C4 - C6 - H9	110.6	-0.8	-0.4	-2.7	-2.2	-2.2	-1.4	-0.4	-0.4	-0.5
C4 - C6 - H10	110.4	1.2	1.4	1.7	2.1	0.6	0.8	-0.3	-1.3	-0.9
N5 - C4 - H7	106.9	0.7	0.6	-1.8	-1.9	0.7	1.1	-1.0	-1.4	-1.1
C6 - C4 - H7	110.4	-1.7	-1.1	0.3	1.2	0.0	0.5	-1.0	-0.3	-0.3
H8 - C6 - H9	108.3	-0.5	-1.3	0.5	-0.2	0.8	0.0	0.6	1.0	1.0
H8 - C6 - H10	108.4	-0.1	-0.6	1.2	0.6	0.9	0.6	1.0	2.1	1.7
H9 - C6 - H10	108.9	-2.1	-1.5	-1.0	-0.3	-0.2	-0.5	-0.9	-1.2	-1.3
H11 - N5 - H12	108.1	1.3	1.6	5.6	6.1	3.4	3.2	-2.9	1.4	0.9
H11 - N5 - H13	110.7	0.0	-0.4	-4.1	-4.3	-1.7	-0.9	0.1	0.9	-0.7
H12 - N5 - H13	108.2	1.6	1.6	3.0	2.8	-0.5	-0.7	7.8	-0.3	0.6
RMS		0.5	0.4	0.5	0.6	0.5	0.6	0.6	0.3	0.2
Dihedral Angles										
O1 - C2 - C4 - N5	-18.7	-13.5	-12.3	-7.2	-8.2	0.6	-3.0	-21.3	-8.5	-8.1
O1 - C2 - C4 - C6	103.1	-12.1	-11.0	-8.1	-9.5	-1.2	-4.9	-21.2	-8.2	-8.0
O1 - C2 - C4 - H7	-135.4	-14.6	-12.9	-5.2	-5.7	0.2	-2.6	-23.3	-7.0	-6.9
O1 - O3 - C4 - C2	-0.1	1.4	2.0	-0.3	0.0	-1.0	0.3	-0.7	0.5	0.4
C2 - N5 - C6 - C4	34.0	0.5	0.8	0.1	0.5	1.6	2.4	-0.6	-0.5	-0.1
H11 - N5 - C4 - C2	58.3	9.0	7.4	-5.1	-4.8	-39.0	-36.4	-1.1	0.1	-0.7
H8 - C6 - C4 - C2	-64.4	3.9	0.6	6.8	5.3	2.1	5.5	3.1	-1.3	0.9
RMS		3.6	3.2	2.1	2.2	5.6	5.3	5.5	2.0	1.9
Hydrogen Bond Distances										
O1 - H177/H86	1.861	-0.025	-0.016	-0.030	-0.026	0.232	0.179	-0.199	0.073	0.098
O3 - H49/H23	1.828	-0.069	-0.068	-0.062	-0.058	0.067	0.020	-0.101	-0.146	-0.131
O3 - H113/H48	1.780	-0.033	0.011	-0.040	0.005	0.137	0.140	-0.206	-0.018	-0.016
H11 - O144/O66	1.861	0.055	-0.017	0.096	0.013	0.701	0.363	0.337	0.236	0.276
H12 - O54/O28	1.780	0.006	-0.006	-0.002	-0.011	0.428	0.362	-0.330	-0.108	-0.075
H13 - O119/O54	1.828	-0.051	0.005	-0.059	0.006	0.208	0.279	-0.477	-0.201	-0.211
RMS		0.018	0.012	0.023	0.011	0.149	0.104	0.123	0.061	0.065

Table 5.3: Summary of selected geometrical parameters for the various optimized geometries of an undamaged alanine. Units of bond lengths are Angströms. The H- and O- hydrogen bond partners in the last section are labeled conform their numbering in the 15 and 7 molecule clusters, respectively.

In the table, only those dihedral angles are shown that give essential insight into the chemical structure of the optimized central molecule. The position of the amino- and methyl group relative to the rest of the central alanine is characterized by the dihedral angles H_{11}-N_5-C_4-C_2 and H_8-C_6-C_4-C_2 respectively. The other hydrogen atoms lie in planes that form approximately 120° or 240° with respect to the (H_{11}, N_5, C_4) and (H_8, C_6, C_4) planes for the amino- and methyl group, respectively. The BLYP/II-III/6 calculations succeed in reproducing almost exactly the experimental dihedral angles. On the contrary, the B3LYP/AM1/6-14 calculations totally fail in reproducing the H_{11}-N_5-C_4-C_2 dihedral angle, indicating that hydrogen bonds are poorly described by the AM1 Hamiltonian. All methods succeed in predicting a satisfactory H_8-C_6-C_4-C_2 dihedral angle. The position of the methyl group is well described and this is probably due to the absence of any hydrogen bonds with one of the hydrogens of the methyl group. Two "improper" torsional angles are also included in Table 5.3: O_1-O_3-C_4-C_2 and C_2-N_5-C_6-C_4. The former is a measure of deviation from planarity of the C_2 carbon center. All optimized geometries point toward an almost planar conformation for the CO_2 group. The second improper torsional angle is a measure for the overall sp^3 character of the C_4 carbon center. Apart from the B3LYP/AM1/6-14 results, all other theoretical predictions are in excellent agreement with experiment. However, all these geometries show a significant and almost uniform deviation in the dihedral angles associated with oxygen O_1 (the first three dihedral angles reported in Table 5.3). Since the CO_2 group is planar and the overall sp^3 character of C_4 is preserved, the deviation of the dihedral angles indicates a rotation of the CO_2 group along the C_2-C_4 axis.

A further measure for the adequacy of the cluster models in giving a plausible description of the crystalline environment is the reproduction of the hydrogen bond lengths. These intermolecular distances are more sensitive to the method used to describe the cluster. They are also presented in Table 5.3, but in Figure 5.5, a graphical representation is given, where the hydrogen bond lengths in the various optimized geometries are cross-referenced with the actual bond lengths in the crystal structure. While Figure 5.5(a) presents these distances for all geometries obtained at levels of theory involving the 7 molecule cluster; similarly, those involving the 15 molecule cluster are given in Figure 5.5(b). The crystalline hydrogen bond lengths are represented by a thick black line, sided by two dashed lines corresponding to an error margin of ±0.01 Å.

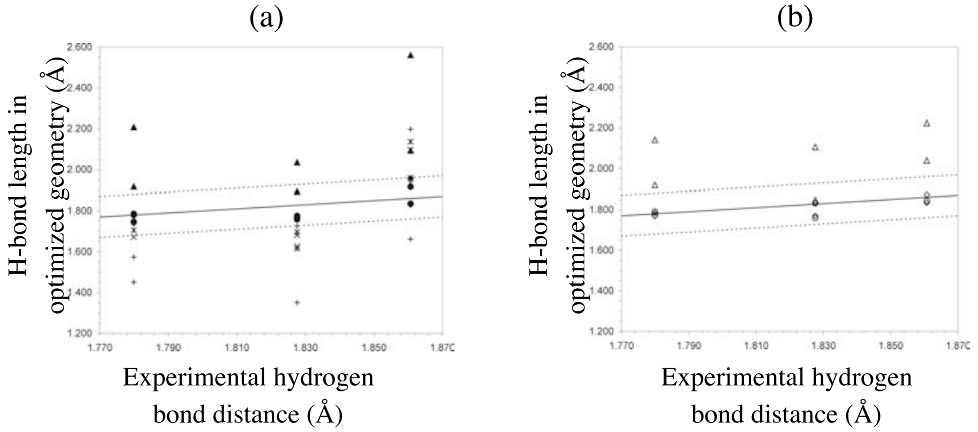

Figure 5.5: Experimental hydrogen bond lengths in relation to those of the optimized geometries. **(a)** presents information about the PM3/PM3/6 ( ), B3LYP/PM3/6 (•), B3LYP/AM1/6 ( ), BLYP/I/6 (+), BLYP/II/6 (×) and BLYP/III/6 (∗) levels of theory; **(b)** those of PM3/PM3/14 (○), B3LYP/PM3/14 (●) and B3LYP/AM1/14 ( ).

For this geometrical feature, the largest deviations are noticed at the B3LYP/AM1/6-14 and BLYP/I/6 levels of theory. This again indicates that the AM1 semi-empirical methods are inadequate to describe the hydrogen bonds. Deviations at the BLYP/I/6 level can probably be attributed to the small basis set used. Of all levels, only the hydrogen bonds of the PM3/PM3/6-14 and B3LYP/PM3/6-14 optimized geometries remain more or less within the ±0.01 Å interval, with rms errors of 0.01-0.02 Å. The corresponding rms errors for BLYP/II/6 and BLYP/III/6 are not as good (about 0.06 Å). The hydrogen bonds for these optimized geometries are therefore outside the ±0.01 Å accuracy region, but not as excessive as those of e.g. B3LYP/AM1/6-14.

Concluding, the proposed cluster models perform overall relatively well in describing the crystal, apart from the B3LYP/AM1/6-14 and BLYP/I/6 methods. The poor performance of the latter method can be ascribed to an inadequate basis size, while the former methods completely fail to correctly describe hydrogen bonding, owing to the AM1 parameterized Hamiltonian. Cluster methods involving the PM3 Hamiltonian perform somewhat better in the description of hydrogen bonds, undeniably a manifestation of its valid semi-empirical input.

5.4 IDENTIFICATION OF THE RADIATION-INDUCED RADICAL R2 OF L-α-ALANINE

In a second set of calculations, the radiation-induced radical R2 was examined, by taking into account an adequate modeling of the alanine crystalline environment through the use of the proposed (and validated) model spaces. Starting from an initial radical geometry, optimizations were performed using either a cluster or periodic approach and consequently EPR calculations were carried out on the resulting optimized geometries, as sketched in the computational details. For the cluster model calculations, we will again refer to the same notations as mentioned earlier but with the difference that now a central R2 radical is considered instead of an intact alanine molecule. Even cluster models that were previously deemed not apt to simulate the solid state were still employed, in an attempt to extend the previous conclusions with respect to radical systems.

In this section, we will first discuss the impact of the different model space approaches on the geometry of the studied radical, in comparison with the results of other theoretical studies. In a second part, the isotropic and anisotropic hfcc's of the magnetic nuclei in the radical R2 are reported for all optimized geometries and a detailed evaluation of the theoretically predicted EPR parameters will be made, mainly based on the agreement of the calculated isotropic hyperfine coupling constants with experimental values.

5.4.1 Effect of model space on radical geometry

In Table 5.4, a summary of selected geometrical parameters is given for the various optimized geometries. We also report on the geometries predicted by Lahorte et al. [83] and Ban et al. [82]. These parameters include bond lengths, selected bond- and dihedral angles and hydrogen bond distances. The numbering of the atoms in the radical is conform that in Figure 5.6.

	B3LYP/0/0	B3LYP/Onsager/0	PM3/PM3/14	PM3/PM3/6	B3LYP/PM3/14	B3LYP/PM3/6	B3LYP/AM1/14	B3LYP/AM1/6	BLYP/I/6	BLYP/II/6	BLYP/III/6	BP86/PW
Bond lenghts												
O1-C2	1.271	1.277	1.254	1.251	1.261	1.264	1.272	1.277	1.335	1.317	1.278	1.285
C2-O3	1.242	1.295	1.264	1.272	1.282	1.292	1.270	1.277	1.399	1.339	1.302	1.307
C2-C4	1.511	1.507	1.507	1.500	1.466	1.455	1.468	1.464	1.540	1.450	1.465	1.467
C4-N5	1.492	1.478	1.460	1.458	1.503	1.503	1.465	1.466	1.563	1.489	1.472	1.464
C4-C6	1.479	1.478	1.463	1.461	1.487	1.484	1.478	1.475	1.547	1.492	1.484	1.483
H7-C6	1.102	1.100	1.105	1.099	1.107	1.103	1.104	1.101	1.118	1.110	1.107	1.114
H8-C6	1.093	1.090	1.103	1.097	1.094	1.090	1.092	1.087	1.105	1.096	1.093	1.103
H9-C6	1.102	1.100	1.102	1.133	1.102	1.107	1.104	1.112	1.110	1.104	1.102	1.106
H10-N5	1.023	1.030	1.024	1.005	1.058	1.053	1.044	1.040	1.100	1.047	1.043	1.064
H11-N5	1.025	1.030	1.025	1.015	1.055	1.051	1.038	1.034	1.125	1.057	1.054	1.109
H12-N5	1.037	1.052	1.024	1.025	1.052	1.057	1.039	1.043	1.222	1.076	1.078	1.054
Bonding angles												
O1-C2-O3	133.0	128.1	120.6	118.0	126.7	124.9	127.1	125.0	117.7	121.8	123.8	124.2
O1-C2-C4	111.3	113.5	117.0	120.6	116.4	118.2	116.2	117.3	127.6	119.1	117.9	116.2
C2-C4-N5	108.4	111.4	116.2	115.3	112.7	114.2	112.2	113.3	116.4	115.7	115.5	114.8
C2-C4-C6	131.8	130.2	122.1	124.1	124.5	126.7	128.4	128.9	114.7	125.7	125.1	119.6
Dihedral angles												
O1-C2-C4-C6	180.0	180.0	122.7	120.5	115.3	125.7	153.8	163.8	99.5	137.8	134.4	114.7
O1-C2-C4-N5	0.0	0.0	-46.2	-56.9	-32.8	-32.1	-24.0	-25.3	-32.2	-27.8	-27.4	-29.7
O3-C2-C4-C6	0.0	0.0	-59.9	-63.9	-66.2	-55.6	-28.2	-17.3	-83.9	-43.0	-46.0	-61.5
H8-C6-C4-C2	0.0	0.0	26.2	351.3	34.6	23.1	9.2	355.6	42.5	9.0	14.1	42.6
H10-N5-C4-C2	82.4	79.0	82.4	80.4	71.0	73.5	10.8	10.8	60.4	77.8	75.2	71.8
Improper torsion angles												
O1-O3-C4-C2	0.0	0.0	1.5	2.5	0.8	0.7	1.1	0.6	1.7	0.4	0.2	-2.2
C2-N5-C6-C4	0.0	0.0	6.6	1.6	17.2	11.6	1.2	-4.8	26.0	7.7	9.9	20.1
Hydrogen bonding distances												
O1-H176/H85	?	?	1.835	1.831	1.871	1.863	2.128	2.128	1.611	2.103	2.102	2.015
O3-H48/H22	?	?	1.781	1.734	1.777	1.800	1.915	1.943	1.787	1.740	1.762	1.778
O3-H112/H47	?	?	1.813	1.745	1.790	1.758	1.947	1.969	1.474	1.739	1.743	1.490
H10-O143/O65	?	?	1.842	2.510	1.813	1.870	2.700	2.929	2.038	1.944	1.995	1.832
H11-O53/O27	?	?	1.763	1.758	1.757	1.786	2.466	2.516	1.753	1.752	1.773	1.522
H12-O118/O53	?	?	1.835	1.745	1.833	1.780	2.384	2.278	1.374	1.708	1.679	1.847

Table 5.4: Summary of selected geometrical parameters for the various optimized radical geometries.

In analogy with the earlier discussion, the position of the amino- and methyl group relative to the rest of the central radical is given by the dihedral angles H_{10}-N_5-C_4-C_2 and H_8-C_6-C_4-C_2 respectively. The other hydrogen atoms again lie in planes at approximately 120° or 240°. No bond angles involving hydrogen atoms are mentioned as they all lie around 110°. Two 'improper' torsion angles are also presented, namely O_1-O_3-C_4-C_2 and C_2-N_5-C_6-C_4. The first is a measure of deviation from planarity of the C_2 carbon center. As is clear from Table 5.4, all optimized geometries point towards an almost planar conformation for the CO_2 group. The second improper torsion angle C_2-N_5-C_6-C_4 indicates the deviation from planarity of the radical backbone, which is formed by the atoms N_5, C_4, C_6 and C_2, and is thus a measure for the sp^3 character of the radical center C_4. It turns out that all optimized geometries deviate from planarity but that the deviation largely depends on the employed level of theory. The maximum deviation amounts to 26° in the BLYP/I/6 optimized geometry, while it is close to 0° in B3LYP/AM1/14 and

PM3/PM3/6. On average, the deviation from planarity remains still 7° and this is remarkable as it was previously always assumed in both experimental and theoretical studies, that upon hydrogen abstraction from C_4, the carbon atom transforms from an sp^3 to a perfectly planar sp^2 center. Our calculations do not support this picture. The interactions with the neighbouring molecules force the central radical into a non-planar conformation. This non-planarity of the radical backbone can be observed in Figure 5.6, displaying the optimized geometry of only the central radical at the B3LYP/PM3/6 level.

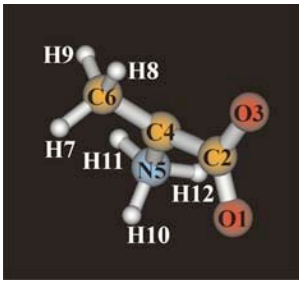

Figure 5.6: B3LYP/PM3/6 optimized geometry of the central alanine radical.

We notice a strong correlation between the non-planarity of the radical backbone and the rotation of the CO_2 group relative to the reference (C_2, N_5, C_6) plane of the radical backbone. This is best illustrated in Figure 5.7 where we plot the two relevant parameters characterizing the two above-mentioned features for each level of theory.

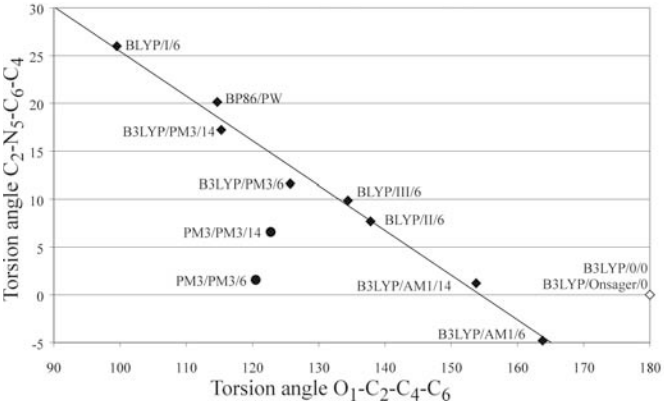

Figure 5.7: Relation between the torsion angle O_1-C_2-C_4-C_6 with respect to the C_2-N_5-C_6-C_4 angle in the various optimized geometries, obtained at different levels of theory: the ONIOM or ab-initio optimized geometries (●) and the purely semi-empirical optimized geometries ( ). In addition, the results of earlier theoretical calculations are indicated (●).

The dihedral angle O_1-C_2-C_4-C_6 determines the rotation angle of the almost planar O_1-O_3-C_2-C_4 constellation with an angle of 180° referring to the planar conformation. We observe an almost linear behaviour between the non-planarity of the radical backbone and the CO_2-rotation. This is a very striking result, which can be explained by considering the π-system of the CO_2 group. When the position of this group would not be influenced by attracting hydrogen bonds, the associated π-cloud would be oriented parallel to the lone electron orbital (LEO) on carbon C_4. The LEO conjugates with the π-cloud of CO_2 and the radical carbon center is stabilised by the effect of resonance stabilisation. However, when strong hydrogen bonds force the CO_2 group to shift out of the plane of the radical backbone, the π-cloud gets rotated relative to the direction of the LEO and is no longer parallel, resulting in a diminished conjugation. Since, in this case, sp^2 hybridisation of the C_4 carbon does not cause an overall stabilisation of the radical, the atom has some sp^3 character as well.

Methods which substantially differ from the quasi-linear pattern in Figure 5.7 are systematically described at a lower level of theory. Both PM3/PM3/6-14 models describe the central molecule within the semi-empirical approach of PM3, which is clearly insufficient. Hence, the deviation from planarity of the radical backbone is a direct consequence of the appearance of hydrogen bonds which induce a rotation of the CO_2 group, forcing the radical center to a non-planar conformation. It should be stressed that the strong hydrogen bonds only take place between the oxygen atoms and the amino protons, as was already apparent in Figures 5.3 and 5.4. Methyl protons are not involved in any hydrogen bond and remain submitted to quasi-free rotations, in contrast to the amino protons whose internal rotations are completely hindered by the hydrogen bonds. The strength of the hydrogen bond is therefore a determining factor to which extent the radical backbone deviates from planarity.

The stern effect of the simulated molecular environment on the optimized radical geometry is illustrated in Figure 5.8, where the relative B3LYP and ONIOM extrapolated energies are plotted as a function of the rotation angle of both the methyl and amino groups.

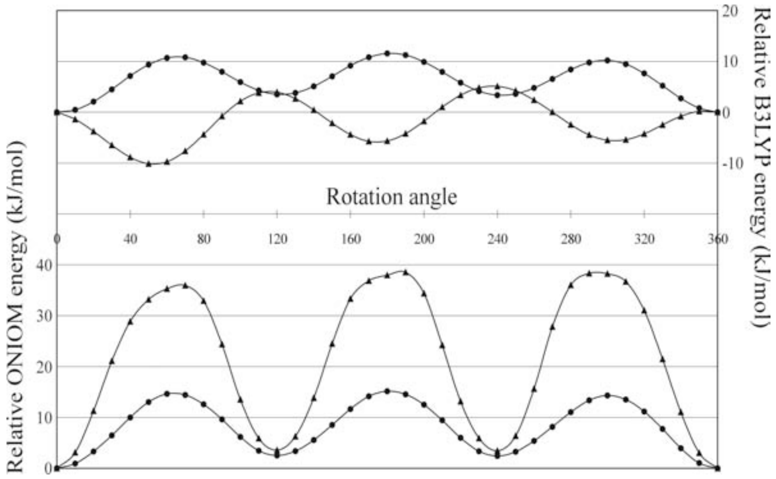

Figure 5.8: B3LYP/6-31G** energies versus ONIOM extrapolated energies relative to the energy of the optimized B3LYP/PM3/14 geometry as a function of the rotation angle for both the methyl ( ) and amino ( ) group (ONIOM extrapolated energy = -324.877522 a.u.; B3LYP/631G** energy = -323.034459 a.u.).

This plot was obtained by gradually rotating the methyl and amino group, starting from the B3LYP/PM3/14 optimized geometry, while keeping all other geometrical parameters fixed, and along the way determining the B3LYP/6-31G** energies for the central radical alone and the ONIOM extrapolated energies for the whole cluster. Quite striking in this figure is the fact that the starting geometry at 0º (the actual B3LYP/PM3/14 optimized geometry) does not represent a minimum for the amino group rotation. On the other hand, the ONIOM extrapolated energy of the starting geometry turns out to be a minimum, since in this case the molecular environment is included. Consequently, the surrounding alanine molecules in the cluster force the central radical to attain a conformation that does not correspond to an energetically most favoured structure in vacuo (at the B3LYP level). A similar effect is not observed for the methyl group rotation, corroborating that this internal motion is a quasi-free rotation in the crystal lattice.

5.4.2 Analysis of the calculated EPR parameters

Based on the match between calculated EPR parameters and experimental data, a final assessment was made of the considered model space approaches and their performance to yield correct structures for the radiation-induced radicals in L-α-alanine. Since all EPR parameters were calculated at a high and uniform level, the possible differences between the approaches can hence be solely attributed to geometrical features rather than to methodological grounds. However, the assessment was based predominantly on the agreement of the isotropic and anisotropic hyperfine coupling constants. The calculated values for these parameters are listed in Table 5.5 for all optimized geometries.

	Experimental				B3LYP/0/0				B3LYP/Onsager/0				PM3/PM3/14				PM3/PM3/6			
	A_{iso}	T_{xx}	T_{yy}	T_{zz}	A_{iso}	T_{xx}	T_{yy}	T_{zz}	A_{iso}	T_{xx}	T_{yy}	T_{zz}	A_{iso}	T_{xx}	T_{yy}	T_{zz}	A_{iso}	T_{xx}	T_{yy}	T_{zz}
O_1													**-2.6**	-48.8	22.4	26.3	**-0.4**	-47.1	21.7	25.5
C_2													**-28.6**	-5.9	2.5	3.4	**-30.7**	-5.7	2.6	3.1
O_3													**-0.7**	-44.0	19.4	24.6	**-2.6**	-59.4	28.1	31.3
C_4					**94.0**	-77.5	-76.4	153.9					**82.0**	-70.0	-68.2	138.2	**71.5**	-67.8	-66.4	134.2
N_5	**7.3**	-1.8	0.9	1.0	**-8.0**	-0.5	0.2	0.4					**-3.7**	-0.4	-0.1	0.5	**-6.5**	-0.3	-0.1	0.4
C_6					**-31.6**	-2.4	-0.4	1.9					**-28.9**	-1.9	-0.1	2.1	**-28.7**	-1.7	-0.4	2.1
H_7									**95.5**	-4.6	-3.4	8.0	**114.3**	-4.4	-2.8	7.3	**61.4**	-4.0	-3.2	7.2
H_8	**70.8**	-2.9	-2.7	5.6	**68.4**	-4.7	-3.8	8.5	**2.2**	-4.1	-3.9	8.0	**11.6**	-3.9	-3.5	7.4	**6.5**	-3.9	-3.0	6.9
H_9									**95.7**	-4.6	-3.4	8.0	**53.9**	-4.1	-3.7	7.7	**111.7**	-3.9	-3.2	7.1
H_{10}	**86.3**	-6.9	-2.7	9.5	**80.3**	-5.5	-4.8	10.3	**86.0**	-4.8	-4.5	9.3	**86.8**	-5.2	-4.8	9.9	**76.2**	-5.3	-4.7	10.1
H_{11}	**10.2**	-4.9	-4.8	9.7	**13.9**	-5.2	-4.4	9.6	**12.0**	-4.9	-4.5	9.4	**12.1**	-5.5	-4.4	9.9	**8.0**	-5.2	-4.0	9.2
H_{12}	**30.2**	-6.1	-4.7	10.7	**29.9**	-5.9	-5.3	11.3	**30.0**	-5.6	-4.9	10.6	**23.8**	-5.4	-4.6	9.9	**32.6**	-4.8	-4.5	9.3

	B3LYP/PM3/14				B3LYP/PM3/6				B3LYP/AM1/14				B3LYP/AM1/6				BLYP/I/6			
	A_{iso}	T_{xx}	T_{yy}	T_{zz}	A_{iso}	T_{xx}	T_{yy}	T_{zz}	A_{iso}	T_{xx}	T_{yy}	T_{zz}	A_{iso}	T_{xx}	T_{yy}	T_{zz}	A_{iso}	T_{xx}	T_{yy}	T_{zz}
O_1	**-0.9**	-37.6	15.0	22.6	**-0.7**	-37.7	14.6	23.2	**-2.1**	-28.5	12.3	16.2	**-1.0**	-29.1	12.3	16.8	**1.0**	-43.9	15.3	28.6
C_2	**-23.9**	-7.5	2.4	5.1	**-28.4**	-8.1	3.2	5.0	**-32.8**	-8.6	3.4	5.2	**-33.1**	-9.1	3.4	5.7	**-21.0**	-8.8	3.5	5.3
O_3	**-4.8**	-49.5	23.4	26.2	**-6.2**	-62.0	29.3	32.7	**-4.8**	-48.5	21.8	26.7	**-6.6**	-58.1	26.3	31.9	**-10.7**	-106.0	50.3	55.8
C_4	**152.3**	-67.8	-66.3	134.1	**116.9**	-67.0	-65.8	132.8	**81.2**	-72.7	-71.5	144.2	**74.5**	-70.3	-69.3	139.6	**271.9**	-49.1	-47.1	96.2
N_5	**7.7**	-0.8	-0.2	1.0	**2.7**	-0.6	-0.2	0.8	**-7.2**	-0.5	-0.1	0.6	**-8.4**	-0.3	-0.3	0.5	**15.5**	-1.0	-0.3	1.4
C_6	**-21.7**	-2.0	-0.7	2.8	**-25.4**	-1.9	-0.3	2.2	**-28.6**	-2.0	0.2	1.8	**-25.2**	-2.0	-0.2	2.1	**-7.0**	-2.1	-1.2	3.3
H_7	**100.2**	-4.0	-2.2	6.3	**90.4**	-4.0	-2.4	6.4	**95.9**	-4.5	-3.2	7.7	**77.2**	-4.5	-3.4	7.8	**58.8**	-3.0	-1.4	4.3
H_8	**4.2**	-4.2	-3.8	8.0	**2.0**	-3.9	-3.7	7.6	**2.8**	-4.0	-3.9	7.9	**1.7**	-4.0	-3.6	7.6	**0.8**	-3.4	-2.5	6.0
H_9	**54.5**	-4.3	-4.2	8.5	**69.0**	-4.2	-3.9	8.0	**81.7**	-4.3	-3.4	7.7	**95.7**	-4.1	-3.0	7.1	**23.8**	-3.8	-3.4	7.2
H_{10}	**84.6**	-4.3	-3.8	8.1	**80.7**	-4.3	-3.9	8.2	**4.5**	-5.4	-4.8	10.3	**2.7**	-5.3	-4.5	9.7	**61.3**	-2.9	-2.5	5.4
H_{11}	**5.2**	-5.7	-4.4	10.1	**4.8**	-5.4	-4.2	9.5	**65.9**	-4.5	-4.3	8.8	**65.7**	-4.7	-4.4	9.1	**-1.4**	-4.6	-3.2	7.8
H_{12}	**17.6**	-5.9	-4.7	10.6	**22.3**	-5.4	-4.6	10.0	**72.3**	-5.3	-4.6	9.9	**69.8**	-4.8	-4.3	9.0	**10.4**	-4.4	-3.4	7.8

	BLYP/II/6				BLYP/III/6				BP86/PW			
	A_{iso}	T_{xx}	T_{yy}	T_{zz}	A_{iso}	T_{xx}	T_{yy}	T_{zz}	A_{iso}	T_{xx}	T_{yy}	T_{zz}
O_1	**0.1**	-43.6	15.1	28.5	**-1.2**	-38.6	15.2	23.5	**-1.8**	-45.4	18.6	26.8
C_2	**-35.1**	-10.6	4.2	6.4	**-31.2**	-8.9	3.5	5.4	**-23.8**	-8.6	2.3	6.3
O_3	**-8.7**	-81.8	39.1	42.6	**-4.7**	-58.8	27.8	31.0	**-4.0**	-46.7	21.8	24.9
C_4	**84.7**	-63.0	-62.0	125.0	**99.0**	-68.1	-66.6	134.7	**143.4**	-66.1	-64.3	130.3
N_5	**-2.0**	-0.4	-0.1	0.5	**-1.6**	-0.5	-0.2	0.7	**6.6**	-1.0	-0.2	1.2
C_6	**-24.9**	-1.7	0.3	1.4	**-26.7**	-2.0	0.2	1.8	**-20.9**	-1.8	-0.8	2.6
H_7	**71.6**	-4.0	-2.5	6.5	**84.7**	-4.3	-2.6	6.9	**105.1**	-3.8	-2.2	6.0
H_8	**1.6**	-3.8	-2.7	6.5	**1.4**	-3.9	-3.3	7.1	**9.6**	-3.9	-3.6	7.5
H_9	**74.9**	-3.8	-3.4	7.2	**77.8**	-4.2	-3.7	7.9	**41.0**	-4.2	-4.0	8.2
H_{10}	**74.3**	-4.2	-3.8	8.1	**85.1**	-4.5	-4.1	8.6	**95.2**	-4.4	-3.6	7.9
H_{11}	**4.9**	-4.9	-3.8	8.7	**6.0**	-5.3	-4.1	9.3	**6.7**	-5.4	-3.9	9.3
H_{12}	**26.4**	-4.5	-4.1	8.6	**30.0**	-4.9	-4.4	9.4	**17.0**	-5.6	-4.4	10.0

Table 5.5: Summary of the isotropic and anisotropic components of the hyperfine coupling tensor, calculated for all optimized radical geometries.

The partial sp^3 character of the radical center C_4 in most optimized geometries has a considerable effect on the EPR hyperfine coupling constants of the surrounding atoms. In Figure 5.9 the isotropic hfcc of nitrogen, calculated at the different levels of theory is plotted as a function of the improper torsion angle C_2-N_5-C_6-C_4, which stands for a measure of deviation from planarity of the radical backbone.

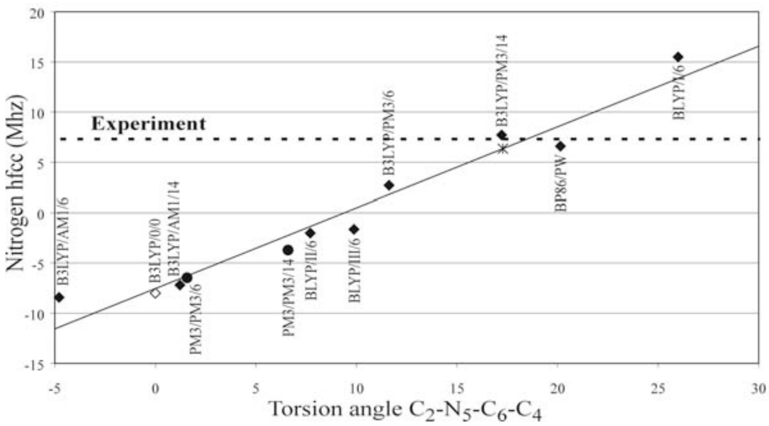

Figure 5.9: The nitrogen isotropic hyperfine coupling constant is plotted as a function of the torsion angle C_2-N_5-C_6-C_4 at different levels of theory. The dotted line represents the experimental value, while the asterisk (*) stands for the B3LYP/I/6 result with a constraint on the improper torsion angle C_2-N_5-C_6-C_4.

The plot clearly indicates that the N hfcc exhibits an almost linear dependence with the non-planarity of the radical backbone: the more the radical backbone deviates from the planar conformation, the larger the N-hfcc prediction becomes. The experimental value of 7.3 MHz [79] is best reproduced by the B3LYP/PM3/14 and the periodic BP86/PW calculations. Only few calculations succeed in reproducing the N-hfcc in a satisfactory way. The B3LYP/AM1/6-14 and PM3/PM3/6 models even underestimate the experimental value by 14 to 15 MHz. The striking correlation between the hfcc of the nitrogen atom and the non-planarity of the radical backbone is confirmed by additional calculations based on models whose ab-initio prediction of the N-hfcc differs significantly from the experimental value but where we constraint the improper torsional angle C_2-N_5-C_6-C_4 to be 17.22°, as resulting from the B3LYP/PM3/14 optimized geometry. Applied to the BLYP/I/6 optimized geometry, we get a new value for the N-hfcc (indicated by the asterisk * in Figure 5.9) close to the experimental estimate and obeying the linear correlation as suggested.

As the methyl group acts as a quasi-free rotor even in a crystalline environment only computed averages of the methyl proton couplings have sense. Their absolute differences between calculated and experimental isotropic coupling constants are displayed in Figure 5.10 for all optimized geometries.

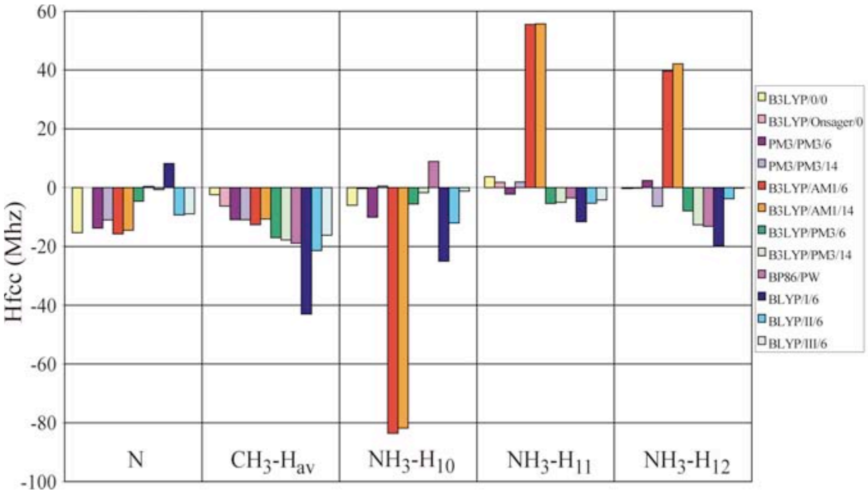

Figure 5.10: Overview of the different hyperfine coupling constants calculated at various levels of theory relative to the experimental values. Note that the B3LYP/Onsager/0 prediction for the N-hfcc has not been reported in ref. [82] and is accordingly not indicated.

A striking feature in this figure is the excellent reproduction of these average hfcc's by the calculations in the absence of any neighbours. All cluster and periodic models predict values which are not of that level of agreement. This is an unlike feature, as this points towards the necessity of a planar radical structure for getting satisfactory reproduction of the methyl proton hfcc's, and is apparently in contrast to preceding conclusions. This stimulated us to study into more details the underlying reasons of this apparent contradiction. Therefore we performed some additional calculations in an attempt to search for the geometrical parameters with the greatest impact on the averaged value of the methyl hydrogen coupling constants. Starting from the B3LYP/PM3/14 optimized geometry the planarity of the radical was gradually increased by reducing the improper torsional angle C_2-N_5-C_6-C_4 to zero, while keeping all other variables at their optimized values. In a subsequent step, the CO_2 group was rotated gradually towards a fully planar conformation of the radical backbone. During these geometry changes, the average methyl proton hfcc values were systematically calculated and reported in Figure 5.11.

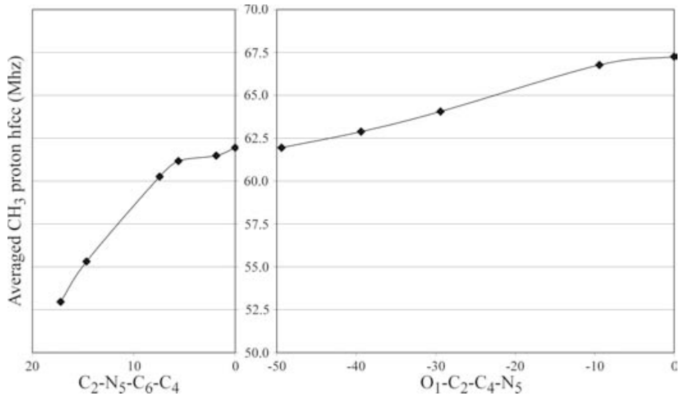

Figure 5.11: The averaged methyl proton hyperfine coupling constants as a function of the planarity of the radical backbone and rotation of the CO_2 group.

In the first part of the figure, the average hfcc is plotted versus the improper torsion angle C_2-N_5-C_6-C_4 reflecting the measure of non-planarity of the radical backbone. This change in geometry induces already an increase of 10 MHz. In the second part of Figure 5.11, the isotropic hfcc is shown with respect to the O_1-C_2-C_4-N_5 torsional angle. This rotation of the CO_2 group towards planarity gives rise to an additional increase of 5 MHz. The remaining discrepancy between the experimental and the average methyl proton hfcc can probably be attributed to the other geometrical parameters that were not optimized. This calculation suggests that the experimental (rotationally averaged) value of the methyl proton hfcc originates from a planar radical structure, as suggested by both experimental and earlier theoretical studies [82, 83]. We believe that this apparent contradiction with earlier conclusions is due to temperature effects on the geometry of the central radical.

The situation is different for the amino protons. Their isotropic hyperfine coupling constants are also displayed in Figure 5.10. The amino protons are involved in intermolecular hydrogen bridges, each proton participating in one hydrogen bond with an oxygen atom from a neighbouring alanine molecule. Due to these interactions, the amino group cannot freely rotate, resulting in three individual hyperfine coupling tensors for the amino protons. Hydrogen bond distances fluctuate around 1.8 Å, except for the B3LYP/AM1/6-14 structures where they are overestimated, in accordance with our earlier observations. Furthermore, the hydrogen bonds cause a rotation of the amino group about the C_4-N_5 axis. This torsional motion is described by the dihedral angle H_{10}-N_5-C_4-C_2. From Table 5.4, it follows that most levels of theory yield comparable values for this dihedral angle. Apart from the B3LYP/AM1/6-14 levels and the BLYP/I/6 level, the torsional angle always varies between 70° and 80°. Our earlier conclusions about the minute basis size in the case of BLYP/I/6 and the inaccurate modeling of hydrogen bonds in the case of B3LYP/AM1/6-14 are thus sustained for radical systems. In earlier studies by Lahorte et al. [83] and Ban et al. [82], a geometry was proposed in which one of the hydrogen atoms of the amino group lies in the plane of the fully planar radical backbone. In order to get good agreement with experimental results, the amino group had to be rotated about the C_4-N_5 axis, as is illustrated in Figure 5.12.

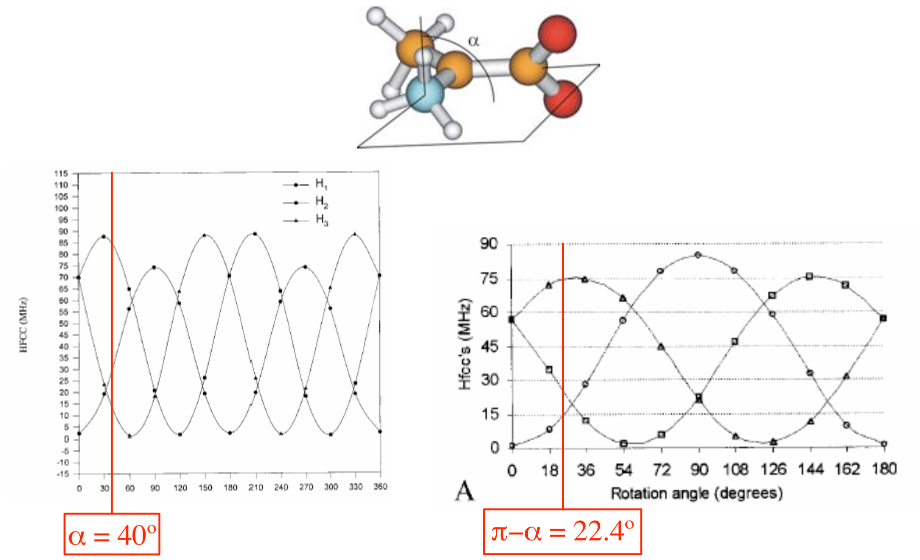

Figure 5.12: For the R2 radical in a single molecule approach, agreement between experiment and theory is only possible when the amino group is rotated about a specific angle α=H_{10}-N_5-C_4-C_2. In the case of [82], α equals about 40° while in [83] π−α was determined at 22.4°. Figures are taken from the respective papers, and in the latter paper a different rotation angle was defined (hence π−α).

Both studies proposed final geometries with H_{10}-N_5-C_4-C_2 dihedral angles that apparently differ substantially from the approximate 80° of our ab-initio results. However, since the amino group rotation of these geometries was altered to fit the experimentally proposed hyperfine coupling constants and considering the symmetry of the plots in Figure 5.12, equally sound agreements between experiment and calculation can be obtained at a rotation angle between 70° and 80°. In contrast, by explicitly accounting for the molecular environment of the central radical this ‘manual’ adjustment of the amino group rotation is no longer necessary.

The overview of the different results and discrepancies with experiment in Figure 5.10 learns that most of the cluster and the periodic calculations succeed in a very satisfactory reproduction of the amino-proton hfcc's. Two calculations emerge from the general pattern: those corresponding to the B3LYP/AM1/6-14 methods. Their optimized geometries are very unrealistic, as already mentioned, and they obviously result into large discrepancies as noticed in the unsound coupling constants of the three amino protons. The PM3/PM3/14, B3LYP/PM3/6-14 and BP86/PW geometries produce a comparable absolute error over all amino proton hfcc's (15 to 25 MHz in total). For the PM3/PM3/6 geometry they are in somewhat better agreement with experiment, although the error is still quite large for proton H_{12}. Figure 5.10 also learns that the size of the basis set has a substantial impact on the accuracy of the results. Among the three BLYP/I-III/6 geometries, the best agreement with experiment is reached by the model corresponding to the most extended basis set. This is probably due to a more reliable reproduction of the hydrogen bridges.

5.5 CONCLUSIONS

The geometries and hyperfine coupling constants of the R2 radical of L-α alanine have been computed using primarily density functional theory in both cluster and periodic models. The calculated results have been compared with the experimental values obtained from X-irradiated crystals of L-α alanine at 295 K. A detailed investigation has been made on the optimized geometries in a variety of model space approaches using different levels of theory and their impact on the various hyperfine coupling constants has been studied. This work can be regarded as an extension of previously done work [82, 83] where the lack of environmental effects was commonly accepted as inadequate for an accurate description and reproduction of quantities that are strongly geometry-dependent. The most dramatic change in the geometry due to the crystal environment on the alanine radical in its zwitterionic form is the deviation of the radical backbone from its planar skeleton. This deviation of planarity is a prerequisite for the satisfactory reproduction of the isotropic hyperfine coupling constants of the nitrogen atom and the amino protons. On the other hand the non-planarity hinders the reproduction of the experimental averaged methyl proton hfcc's. We attribute this discrepancy to temperature effects, since the present static calculations correspond to a situation at zero temperature, while the experimental measurement has taken place at room temperature. Thermal agitation probably weakens the strength of the intermolecular hydrogen bridges, breaking down the forces keeping the central radical R2 in the non-planar conformation. This picture would suggest a tendency to a more planar structure as the average conformation, giving a probable interpretation of the relatively good results obtained from the B3LYP/0/0 and B3LYP/Onsager/0 calculations on isolated molecules. We stress the overall-success of the periodic calculations. They have posed considerably less convergence problems than most of the cluster calculations. The optimized geometries resemble those of the most advanced cluster results and the overall agreement with the experimental hfcc's should be emphasized and is best illustrated in Figure 5.10.

Chapter 6. Radiation-induced radicals in α-glycine

REFERENCE: [100], [101].

6.1 BACKGROUND

Ever since the first EPR analyses of the radiation-induced radicals in solid-state α-glycine – the simplest amino acid – a vast amount of studies have appeared concerning their precise structure, both from an experimental and theoretical point of view.

In the mid 1950's, two groups first observed a triplet in the EPR spectrum of glycine crystals, irradiated with either X-rays [102] or γ-rays [103], and both attributed this signal to a radical of type $R\text{-}^{\bullet}CH_2$. Even so, the existence of a second radical in the glycine lattice was suggested, based on unresolved fine structure in the spectrum. Ghosh and Whiffen [104] suggested this species to be a radical in its zwitterionic form, $^{+}NH_3\text{-}^{\bullet}CH\text{-}CO_2^{-}$ (or R1), and were the first to analyze nitrogen and several proton hyperfine coupling tensors for this radical. This structure – generated by hydrogen abstraction from the central carbon atom of glycine – was later confirmed [105], and eventually all proton hyperfine coupling tensors were determined accurately using the ENDOR technique [106]. The $R\text{-}^{\bullet}CH_2$ radical was subject to some controversy [102, 107], but eventually the $^{\bullet}CH_2COOH$ structure was proposed [108], a deamination product of glycine (labeled R2). Later on, several other – minor or transient – radicals were detected in the irradiated lattice [109, 110]. Glycine radicals have also been reported in liquid phase [111] and even in the gas-phase [112], but only in solution an EPR analysis was performed. In this study, however, we will solely concentrate on the R1 radical $^{+}NH_3\text{-}^{\bullet}CH\text{-}CO_2^{-}$ in solid-state glycine as it is the major paramagnetic species formed at room temperature and because it closely resembles the zwitterionic glycine molecule in the solid state. Based on the work of Ghosh and Whiffen [104], several other EPR analyses were made for this glycine radical. Hedberg and Ehrenberg [113] suggested some corrections for the proton hyperfine tensors, based on a spectral resolution enhancement technique. More recently, Sanderud and Sagstuen [114] made an elaborate study of irradiated glycine crystals, using EPR, ENDOR and ENDOR-induced EPR (EIE). They measured enhanced hyperfine tensors for the discussed radical, but also detected three new paramagnetic species (among which R3 and R5). An overview of four of the proposed structures in that paper is presented in Figure 6.1 and is illustrative of the complexity of the glycine radiation chemistry.

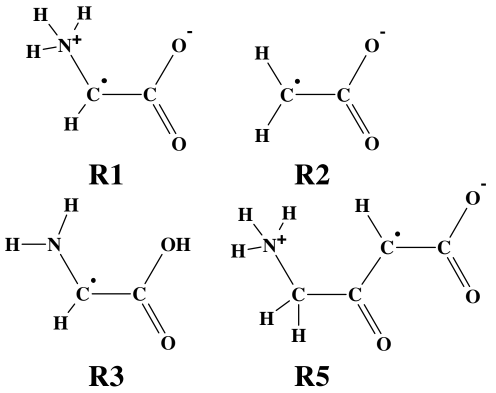

Figure 6.1: Overview of radicals identified in [114].

Prompted by the wealth of experimental results, several theoretical studies have been performed on glycine and its associated radicals [115, 116, 117, 118]. However, for calculated EPR parameters to be in accordance with experiment, a decent radical conformation has to be obtained first and this is somewhat problematic with zwitterionic amino acids. As mentioned earlier, it has been shown that the zwitterionic form of a single glycine molecule in vacuo is not stable and is subject to an intramolecular proton transfer thus adopting a non-ionic form [115]. Similarly, the zwitterionic form of an isolated glycine radical also does not correspond to an energetic minimum [116]. Therefore, in order to study glycine or one of its derived radicals in solid state (or solution), it is essential to account for intermolecular environmental effects in one way or another. Barone et al. addressed this problem by imposing constraints on a single glycine radical during optimization in vacuo [116]. Others have kept the radical in its zwitterionic form by using continuum models [119]. Within this methodology, Ban et al. [117] obtained the isotropic and anisotropic hyperfine couplings for all glycine radicals of Figure 6.1 and compared these with experimental solid-state data. Using a conductor-like variant of the polarisable continuum model (CPCM), Rega et al. [118] calculated the vibrationally averaged isotropic hyperfine coupling constants for comparison with solution EPR couplings.

Despite the evident usefulness of these single molecule calculations, one very important experimental parameter is not analyzed in this approach: the principal axes of the hyperfine interaction tensor. The analysis of this parameter is complicated within a single molecule approach, as it is very tricky to insert the same reference axis system as was done in the experiment. Still, it is possible, using either of the two schemes mentioned in section 4.2.1. Another way to insert the reference frame is to include an explicit part of the surrounding crystal lattice in the calculation, as in cluster models or in a periodic approach.

In this study, therefore, we have modeled the $^{+}NH_3$-$^{\bullet}CH$-CO_2^{-} radical in solid-state glycine, using most of the model space approaches introduced earlier. In a first attempt, the radical defect in glycine is modeled using an adapted single molecule approach. In the second approach, high-level DFT cluster models are employed to obtain a valid conformation of the radical. In the third approach, ab-initio periodic calculations are performed. The results of all these optimizations are then used to calculate the EPR parameters for the different conformations. To also examine the influence of the neighboring lattice on the electronic structure of the central radical, EPR calculations were performed both on the single radical and on the radical in its cluster environment. During the subsequent analysis of the spectroscopic properties, special attention is paid to the reproduction of the calculated principal axes of the hyperfine tensor.

6.2 MODEL SELECTION AND COMPUTATIONAL DETAILS

The α-glycine crystal reveals space group symmetry $P2_1/n$ and has four glycine molecules in the monoclinic unit cell. In what follows, we refer to the atomic lattice coordinates of a recent X-ray diffraction study at 23 K [120] where also the unit cell constants were determined as a=5.087 Å, b=11.773 Å, c=5.460 Å and β=111.99° at the specified temperature.

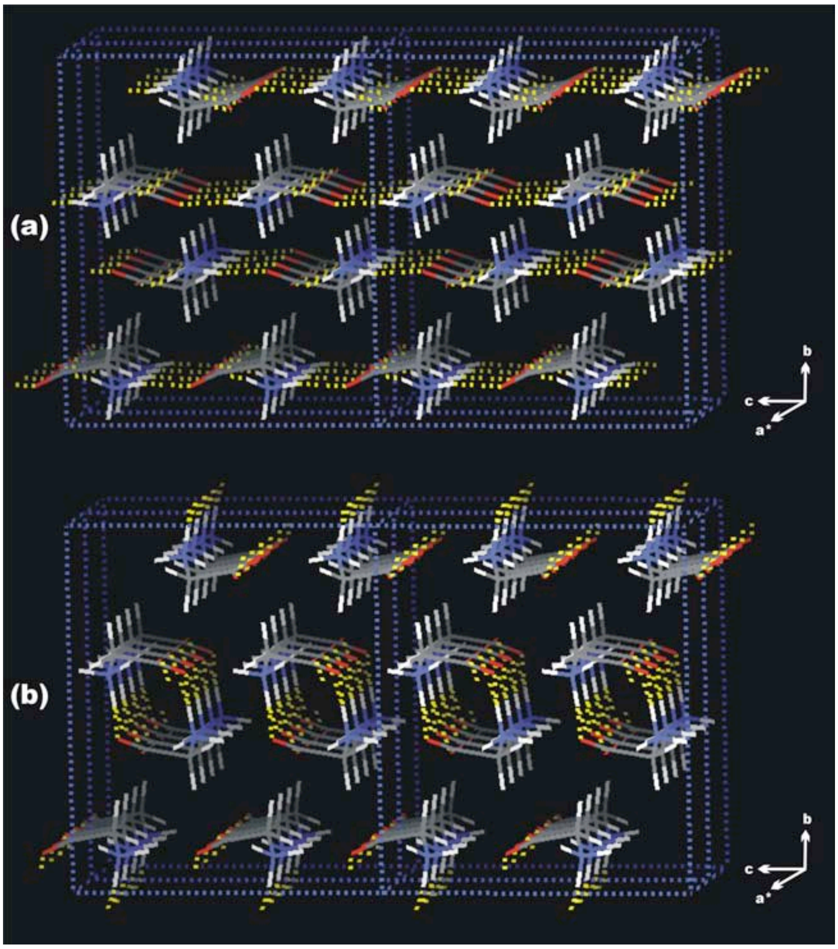

Figure 6.2: Four enlarged unit cells (original unit cell doubled in a- and c-directions), illustrating the hydrogen bonding scheme in solid-state α-glycine. **(a)** Layers of glycine molecules are formed within the crystal by short hydrogen bonds (interactions a and c). **(b)** One long hydrogen bond and a short Van der Waals contact hold together adjacent layers (interactions b and d, respectively).

As is illustrated in Figure 6.2(a), the glycine crystal structure can be best described as consisting of layers, perpendicular to the b axis, which are formed by two short hydrogen bonds (O_4-H^a=H_6-O^a=1.748 Å and O_5-H^c=H_7-O^c=1.821 Å). The atomic numbering is defined in Figure 6.3. Adjacent layers are held together by a slightly weaker hydrogen bond (O_5-H^d=H_8-O^d=2.04 Å) and a short van der Waals contact (O_4-H^b=H_8-O^b=2.387 Å), as shown in Figure 6.2(b). Considering the last interaction to be an extremely weak hydrogen bond, an actual network of bifurcated hydrogen bonds mainly keeps the glycine crystal structure together. These and other representative geometrical features are listed in the left column of Table 6.1.

	Experiment	Optimized crystal geometry			Optimized radical geometry					
		Cluster approach		Periodic approach	Single molecule		Cluster approach			Periodic approach
		B3LYP/PM3/7	B3LYP/7	BP86/PW	B3LYP/1	B3LYP/Onsager/1	B3LYP/PM3/7	B3LYP/PM3/10	B3LYP/7	BP86/PW
Bond lenghts										
C1-C2	1.527	1.515	1.533	1.504	1.468	1.501	1.448	1.440	1.469	1.447
C1-O4	1.257	1.267	1.257	1.278	1.257	1.266	1.267	1.264	1.268	1.291
C1-O5	1.259	1.261	1.259	1.287	1.259	1.270	1.280	1.276	1.265	1.295
C2-N3	1.482	1.537	1.480	1.479	1.505	1.471	1.490	1.484	1.438	1.437
C2-H9	1.080 / 1.090	1.091 / 1.091	1.092 / 1.087	1.095 / 1.090	1.078	1.083	1.081	1.101	1.080	1.086
N3-H6	1.036	1.048	1.045	1.074	1.036	1.034	1.047	1.044	1.049	1.079
N3-H7	1.024	1.058	1.043	1.033	1.024	1.036	1.061	1.065	1.055	1.040
N3-H8	1.024	1.052	1.034	1.060	1.024	1.034	1.064	1.059	1.044	1.087
Dihedral angles										
O4-C1-C2-N3	19.5	29.1	22.2	9.0	19.0	0.0	29.7	24.8	15.2	9.2
O5-C1-C2-N3	-161.3	-149.5	-157.1	-174.5	-161.6	-180.0	-145.0	-150.9	-161.6	-172.1
H6-N3-C2-C1	177.3	177.9	176.0	182.8	177.6	183.7	173.7	171.0	179.2	183.7
H7-N3-C2-C1	-60.6	-57.5	-61.6	-54.9	-59.5	-54.8	-63.0	-63.6	-56.6	-52.6
H8-N3-C2-C1	57.9	55.9	59.0	70.1	57.8	64.8	51.6	49.8	62.3	70.5
Improper torsion angles										
C2-O4-O5-C1	0.6	-1.0	-0.5	2.3	0.4	0.0	-3.0	-2.8	-2.2	0.8
C1-N3-H9-C2	-37.5 / 36.0	-36.5 / 36.1	-36.7 / 35.9	-34.7 / 34.5	2.7	0.0	11.3	-7.7	7.0	0.4
Hydrogen bonding distances										
O4-Ha	1.748	1.730	1.738	1.839	-	-	1.713	1.758	1.728	1.837
O4-Hb	2.387	2.327	2.368	2.215	-	-	2.320	2.253	2.364	2.184
O5-Hc	1.821	1.760	1.733	2.002	-	-	1.759	1.748	1.727	2.005
O5-Hd	2.040	1.833	1.925	1.910	-	-	1.834	1.763	1.969	1.976
H6-Oa	1.748	1.747	1.706	1.615	-	-	1.741	1.738	1.699	1.590
H7-Oc	1.821	1.813	1.792	1.615	-	-	1.812	1.748	1.764	1.528
H8-Od	2.040	1.833	1.962	1.739	-	-	1.819	1.858	1.994	1.628
H8-Ob	2.387	2.439	2.283	2.721	-	-	2.402	2.297	2.177	2.720

Table 6.1: Overview of selected geometrical features for optimized crystal and radical geometries, in comparison with experimental crystal structure data, taken from [120]. Units of bond lengths are Angstroms. The atomic numbering scheme refers to that presented in Figure 6.3. The B3LYP/Onsager/1 geometry is taken from Ban et al. in [117].

Based on the crystal geometry, three different model space approaches were put together to describe the glycine radical within the crystal lattice, each with increasing complexity. In all models, (partial) geometry optimizations were only performed on the central radical. For the calculations incorporating explicit crystal lattice molecules (cluster and periodic approaches), the atomic coordinates of these were fixed in space at the experimental geometry.

6.2.1 Single molecule approach

An initial geometry for the radical was obtained by removing a -CH_2- hydrogen from the original glycine crystal structure as to obtain a $^+NH_3$-$^\bullet$CH-CO_2^- structure. Geometry optimization calculations were then performed within a “**Partial Optimization**” computational regime, outlined in detail in section 4.2.1. Applied to glycine, this scheme essentially implies that only the C_2 and H_9 atoms were allowed to relax, while all other atoms were kept fixed at their original position in the crystal structure during optimization. To allow for the determination of the hyperfine tensor principal directions later on, the partial geometry optimizations were performed using the “Fixed Axes” approximation (see also section 4.2.1) with the Gaussian03 software package [31]. This keyword constrains the software package not to shift or rotate the Cartesian coordinates of the radical model with respect to the reference frame and so a direct link with the original crystal axes is preserved.

The calculations were performed within a Density DFT framework, employing the B3LYP functional [28]. Molecular orbitals were expanded in a triple-ζ 6-311G** basis augmented with single d and p polarisation functions [33]. In what follows, we will refer to the results of these calculations with the B3LYP/1 shorthand.

6.2.2 Cluster approach

A cluster model of glycine molecules was constructed in accordance with the structure of the α-glycine crystal as determined from X-ray diffraction [120]. In this lattice, an initial cluster was obtained by considering all molecules that are engaged in hydrogen bonds with a central glycine molecule. This way, a model space of 7 molecules was constructed, involving all hydrogen bonding interactions taking place between one glycine and its crystalline environment. Again a starting geometry for the radical $^+NH_3$-$^\bullet$CH-CO_2^- was obtained by abstracting one -CH_2- hydrogen atom from the central glycine molecule. This model is shown in Figure 6.3.

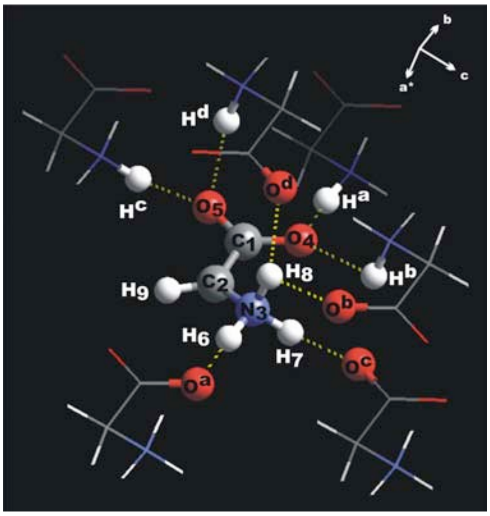

Figure 6.3: B3LYP/PM3/7 optimized geometry for the glycine radical, illustrating the model space in the cluster approach. Yellow dashed lines give an enhanced view of the hydrogen bonds presented in Figure 6.2.

The radical structure was then fully optimized within the cluster in search for conformations with minimal energy. Initially, a layered ONIOM approach of the system was adopted, since it proved quite successful and cost-effective in the analogous study on the radiation products of L-α-alanine. In this ONIOM scheme, the central radical makes up the 'inner' layer and is treated at a high level of theory (DFT-B3LYP [28] with 6-311G** basis set [33]) while the surrounding glycine molecules – the 'outer' layer – are described using a semi-empirical PM3 Hamiltonian [36]. The optimized glycine conformation thus obtained will be referred to with the abbreviation B3LYP/PM3/7.

Subsequently, a second, larger cluster was also considered within this methodology, obtained by extending the original cluster of six with four additional lattice molecules, all having at least one atom closer than 4.0 Å from the center of mass of the central glycine radical. The resulting model space – thus consisting of one radical and nine surrounding molecules – was also subjected to the ONIOM optimization mentioned above, and the resulting conformation is referred to as B3LYP/PM3/10.

Additional calculations were performed on the small cluster, treating both glycine radical and lattice molecules at a full ab-initio B3LYP level, with a 6-311G** basis. The results of these quite exhaustive calculations will be labeled B3LYP/7. No calculations were performed on the large cluster at this level, as it would impose severe stress on computational resources.

To assess the accuracy and validity of the ONIOM and full ab-initio levels of theory to describe the intermolecular interactions within the crystal, complementary calculations were performed on a small cluster of 7 undamaged glycine molecules. Analogous to the L-α-alanine study, the optimization procedure presented above for the B3LYP/PM3/7 and B3LYP/7 approaches was reapplied on an intact central glycine molecule. The resulting geometrical parameters (which are given in the left side of Table 6.1) allow for a direct comparison with the experimentally determined conformation in the crystal lattice.

6.2.3 Periodic approach

To properly simulate the radical in the crystal lattice within a periodic approach, it is necessary to double the unit cell in the a- and c directions to ensure that the radical defects are well separated from each other. The resulting orthorhombic supercell contains 15 glycine molecules and the central radical. The structure of the radical was optimized by using a simulated annealing technique as proposed by Car and Parrinello [70]. In this scheme, the interatomic forces are calculated on the "fly" from the instantaneous electronic potential. For glycine, the global minima of the radicals at T=0K were localized by simultaneously optimizing the electronic and nuclear degrees of freedom. For the geometry optimizations the structure of the radical was allowed to relax, while the coordinates of all other atoms were kept fixed at their experimental geometries. All periodic calculations were performed with the CPMD molecular dynamics program [69]. Very soft pseudopotentials of the Vanderbilt type were used to account for the core, with use of an energy cutoff of 25 Ry (1Ry=1314 kJ/mol) for the plane wave expansion [97]. The electronic structure is described within the DFT formalism with use of the BP86 gradient corrected functional [23, 24, 25].

Similarly as for the cluster approach we also adopted the periodic model on the undamaged glycine crystal lattice in which a central molecule was allowed to relax and its neighbors were kept fixed at their experimental positions. The resulting geometrical parameters are also given in Table 6.1 and a comparative study of the experimental and theoretical geometry enables us to assess the accuracy of these type of calculations.

6.2.4 EPR calculations

The Gaussian03 software package [31] was used to calculate isotropic and anisotropic hyperfine couplings, as well as the associated principal axes. This was done using a B3LYP functional [28] within the DFT framework and employing a 6-311G** basis set [33].

For cluster or periodic lattice models, the EPR parameters were initially determined solely on the optimized structure of the central radical, without taking into account the neighbors. Hence, these are effectively single molecule EPR calculations. To evaluate the influence of neighboring lattice molecules on the EPR parameters of the central radical and thus on its electronic structure, the paramagnetic properties were also calculated for the full cluster. The results of these calculations will be referred to with the additional label "(full)", as the complete model space was accounted for in the EPR calculation. Similar calculations within a periodic approach were, however, impossible as these are not yet implemented in the CPMD code.

6.3 GEOMETRICAL ANALYSIS

6.3.1 Radical geometry in single molecule approach

Considering the main conformational properties of the B3LYP/1 optimized radical geometry in the right side of Table 6.1, it is quite obvious that large similarities appear with the crystal geometry, apart from the planarity of the radical backbone – expressed by the C_1-N_3-H_9-C_2 improper torsional angle, that is a direct measure of the deviation from planarity for the C_2 carbon radical center. For completeness, we have also included in Table 6.1 geometrical information on the conformation proposed by Ban et al. [117]. This structure was also obtained at the DFT level of theory, using a B3LYP functional and a double-ζ 6-31+G** basis, within the Onsager solvent simulation approach [119]. The structure – hence labelled B3LYP/Onsager/1 – is quite similar to our single molecule geometry, although a substantial deviation from the crystal structure is evident for the CO_2-group. Both the O_4-C_1-C_2-N_3 and O_5-C_1-C_2-N_3 torsional angles indicate a rotation of about 20°. These geometrical features can not be reproduced in our single molecule approach since only C_2 and H_9 are allowed to relax.

6.3.2 Model assessment for cluster and periodic approach

As mentioned, separate geometry optimization calculations were performed on an undamaged glycine molecule adopting both cluster and periodic approaches. By consecutively evaluating the difference between these optimized crystal geometries and the original crystal structure, an assessment was possible of the capabilities of either model approach to treat intermolecular interactions within solid-state glycine. The resulting geometrical features of the optimized crystal geometries are given in the left side of Table 6.1.

Bond lengths are most accurately reproduced at the B3LYP/7 level of theory. The largest deviation is found for the N_3-H_7 bond and is limited to 0.02 Å. In contrast, substantially larger deviations are reported when part of the cluster is treated at the semi-empirical level: the B3LYP/PM3/7 optimized central glycine molecule displays particularly elongated N_3-H_7, N_3-H_8 and C_2-N_3 bonds that are up to 0.05 Å longer.

Surprisingly, apart from C_2-N_3 and N_3-H_7, all predicted bond lengths at the BP86/PW level of theory deviate with about 0.03 Å from the crystal structure.

A similar qualitative pattern can be observed for the dihedral angles. Those of the B3LYP/7 optimized central glycine are in remarkable correspondence with the crystal, while those of the B3LYP/PM3/7 geometry show that the CO_2 group is rotated some 10° counter-clockwise about the C_1-C_2 bond. At the BP86/PW level, this rotation is instead reversed to about -10° and also the position of the NH_3 group is altered, the H_8-N_3-C_2-C_1 dihedral angle exhibiting the largest change (12°).

Hydrogen bond distances are perhaps the most sensitive and powerful indicators of the model approach performance to describe intermolecular interactions. These distances, both from experiment and theory, are plotted in figure 6.4, subdivided by the four types of hydrogen bond interactions occurring in the crystal. Both cluster methods accurately reproduce the two short interactions a and c, which are the strongest hydrogen bonds. In the periodic approach, on the other hand, their strength is significantly overestimated at the side of the amino protons H_6 and H_7, while it is instead underestimated at the O_4 and O_5 side. This tightening of the hydrogen bond at one end and an elongation at the other consequently shifts the whole glycine molecule in the direction of the O^a and O^c matrix atoms. Neither cluster nor periodic approach succeeds in a very accurate prediction of the long hydrogen bond distance (interaction d). The B3LYP/7 method is closest, with roughly a 0.1 Å deviation for both H_8-O^d and O_5-H^d. In the BP86/PW optimized geometry, the strength of the hydrogen bond is again overestimated at the side of the amino proton, with a dramatic 0.3 Å shortening of the H_8-O^d distance. In the case of a periodic approach, clearly the hydrogen bond network of glycine is completely disturbed, which is corroborated even further by the erroneously predicted H_8-O^b and O_4-H^b distances. Nevertheless, the latter short van der Waals contact (interaction b) is treated quite properly at the B3LYP/PM3/7 or B3LYP/7 level of theory.

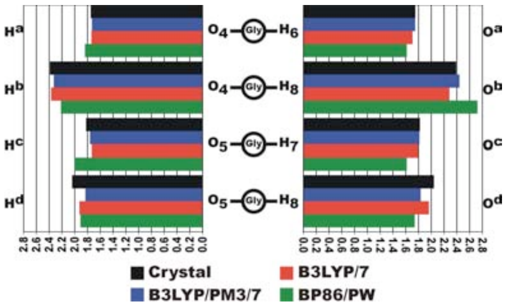

Figure 6.4: Schematic representation of hydrogen bond distances (in Å) between an optimized glycine molecule and the simulated crystal matrix. The four types of hydrogen bond interactions are considered separately.

From this initial assessment it is clear that cluster methods are likely to provide the best description of intermolecular forces within the glycine solid state. Among these methods, a full ab-initio (B3LYP/7) model is preferable. Despite their only limited level of theory, hybrid cluster models (B3LYP/PM3/7) offer an overall better description of this crystal than a periodic approach. The latter method is computationally quite expensive and predicts too large deviations for the hydrogen bonds while the internal structure of the glycine molecule is fairly accurate. However, it first has to be established that these results also apply to the interaction between a (central) glycine radical and a simulated crystal lattice.

The failure of the periodic method to describe the weak forces must probably be assigned to the use of the gradient corrected functional BP86. However, the results as given do not allow a systematic rejection of periodic approaches, but stress the importance of the use of a correct functional for the right application. Most periodic packages do not include yet the use of hybrid functionals, but improvement can be expected in the near future which will allow us then to reassess the accuracy of the periodic calculations with more advanced functionals [121].

6.3.3 Radical geometry in Cluster Approach

Nearly identical bond lengths and dihedral angles can be observed for both ONIOM optimized structures (indicated as B3LYP/PM3/7 and B3LYP/PM3/10). The hydrogen bond lengths in both geometries are also comparable to those of the crystal, the O_5-H^d and H_8-O^d distances notwithstanding. Apparently, the effects observed in the initial assessment on the optimized crystal geometry do also apply here.

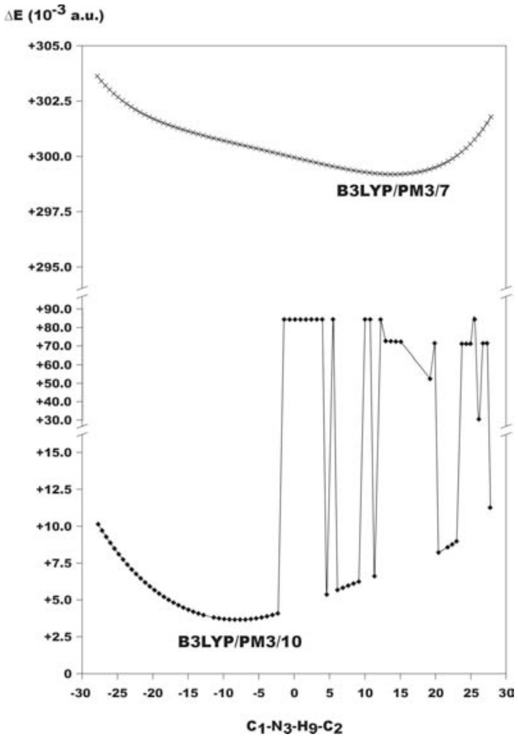

Figure 6.5: ONIOM extrapolated energies (in 10^{-3} a.u.) of B3LYP/PM3/7 (x) and B3LYP/PM3/10 (♦) clusters, as a function of a scan for the C_1-N_3-H_9-C_2 dihedral angle. Energies are reported relative to a base level of -284.83 a.u.

Only one feature is clearly differing in both ONIOM approaches: the C_1-N_3-H_9-C_2 dihedral angle, describing the planarity of the radical backbone, switches from +11.3° in the B3LYP/PM3/7 structure to –7.7° for B3LYP/PM3/10. This apparent incoherency as a result of cluster size expansion prompted us to investigate the effect of the radical planarity on the total cluster energy. In Figure 6.5 the total ONIOM extrapolated energies of both small (×) and large (♦) clusters are plotted as a function of the C_1-N_3-H_9-C_2 dihedral (relative to a base level of –284.83 a.u.). In the upper and lower parts of the graph distinct energetic minima are visible, roughly corresponding to the representative planarity values for the optimized B3LYP/PM3/7 and B3LYP/PM3/10 geometries, respectively. However, for the latter cluster, inconsistent energies are obtained for some specific C_1-N_3-H_9-C_2 values. This discontinuity in the groundstate energy behaviour is obviously unphysical and needs special attention. We observe that in these specific unphysical cases, something wrong happens with the electronic PM3 wave function. An investigation of the spin density learns that a redistribution of the spin has taken place over different molecules in the cluster. Summing up all atomic spin densities per molecule, two molecules contribute to the total unpaired spin density (ρ_α - ρ_β) with about $+\frac{1}{2}$ and $-\frac{1}{2}$, respectively, in addition to the $+\frac{1}{2}$ of the central radical. Although the net unpaired spin density of the complete cluster ($\frac{1}{2}$ in total) is still maintained in this scheme, a completely unphysical electronic configuration is thus obtained. Similar unphysical solutions with the PM3 method – besides convergence difficulties – were encountered in a preliminary study (taken up in [101]) on even larger glycine clusters – including up to 18 molecules – and have also been recognized in a study of the cation radicals in L-α-alanine [50]. Based on these indications of numerical instability with increasing cluster size and of the geometrical discrepancies with the B3LYP/PM3/7 structure, we decided to reject the B3LYP/PM3/10 optimized geometry altogether.

Comparing the full-B3LYP optimized geometry B3LYP/7 with the B3LYP/PM3/7 structure, several subtle, but striking differences can be noticed. Apart from an enhanced radical planarity (7.0° instead of 11.3° for C_1-N_3-H_9-C_2), the overall rotation of the amino group is altered as well. Whereas in the B3LYP/PM3/7 structure, this group is rotated 4° about the N_3-C_2 bond in a clockwise direction with respect to the original crystal structure, in the B3LYP/7 structure it is rotated 4° in a counter-clockwise direction. A similar observation can be made for the CO_2 group rotation, which is now virtually parallel with its original orientation in the crystal for B3LYP/7. These effects are most likely correlated with a more correct description within DFT of the O_5-H^d and H_8-O^d weak hydrogen bonds between radical and lattice, as observed in the previous section. In fact, all geometrical features of the glycine radical and the optimized crystal are comparable, apart from the C_2-H_9 distance and the C_1-N_3-H_9-C_2 improper torsion angle, evidently.

6.3.4 Radical geometry in Periodic Approach

The same observation can be made at the BP86/PW level of theory, where the structural parameters of the radical now closely resemble those of the optimized crystal geometry. In contrast with the cluster models, the radical backbone is nearly planar (almost 0° for C_1-N_3-H_9-C_2). The shortening and lengthening effects on the hydrogen bonds (see model assessment section) are even more pronounced for the radical geometry. Most remarkably, the H_6-O^a, H_7-O^c and H_8-O^d hydrogen bonds at the side of the amino group are lowered below 1.6 Å.

6.4 EPR PARAMETERS

In this section, we will compare the different experimental EPR results with calculated EPR parameters for all optimized geometries, as summarized in Table 6.2. Here, all hyperfine couplings are presented in MHz and the principal axes of the tensors are always given by means of direction cosines with respect to the orthogonal reference frame <oa*bc>.

For reference, we have also summarised the calculated EPR parameters, obtained in earlier theoretical (single molecule) studies. The UQCISD/1, B3LYP/CPCM/1 and B3LYP/Onsager/1 labels thus refer to the results of Barone et al. [116], Rega et al. [118] and Ban et al. [117], respectively.

	Experimental data																								
	Ghosh & Whiffen (1959)					Morton (1964)					Collins & Whiffen (1966)					Hedberg & Ehrenberg (1968)					Sanderud & Sagstuen (1998)				
	Aiso	Taniso	Principal axes			Aiso	Taniso	Principal axes			Aiso	Taniso	Principal axes			Aiso	Taniso	Principal axes			Aiso	Taniso	Principal axes		
C_{exp}						126.7	-90.0	0.902	-0.080	-0.424															
							-36.7	0.360	-0.404	0.841															
							126.8	0.239	0.911	0.335															
N_{exp}	-8.6	3.4	-0.650	0.760	0.000						-9.0	1.9	-0.394	0.916	-0.076	-8.7	1.7	-0.217	0.951	0.219					
		-1.5	0.000	0.000	1.000							-0.9					-0.8	0.885	0.097	0.456					
		-2.0	-0.760	-0.650	0.000							-1.1					-1.0	-0.412	-0.293	0.863					
$H_{exp}(\beta1)$											3.3	-7.3	0.620	-0.680	0.391										
												-1.8	0.614	0.731	0.296										
												9.2	-0.488	0.057	0.871										
$H_{exp}(\beta2)$											62.0	-6.0	0.005	-0.810	0.587						62.0	-6.4	-0.077	-0.976	0.206
												-3.2	0.146	0.581	0.801							-3.8	0.031	0.204	0.978
												9.3	0.989	-0.082	-0.121							10.2	0.997	-0.081	-0.015
$H_{exp}(\beta3)$											82.0	-6.1	0.751	0.361	0.551						83.1	-7.1	0.725	0.387	0.570
												-4.0	-0.371	-0.460	0.807							-3.5	-0.386	-0.457	0.801
												10.1	0.545	-0.811	-0.212							10.6	0.570	-0.801	-0.182
$H_{exp}(\alpha)$	-66.0	34.3	0.680	-0.630	0.370						-66.3	27.3	0.789	-0.316	0.527	-63.5	30.4	0.778	-0.378	0.502	-63.7	31.9	0.797	-0.301	0.524
		-4.4	0.430	0.750	0.500							4.9	0.358	0.933	0.023		2.2	0.412	0.910	0.047		1.9	0.330	0.943	0.040
		-29.9	-0.600	0.180	0.780							-32.3	-0.499	0.171	0.850		-32.6	-0.475	0.170	0.864		-33.8	-0.507	0.141	0.851

	Earlier theoretical studies			
	UQCISD/1	B3LYP/CPCM/1	B3LYP/Onsager/1	
	Aiso	Aiso	Aiso	Taniso
C_{exp}	127.8	120.5	98.7	-76.3
				-74.6
				150.9
N_{exp}	-12.3	-9.0	-7.0	-0.4
				0.2
				0.2
$H_{exp}(\beta1)$	-	-	2.3	-5.4
				-4.7
				10.1
$H_{exp}(\beta2)$	-	-	77.1	-5.5
				-4.5
				10.0
$H_{exp}(\beta3)$	-	-	77.1	-5.5
				-4.5
				10.0
$H_{exp}(\alpha)$	-72.3	-62.2	-59.0	-36.1
				-1.5
				37.5

	Calculated data																			
	B3LYP/1					B3LYP/PM3/7					B3LYP/PM3/7 (full)					B3LYP/7				
	Aiso	Taniso	Principal axes			Aiso	Taniso	Principal axes			Aiso	Taniso	Principal axes			Aiso	Taniso	Principal axes		
C_2	77.3	-70.9	0.868	-0.368	-0.335	64.6	-63.5	0.677	-0.490	-0.549	89.7	-74.2	0.592	-0.392	-0.705	72.4	-70.3	0.713	-0.357	-0.603
		-69.9	0.191	-0.376	0.907		-62.7	0.434	-0.336	0.836		-73.7	0.539	-0.457	0.707		-68.8	0.551	-0.246	0.797
		140.8	0.459	0.851	0.256		126.2	0.594	0.804	0.015		147.9	0.599	0.798	0.059		139.1	0.433	0.901	-0.022
N_3	-7.1	-0.5	0.266	-0.276	0.924	-8.3	-0.4	0.657	-0.366	0.659	-6.2	-1.6	-0.767	0.637	0.076	-10.2	-0.6	0.599	-0.154	0.786
		0.1	0.580	-0.719	-0.382		0.1	0.535	0.843	-0.065		-1.2	0.059	-0.048	0.997		-0.1	0.386	0.915	-0.115
		0.4	0.770	0.638	-0.031		0.3	-0.532	0.395	0.749		2.9	0.639	0.769	-0.001		0.6	-0.701	0.372	0.608
H_6	2.2	-5.3	0.370	-0.540	0.756	3.5	-4.7	0.583	-0.588	0.561	0.9	-5.1	0.532	-0.710	0.462	6.6	-5.2	0.691	-0.440	0.574
		-3.8	0.489	0.805	0.336		-3.4	0.674	0.735	0.071		-4.1	0.766	0.636	0.096		-3.8	0.499	0.864	0.062
		9.0	-0.790	0.245	0.562		8.1	-0.454	0.337	0.825		9.2	-0.362	0.303	0.881		9.0	-0.523	0.244	0.817
H_7	57.3	-4.9	-0.274	-0.936	0.223	53.1	-4.7	-0.462	-0.764	-0.452	54.3	-7.2	-0.234	-0.858	0.457	65.0	-4.8	-0.138	-0.936	0.323
		-4.4	-0.057	0.247	0.967		-4.2	0.026	-0.520	0.854		-3.6	0.216	0.413	0.885		-4.5	0.269	0.278	0.922
		9.3	0.960	-0.252	0.121		8.9	0.887	-0.382	-0.260		10.8	0.948	-0.306	-0.088		9.3	0.953	-0.214	-0.213
H_8	59.6	-6.1	0.218	0.159	0.963	66.3	-5.0	0.667	0.119	0.735	70.7	-7.0	0.772	0.194	0.605	92.7	-5.9	0.539	0.105	0.835
		-4.2	-0.729	-0.630	0.269		-3.7	-0.573	-0.549	0.609		-3.7	-0.528	-0.333	0.781		-3.9	-0.580	-0.673	0.459
		10.3	0.649	-0.760	-0.021		8.7	0.476	-0.827	-0.299		10.7	0.353	-0.923	-0.154		9.8	0.610	-0.732	-0.302
H_9	-56.4	-33.9	-0.777	0.217	0.592	-42.0	-29.7	-0.456	0.290	0.842	-50.2	-35.8	-0.481	0.287	0.828	-53.7	-33.1	-0.492	0.226	0.841
		-2.2	0.471	0.824	0.316		-2.9	0.603	0.796	0.053		-3.4	0.568	0.822	0.045		-2.5	0.442	0.897	0.017
		36.1	0.419	-0.524	0.742		32.6	0.655	-0.532	0.537		39.2	0.668	-0.493	0.558		35.6	0.750	-0.380	0.541

	Calculated data														
	B3LYP/7 (full)					BP86/PW					BLYP/PW				
	Aiso	Taniso	Principal axes			Aiso	Taniso	Principal axes			Aiso	Taniso	Principal axes		
C_2	77.8	-74.8	0.737	-0.352	-0.577	65.5	-64.8	0.785	-0.125	-0.607	72.4	-68.7	0.777	-0.093	-0.623
		-73.4	0.512	-0.266	0.817		-63.3	0.600	-0.089	0.795		-67.1	0.618	-0.078	0.783
		148.2	0.441	0.897	0.015		128.1	0.153	0.988	-0.005		135.8	0.122	0.993	0.003
N_3	-7.4	-1.4	0.592	-0.322	0.739	-11.3	-0.5	0.134	-0.953	0.271	-10.8	-0.4	0.327	-0.797	0.509
		-1.0	0.640	-0.370	-0.673		-0.3	0.568	0.298	0.767		-0.3	0.406	0.604	0.686
		2.4	0.490	0.872	-0.013		0.9	-0.812	0.052	0.581		0.7	-0.854	-0.018	0.521
H_6	2.4	-5.1	0.615	-0.639	0.462	7.7	-4.9	0.818	-0.189	0.543	7.2	-5.3	0.807	-0.129	0.576
		-4.3	0.667	0.734	0.128		-3.5	0.174	0.982	0.080		-3.7	0.115	0.991	0.060
		9.4	-0.421	0.229	0.878		8.5	-0.548	0.029	0.836		9.0	-0.579	0.018	0.815
H_7	56.7	-7.1	-0.092	-0.901	0.423	65.8	-4.0	0.089	-0.995	-0.039	62.4	-4.3	0.242	-0.749	0.617
		-3.8	0.097	0.415	0.905		-3.8	0.301	-0.011	0.954		-4.0	0.091	0.650	0.754
		10.8	0.991	-0.124	-0.049		7.8	0.950	0.096	-0.298		8.4	0.966	0.126	-0.225
H_8	93.6	-7.3	0.678	0.237	0.696	99.8	-4.6	0.473	0.140	0.870	99.7	-4.9	0.431	0.130	0.893
		-4.0	-0.545	-0.473	0.692		-3.7	-0.345	-0.879	0.329		-3.9	-0.348	-0.889	0.297
		11.3	0.493	-0.848	-0.191		8.3	0.811	-0.456	-0.367		8.8	0.832	-0.439	-0.338
H_9	-57.2	-36.0	-0.517	0.232	0.824	-51.5	-29.4	-0.517	0.051	0.855	-55.1	-31.5	-0.547	0.041	0.836
		-3.0	0.426	0.905	0.013		-2.9	0.192	0.980	0.057		-2.7	0.138	0.989	0.043
		39.1	0.743	-0.358	0.566		32.4	0.834	-0.194	0.516		34.2	0.826	-0.139	0.547

Table 6.2: Calculated EPR parameters for all optimized radical geometries. A summary is also presented of relevant EPR parameters reported in earlier experimental (references [104], [105], [106], [113], [114]) and theoretical studies (respectively [116], [118], [117]).

6.4.1 Comments on the experimental results

Concerning the overview of past experimental work, several points have to be addressed first:

(i) Although most experimental studies reported temperature-averaged proton tensors for the ammonium group [104, 106, 110, 113 and 114], these are not analysed nor taken up in the table.

(ii) The couplings, determined by Ghosh & Whiffen [104], are reduced by 12% as suggested in a later communication, to correct a field calibration error [122]. Furthermore, the a- and c-axes of the crystal in the original work were later found to be misidentified [105] and the direction cosines have been adjusted accordingly in the table.

(iii) In the work of Hedberg & Ehrenberg [113], the positions of the hyperfine principal axes were reported with respect to the <oabc*> orthogonal reference frame. To allow for comparison, the direction cosines were recalculated with respect to the <oa*bc> frame.

(iv) In a preliminary study of the direction cosines, an incongruence was found for the $H_{exp}(\beta 2)$ and $H_{exp}(\beta 3)$ principal axes between the Collins & Whiffen paper [106] and that of Sanderud & Sagstuen [114]. This was due to a typographical error [123] and the anisotropic hyperfine couplings and the direction cosines for the proton signals were accordingly adjusted. Only the corrected values and cosines are listed in the table.

(v) As the directions of principal axes cannot be determined absolutely, several sign reversals have been made for the direction cosines to improve congruence between the different experimental data. Furthermore, all corresponding tensors are reported for the same crystal site, whenever possible. There are four molecules per unit cell in glycine, but due to its monoclinic nature there are two magnetically different classes of crystal sites. The tensors can be distinguished by reversal of the sign of the direction cosine with the b axis.

The collected experimental data thus identify six hyperfine coupling tensors for the $^{+}NH_3\text{-}^{\bullet}CH\text{-}CO_2^{-}$ glycine radical: one carbon-, one nitrogen- and four proton tensors. However, as there is a vast amount of experimental data available, we prefer to make first a comparative study of them, facilitating the further analysis and comparison with the theoretical predictions.

Since only one measurement exists of the ^{13}C hyperfine tensor (performed by Morton), all calculated EPR results for C_2 in the model radical are compared with respect to this C_{exp} signal.

One of the protons in the radical exhibits α-coupling characteristics. The different experiments are in good agreement with each other for this $H_{exp}(\alpha)$ tensor, except for the results of Ghosh & Whiffen [104], where the anisotropic components and especially the direction cosines diverge substantially. As this experimental work is quite old (1959) and considering the fact that several errors were identified (cf. supra), its results can be considered as outdated by the more recent studies. The eigenvectors of the other studies never deviate more than 5° and we will therefore retain the most recent study by Sanderud & Sagstuen to compare with the computational results of proton H_9 in the radical model.

A similar conclusion can be formulated for the experiments pertaining the nitrogen hyperfine tensor N_{exp}. The results of Collins & Whiffen and those of Hedberg & Ehrenberg are in fair accordance with each other, in particular for the anisotropic principal values since information of two principal axes is missing in the former study. The anisotropic data recorded by Ghosh & Whiffen is not kept for further consideration as they completely differ from the two former experimental works. We retain the work of Hedberg & Ehrenberg as this is the most recent and complete study of the nitrogen hyperfine tensor.

Merely two studies report on the β-coupling protons in the glycine radical species. Only the 1966 paper by Collins & Whiffen accounted for all three β-proton tensors, but its $H_{exp}(\beta 2)$ signal differs substantially from the one reported by Sanderud & Sagstuen [123], even though no quantitative analysis was made for $H_{exp}(\beta 1)$ in this last study. In order to present the analysis of the theoretical EPR parameters without any bias, we have therefore preferred to compare the calculated parameters of amino group protons H_6 through H_8 with the results of both experimental studies.

6.4.2 Analysis of the predicted EPR parameters

All relevant EPR data are displayed in Figure 6.6. The red bars at the top of each plot represent the absolute differences (in MHz) between the experimental hyperfine coupling constants and the calculated values for the optimized geometries, obtained at various levels of theory. The deviation (in degrees) of the three calculated hyperfine principal directions with the three corresponding experimental directions is schematically presented as black bars at the bottom of each plot. In order to systematically retain or reject a theoretical procedure for the reproduction of EPR data, i.e. both hyperfine couplings and tensor axes, we introduced two criteria to which accepted methods must fulfil. For the isotropic couplings, a maximum deviation of 10 MHz is accepted (**criterion I**), while a deviation of 20° at maximum is assumed to be acceptable for the tensor axes (**criterion II**). These thresholds are indicated in Figure 6.6 by horizontal lines. A model approach that violates either of these criteria must be considered as unable to reproduce the experimental data in a satisfactory way. As a result, they have been assessed in function of criterion I and II.

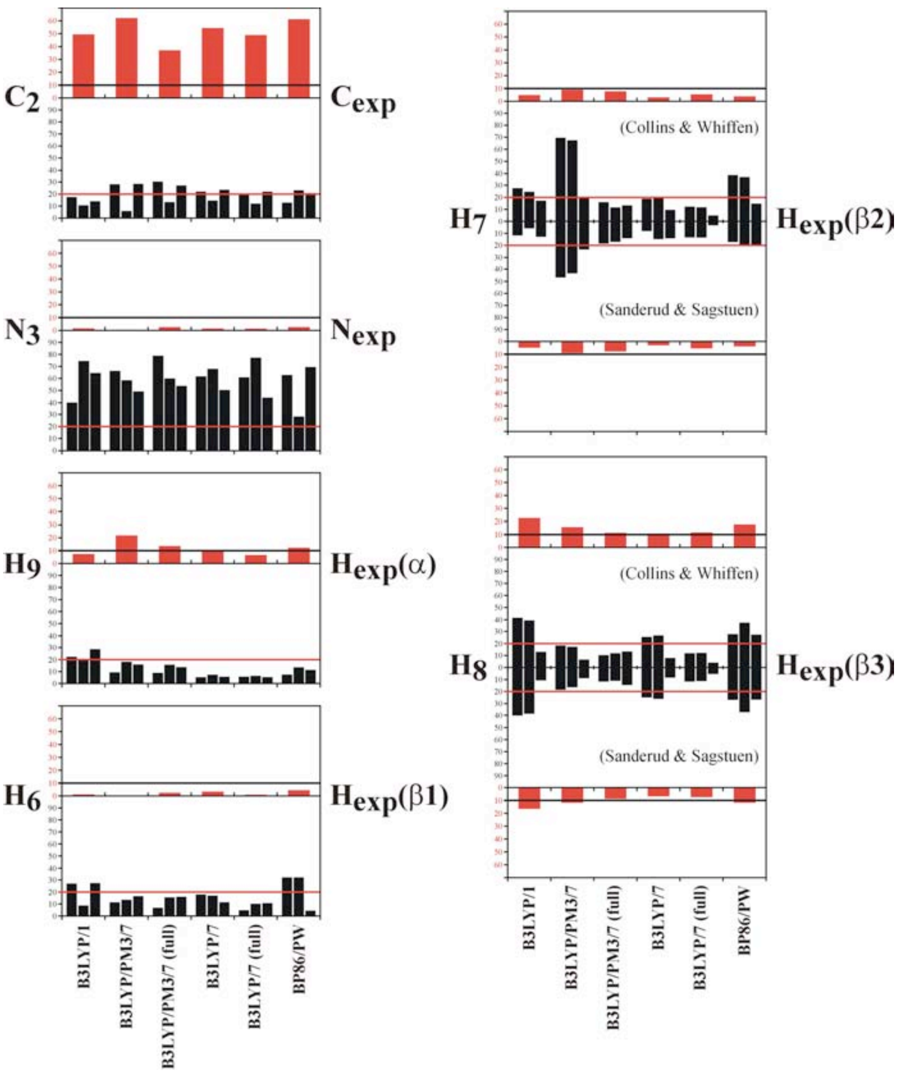

Figure 6.6: Experimental versus calculated hyperfine tensors for the geometries obtained at various levels of theory. Absolute differences (in MHz) between calculated and experimental isotropic hyperfine couplings are represented as red bars at the top of each graph. The deviations of the measured and predicted hyperfine tensor principal directions (in degrees) are given as black bars, with - from left to right - minor, intermediate and major anisotropic eigenvalues.

Single molecule calculations

Based solely on isotropic hyperfine coupling constants, the B3LYP/1 conformer offers a moderate agreement with experimental data. For the C_2 and H_8 couplings, substantial errors (about 50 MHz and 20 MHz, respectively) are observed, violating

criterion I. The calculated couplings are furthermore quite similar to those predicted in earlier single molecule calculations (see table 6.2), apart from the C_2 carbon coupling which is seriously underestimated in our B3LYP/1 calculation but nicely reproduced by the UQCISD/1 and B3LYP/CPCM/1. This disagreement looks somewhat surprising but is due to vibrational averaging effects, which are taken into account in the latter two studies. The B3LYP/Onsager/1 of Ban et al. [117] and our B3LYP/1 approach both predict almost identical couplings. Some slight differences appear for the H_7 and H_8 amino protons (77 MHz versus 60 MHz) but the somewhat better experimental accordance for the B3LYP/Onsager/1 prediction can be traced back to the additional rotation of the amino group about the C_2-N_3 bond, which is imposed in the model of Ban et al. This internal rotation is not based on first principles, but gives an indication of how to improve the agreement with experiment.

Moreover, the B3LYP/1 geometry does not succeed in predicting overall satisfactory principal hyperfine directions. Large discrepancies are noticeable and **criterion II** is violated in all but two cases. A quite good agreement is found with the C_{exp} directions and for H_7. The calculated principal axes differ only 10° from those of the $H_{exp}(\beta 2)$ tensor measured by Sanderud & Sagstuen [114]. The largest deviations from experiment, on the other hand, are obtained for the N_3 and H_8 principal axes. They can rise up to 70° and more.

If we consider the proton EPR parameters in particular as key probes for the accuracy of the proposed structure, a poor result is achieved since both criteria I and II are not met for the H_8 proton. Therefore, the B3LYP/1 geometry must be rejected as is does not yield a good prediction of the EPR data for the considered glycine radical.

Cluster calculations – B3LYP/PM3/7 and B3LYP/7

In comparison with the very simplified single molecule approach, an important improvement is obtained for the H_7 and H_8 isotropic hyperfine coupling constants in both the B3LYP/PM3/7 and B3LYP/7 cluster calculations. The latter geometry almost perfectly reproduces the experimentally observed difference in coupling constants (20 MHz). On the other hand, the B3LYP/PM3/7 geometry fails for the α-hydrogen (H_9) and the description of the C_2 coupling is even worse with respect to all other calculations. Apart from the particular C_2 hyperfine interaction, B3LYP/7 is the only level of theory able to predict isotropic coupling values that meet **criterion I**.

A similar discussion can be held on the reproduction of the hyperfine principal directions. A careful review of the black bars in Figure 6.6 learns that the cluster calculations are completely missing the hyperfine principal axes for the nitrogen atom N_3, but that they nicely succeed in predicting the axes for the four hydrogen atoms. One large discrepancy attracts attention: the two axes belonging to the two minor anisotropic coupling components predicted for the H_7 proton in the B3LYP/PM3/7 approach. The orientations of these axes differ by more than 45° from experiment (either Collins & Whiffen [106] or Sanderud & Sagstuen [114]). However, we notice that the minor and intermediate anisotropic coupling eigenvalues are close to degeneracy (-4.2 versus –4.7 MHz). Eigenvectors of degenerate eigenvalues are not uniquely determined. Only the plane of the axes perpendicular to the principal axis corresponding to the major (non-degenerate) eigenvalue (+8.9 MHz) is completely defined, and this plane seems to be reproduced within the 20° threshold of **criterion II**.

This is a striking phenomenon, which also arises at other levels of theory: one component (corresponding to the largest T_{aniso}) which is in excellent agreement with experiment, and the two minor components exhibiting large, but equal discrepancies with experiment. In all these cases, the two minor T_{aniso} values are close to each other, generating large inaccuracies in the determination of the eigenvectors. A simple rotation of the last two principal axes about the former well determined axis would be sufficient to get an excellent reproduction of all hyperfine principal directions.

Cluster calculations – B3LYP/PM3/7(full) and B3LYP/7(full)

In an attempt to break this quasi-degeneracy, the size of the model space was increased. This is achieved by taking explicitly into account the nearest molecular environment of the radical for the evaluation of the EPR parameters. The results of these additional cluster calculations are labeled B3LYP/PM3/7(full) and B3LYP/7(full), as stated earlier. What could be expected indeed happens: the degeneracy of the two lowest eigenvalues of the T_{aniso} tensor is completely removed, and the agreement with experiment becomes excellent. This spectacular change is observed for H_7 in B3LYP/PM3/7(full), for H_8 in B3LYP/7(full) and to a lesser degree for H_6 in B3LYP/7(full). As visible in Figure 6.6, **criterion II** is well met for these protons.

All discussed cluster approaches utterly fail to correctly predict the N_3 nitrogen hyperfine tensor principal directions. In addition, any sign of improvement upon increasing the level of theory is indiscernible (e.g. comparing the B3LYP/PM3/7 and B3LYP/7(full) results). This suggests that either DFT is completely unstable to calculate nitrogen hyperfine tensor axes, or that an ambiguity persists in the description of the experimental tensor principal directions. Taking into account the satisfactory reproduction of the nitrogen hyperfine coupling constant using DFT methods on the one hand, and the contradictions between the different experimental studies concerning the nitrogen tensor axes on the other, we tend to assume the latter suggestion to be correct.

The enlargement of the model space has also a beneficial influence on the reproduction of the C_2 isotropic coupling constant: the value of 64.6 MHz is raised to 87.7 MHz in B3LYP/PM3/7(full). This isotropic carbon coupling is still too small however to achieve **criterion I**, but as similar low values are reported throughout all other calculations, this can be attributed to the only moderate basis size, as opposed to the more specialized basis sets (EPR-II) used in, for instance, the B3LYP/CPCM/1 approach [118]. Another contributing factor to the underestimation of this coupling is the absence of any temperature consideration in our model approaches. Since calculations are performed at 0 K in vacuo, temperature effects – such as vibrational averaging motions treated in the B3LYP/CPCM/1 and UQCISD/1 models – are not taken into account. As reported in [116] and [101], these effects will also significantly alter the isotropic hyperfine coupling constants. All other reported couplings remain quite comparable. The best agreement for all protons is obtained within the B3LYP/7(full) cluster approach, which makes sense considering the superior level of theory.

The improvement of the calculated hyperfine directions restricts to some extent the validity of the observation formulated in [118] that "the magnetic properties of a glycine radical in its zwitterionic form are scarcely affected by the crystalline environment". As corroborated by the differences between the B3LYP/7 and B3LYP/7(full) calculations, only the (proton) hyperfine couplings are largely unaffected by the presence of a crystal lattice, but this may not be extended to the hyperfine principal directions, where a more elaborate description of the surrounding may lift the possible degeneracy, leading to a more accurate determination of the axes.

Periodic calculations

A good overall agreement with experiment is obtained for the calculated isotropic coupling constants of the BP86/PW structure, apart from the C_{exp} coupling, but this is common to all calculations. Nevertheless, **criterion I** is violated for the H_8 and H_9 couplings, although a qualitative agreement with the experimental amino proton coupling scheme is maintained.

On the other hand, the predicted hyperfine tensor principal directions for these amino protons largely deviate from the experimental principal axes. Apart from a moderate agreement between the BP86/PW H_7 directions and the results of Sanderud & Sagstuen, a deviation of 30° to 40° on average is obtained for all β-protons. This failure to meet **criterion II** is undoubtedly linked to the incorrect description of hydrogen bonds – as argued in sections 3.2 and 3.4 – and confirms that periodic calculations with the use of gradient corrected functionals do not meet the requirements of a viable model to predict EPR parameters of a radiation-induced radical in glycine. We do, however, want to stress that the EPR parameters in the periodic approaches are obtained by performing calculations on the single radical. Up to now, no program packages are available that allow the calculation of EPR data using the full model space, i.e. a periodic model, with plane waves. Even though such calculations are likely to cause an improvement, the hydrogen bonds deviate too much in this approach to retain the model. Further model development is therefore needed for this type of calculations.

6.5 CONCLUSIONS

In this study, we have computed the geometries and EPR parameters of the $^{+}NH_3$-$^{\bullet}CH$-CO_2^- radiation-induced radical of α-glycine in the solid state. Several model spaces were considered, including a single molecule approach, cluster models and periodic calculations, all basing on density functional theory. The structural characteristics of the obtained geometries have been compared with the experimental values obtained from X-irradiated crystals of α-glycine at 23 K.

In an initial assessment of the efficiency for each approach, it was found that the level of theory has a most distinct effect on the description of hydrogen bonds interconnecting adjacent glycine molecules within the crystal. It was established that a full ab-initio cluster model is the most favorable method and that periodic calculations with use of GGA functionals inaccurately account for the hydrogen bond interactions. Subsequently, these methods were applied to determine the optimal geometry of the glycine radical within the crystal. In this application, however, a correct description of hydrogen bond interactions appears essential to yield representative EPR parameters for the glycine amino protons, whose internal rotation with respect to the crystal is mainly determined by hydrogen-bonding forces.

In an ensuing, comprehensive study of the EPR parameters, calculated on the optimized geometries, both the hyperfine coupling constants and the hyperfine tensor principal directions were cross-referenced with selected data, taken from a wealth of (albeit sometimes rather old) experimental studies on glycine. In general, the isotropic hyperfine couplings are not exactly reproduced, although a qualitative agreement is always acquired. Especially the calculated isotropic carbon couplings are only a fraction of the actual experimental value. According to literature, these deviations must be attributed to other factors such as temperature effects or, to a minor extent, basis size effects. Since the trends observed for the calculated isotropic hyperfine constants could be transferred to the anisotropic couplings, they have consequently not been dealt with in detail.

In this paper, the relevance of a good reproduction of the hyperfine tensor principal axes has been stressed. It can be regarded as a sensitive probe for the accuracy of the proposed methodology to describe the glycine radical. Few levels of theory turn out to reproduce the experimental hyperfine principal directions in a satisfactory way. Only cluster methods were able to achieve this goal, the B3LYP/7 model in particular. This agreement was substantially further improved by also incorporating the explicit molecular environment of the cluster model in the EPR calculations. Predominantly in case of a quasi-degeneracy of the two lowest eigenvalues of the anisotropic tensor for the β-protons, the enlargement of the model space removes the degeneracy and predicts the axes of the two nearly degenerate values within 10° to 15° from the experimental directions.

The best overall agreement between theory and experiment is observed for the B3LYP/7(full) calculations. The isotropic coupling constants are in fair accordance with experiment (except for the C_{exp} coupling) and the hyperfine tensor principal directions deviate not much from the experimental ones, in particular for the protons where the agreement is very good (always below 13° deviation) and also for C_2, where the agreement is moderate (never more than 22°). The N_{exp} principal axes are by far not reproduced by any of the proposed models. A possible explanation for this failure lies in the inconsistencies in the experimental data. Large discrepancies are noticed between the various experiments, which make the validity of the nitrogen tensor data questionable.

Chapter 7. Radiation-induced radicals in sugar systems

Saccharides play an essential role in most biological processes. They are extremely abundant in plants and are vital in the biological energy storage and transport systems of animals. The simple sugars D-fructose and D-glucose are of particular interest in this respect, since they are the monomeric units of the disaccharide sucrose, one of the most widespread sugars in nature.

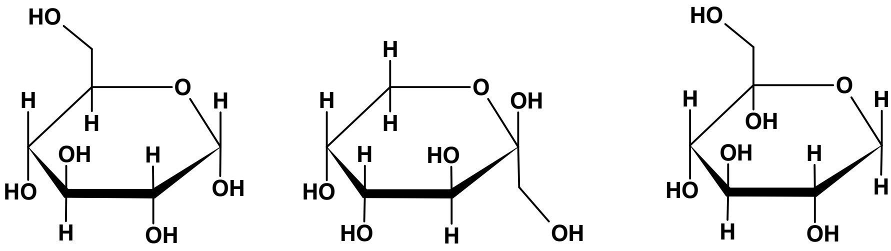

α-D-glucopyranose β-D-fructopyranose α-L-sorbopyranose

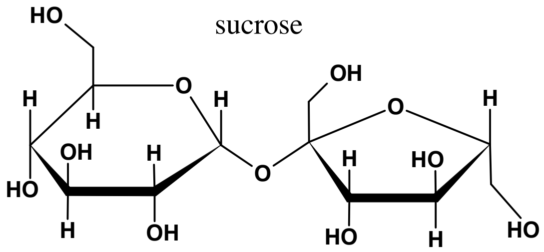

sucrose

Figure 7.1: Chemical structures for some widespread sugars.

In recent years, considerable attention has been given to radiation-induced free radicals in solid-state sugars, in the light of the radiation treatment of sugar-containing food. This treatment improves the hygienic quality, as ionizing radiation sterilizes and reduces the bioburden. In Belgium alone, about 10000 tons of food per year is irradiated on these grounds. From the safety and regulatory point of view, identification of irradiated food and determination of irradiation doses is therefore a major concern. This has spawned research into the development of dosimetric protocols for the various foodstuffs that are suitable for radiation treatment.

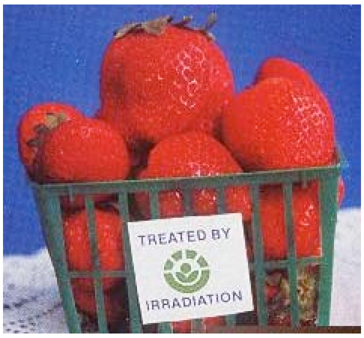

Figure 7.2: In Belgium, food treated with irradiation should be labeled accordingly.

In this respect, Electron Paramagnetic Resonance (EPR) spectroscopy might be one of the most reliable methods to detect irradiation, because of the relative stability of radiation-induced radicals in solid or dried parts of certain foodstuffs. The presence of these radicals constitutes a suitable probe for the absorbed doses of irradiation, whether applied on purpose or contracted by accident – e.g. after the 1986 Chernobyl nuclear disaster. Several dosimetric protocols have already been established for a number of foodstuffs, such as bone-containing [124] or cellulose-containing food [125] and more recently, for a limited number of sugar-containing foods [126]. Nevertheless, a more general protocol for foodstuffs containing sugar is still in a developing stage. Consequently, a number of studies examine the overall dosimetric characteristics and the ensuing applications of the sugar system [127]. Other studies have – on a more fundamental level – rather focused on trying to understand on a fundamental level the nature of the sugar EPR spectra by elucidating the identity and structural characteristics of the radicals involved. For this purpose, sucrose has been examined using EPR techniques under various experimental conditions, such as (frozen) solution [128], powders [129] and single crystals [130, 131, 132]. Up to now, however, an unambiguous identification of the radiation-induced solid-state sucrose radicals has yet to be made. Gräsland and Löfroth [131] were the first to postulate that in fact two types of radical species coexist in sucrose, each located respectively in the glucose and fructose monosaccharide units of sucrose. In later studies [132], the number of possible sucrose radicals even increased. However, the fact that radicals in the irradiated sucrose crystal may be located on the separate monomer sugars, prompted researchers to first investigate the EPR characteristics of these simple sugars in detail.

From another viewpoint, the study of free, radiation-induced radicals in carbohydrates is also important for the understanding of radiation damage processes in DNA [133, 134], eventually causing cell degradation. It is now widely accepted that single-strand breaks in DNA occur via sugar radical intermediates [134, 135, 136], derived from deoxyribose in the phosphate sugar backbone, as illustrated in Figure 7.3.

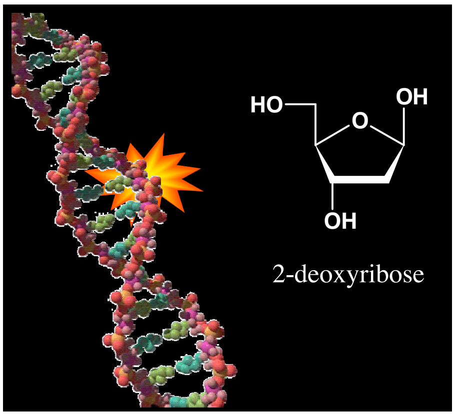

Figure 7.3: The deoxyribose backbone sugar in DNA is a receptive site for possible radiation damage.

Better insights in the radiation damage processes for sugars in general and the resulting radical structures may even further improve this understanding of DNA damage as a result of irradiation.

Mindful of either viewpoint, we will examine in this work some of the radiation-induced radicals of β-D-fructose, α-D-glucose and α-L-sorbose. These sugars are all isomers of $C_6H_{12}O_6$, and their structures are presented in Figure 7.1. Taking into consideration that even monomer carbohydrates are substantially larger than the average amino acid, cluster or periodic calculations for these systems would require considerably more computational resources. For that reason, we have in this work only performed single molecule calculations. Yet, as will become clear, even such a fairly simple model space approach can render quite good qualitative (and sometimes quantitative) results.

Chapter 8. Radiation-induced radicals in β-D-fructose

REFERENCE: [137].

8.1 BACKGROUND

It was only recently that an EPR study was conducted on irradiated solid-state β-D-fructose using ENDOR and EIE [138]. This work reports the identification of two dominant radicals indicated as F1 and F2. Both radicals are characterized by three β-type proton hyperfine couplings, as detected by the EI-EPR experiment. This would suggest that the unpaired electron of both fructose radicals interacts with three protons yielding six hydrogen hyperfine tensors. However, only five tensors have been determined with ENDOR, since the missing tensor in F2 probably corresponds with a small hyperfine interaction that could not be determined unambiguously (see Table 8.1).

	Experiment					
	Aiso	Taniso	Aaniso	Axes		
F1_β1	96.90	-4.2	92.7	-0.448	-0.253	0.858
		-2.9	94	0.675	-0.724	0.139
		7.1	104	0.586	0.642	0.495
F1_β2	37.30	-4.1	33.2	-0.476	0.86	0.185
		-2.4	34.9	-0.78	-0.51	0.362
		6.6	43.9	0.406	0.028	0.914
F1_β3	9.30	-3.3	6	-0.318	-0.946	-0.066
		-1.7	7.6	-0.225	0.008	0.974
		5	14.3	-0.921	0.325	-0.215
F2_β1	87.50	-3.6	83.9	-0.479	-0.365	0.798
		-3.2	84.3	0.642	-0.766	0.035
		6.8	94.3	0.598	0.529	0.601
F2_β2	43.10	-3.9	39.2	-0.262	0.929	0.263
		-2.7	40.4	-0.852	-0.351	0.389
		6.5	49.6	0.453	-0.122	0.883

Table 8.1: Experimental hyperfine coupling constants and direction cosines of radicals F1 and F2 as determined in [138]. A_{iso}, T_{aniso} and A values are in MHz; direction cosines are referred to the *abc* reference axis system of the crystal.

In a preliminary computational study on the radiation-induced radicals in fructose and sucrose [139], a model structure conform Figure 8.1 was tentatively proposed for both radical species in fructose. This identification relied mainly on a close match between experimental and calculated isotropic hyperfine couplings in four distinct conformations, differing only in a rotated position of the CH_2OH group. However, the best fit of the theoretical isotropic hfcc's with the experimental data was never found sufficient to distinguish between any of these four conformations.

Furthermore, it was suggested that both paramagnetic species are in fact manifestations of the same type of radical – generated in two slightly different orientations with respect to the crystal matrix – which would explain the significant similarity between the principal values and axes of the β1 and β2 hyperfine tensors in F1 and F2 [138]. An unambiguous differentiation between these two species was nevertheless impossible, as the accuracy of the adopted computational approach proved insufficient.

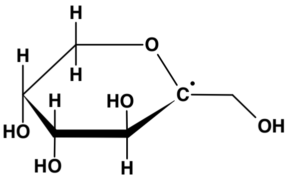

Figure 8.1: model structure for the fructose radical as proposed in [138].

8.2 MODEL SELECTION

β-D-Fructose adopts the pyranose form in the crystalline state. Its structure was thoroughly examined by Takagi and Jeffrey in a neutron diffraction study [140]. They reported that the crystal is orthorhombic (space group $P_{2\perp2\perp2\perp}$) and that its unit cell – with dimensions a=9.191, b=10.046 and c=8.095 – contains four fructose molecules. The structure of one of these molecules is visualized in Figure 8.2. In view of the fact that Vanhaelewyn et al. [138] reported three β-type couplings for both detected radical species, only a limited number of initial radical geometries can be proposed from the undamaged fructose crystal structure that meet the experimental requirements. Radical models were selected, starting from the assumption that in the process of radiation-induced radical formation, the pyranose ring structure of fructose was preserved. Furthermore, we required the models to be neutral. Starting from these assumptions, all possible homolytic cleavages of the fructose ring substituents had to be considered.

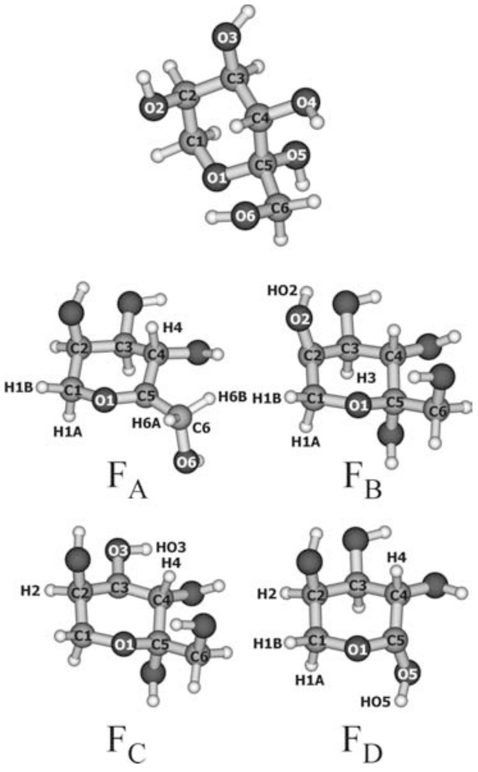

Figure 8.2: Molecular structure of β-D-Fructose as determined by neutron diffraction [140] and the optimized geometries of the proposed model radicals.

First, we looked at the possible radiation products with an abstracted hydroxyl group. By removing the OH group from carbon atoms C_2 through C_6 in the undamaged molecular structure of fructose, these carbon atoms become radical centers. In the case of C_2, C_3, C_4 and C_6 a structure is generated with one hydrogen directly bound to the carbon carrying the unpaired electron. The hyperfine coupling of this proton would undeniably be visible experimentally as it displays the α-type characteristics. Since both F1 and F2 only display three β-type couplings in the experiment, the aforementioned radiation products can be eliminated. Abstraction of the OH group from C_5 does not yield a structure with an α-type proton, but is instead characterised by an unpaired electron that is presumably delocalised over C_5 and O_1. Furthermore, at least three protons are suitably located to produce a β-type coupling with the radical center: the protons of the hydroxymethyl group at C_6, the proton at C_4, and – through the probable delocalisation over the ring oxygen – both protons at C_1. Since this structure was potentially consistent with the experimental results, it has been retained as a possible candidate for the experimentally observed radicals (F_A in Figure 1).

A second set of possible radicals is formed with the extraction of a hydrogen from the undamaged β-D-fructose structure. Hydrogen abstraction from C_1 and C_6 yields structures with an α-type proton so these can be eliminated. The radical created by abstracting a hydrogen from C_4 can also be rejected as a possibility, since no three protons can be found that are in a β-position relative to the unpaired electron. The structures with one hydrogen removed from either C_2 or C_3 – respectively denoted by F_B and F_C in Figure 1 – were further examined in our calculations. Both structures are potentially consistent with the experimental data, since at least three β-type protons can be identified. In F_B both C_1 protons, the hydroxyproton at O_2 and the proton at C_3 can produce a β-type coupling with the unpaired electron, while in model structure F_C the protons at C_2 and C_4 together with the hydroxyproton at O_3 are in a β-position relative to the unpaired electron.

Finally, a fourth model radical structure was proposed that was generated by homolytic cleavage of the hydroxymethyl group from carbon C_5. This leaves a hydroxygroup directly bound to the radical center, which is most probably delocalised over ring oxygen O_1 and carbon C_5. Four possible β-type couplings can be generated in this structure by ring protons H_{1A}, H_{1B} through delocalisation of the radical center, ring proton H_4 and by the hydroxyproton H_{O5}. This candidate structure was labelled F_D and is also included in Figure 8.2.

8.3 COMPUTATIONAL DETAILS

In total, four model radical structures were proposed that could potentially yield EPR parameters in agreement with the experimental results. Extensive single molecule calculations were performed on these models to assess the value of each model separately. Hence, the four initial geometries for the fructose radicals were first further refined by optimization in a DFT framework using the B3LYP functional [28]. Molecular orbitals were expanded in a triple-ζ 6-311G basis augmented with single d polarisation functions [33]. All calculations were performed with the Gaussian 98 package [30]. Subsequently, isotropic and anisotropic components of the hyperfine tensor were calculated, as well as the associated eigenvectors. To allow for the analysis of the latter parameter, a relative approach – as outlined in section 4.2.1 – was adopted. In a separate set of calculations (not taken up) an attempt was made to perform EPR calculations using the "Fixed Axes" method, but this approach proved invalid.

The EPR calculation was also done using a B3LYP functional in Gaussian 98. Even though specialized basis sets exist for EPR calculations (such as the EPR-III basis set of Barone [34]), we chose to perform our calculations in a triple-ζ 6-311G basis augmented with single d polarisation functions. Representative test calculations with the EPR-III set were performed, but only slight changes in the calculated EPR parameters were observed, despite a substantially larger computational cost. A more detailed discussion on these test calculations will be given in the next section.

8.4 RESULTS AND DISCUSSION

8.4.1 Model structure F_A

As already noted, the model radical F_A is obtained by removal of the hydroxyl group from the carbon C_5 in the fructose molecule. In the optimized radical structure, the unpaired spin is mainly located at the carbon atom C_5 and to a smaller extent at the oxygen O_1 with respective spin densities of 0.83 and 0.12. We also notice that in the optimized radical geometry the sp^3 hybridisation on C_5 is partly retained with respect to the undamaged fructose molecule. This can roughly be verified by the out of plane deviation of the C_5 carbon center, as measured by the angle between the planes through atoms C_6-C_4-O_1 and C_4-O_1-C_5 respectively. In the fructose molecule this angle amounts to –37.4°, while in the optimized radical geometry of F_A it reduces to –19.2°.

The most relevant degree of freedom in the single molecule approach of F_A is the internal rotation of the hydroxymethyl group about the C_5–C_6 single bond, characterized by the O_6-C_6-C_5-C_4 torsional angle. As this torsional angle will only be fixed in a cluster model calculation due to the formation of hydrogen bonds with the surrounding molecules, we investigated the fluctuation of the isotropic hyperfine coupling constants of the hydrogen atoms in F_A as a function of the torsional angle O_6-C_6-C_5-C_4. This constitutes just the advantage of the single molecule approach: to scan all geometries – allowed by the degrees of freedom – in an attempt to search for specific geometries that are suitable for a fair reproduction of the experimental data. This should allow us to put forward a fairly accurate conformation for the radical in the crystalline state.

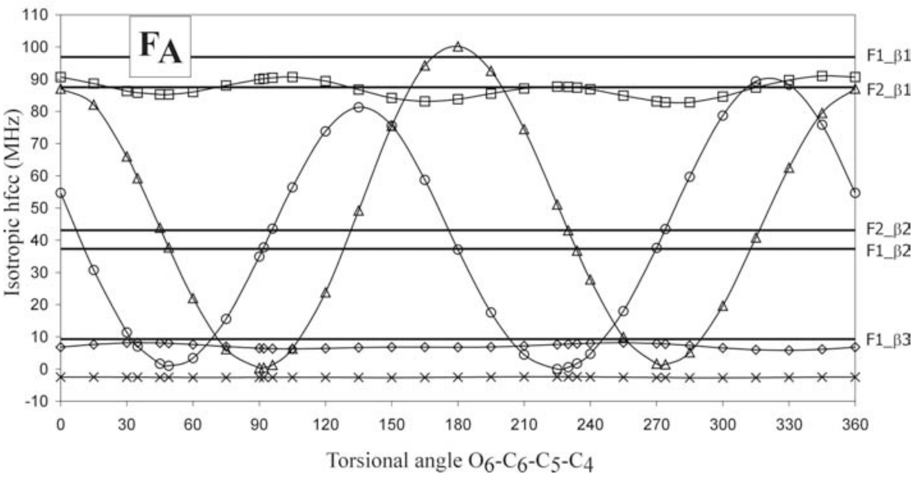

Figure 8.3: Isotropic proton hfcc's in model radical F_A as a function of the hydroxymethyl group rotation (● H_{1A}; × H_{1B}; □ H_4; H_{6A}; ○ H_{6B}; all other proton hfcc's were close to zero throughout the rotation and are therefore not included). The experimental hfcc values are indicated by thick solid lines.

The results of the variation of the torsional angle O_6-C_6-C_5-C_4 are given in Figure 8.3. As could be expected, the hydroxymethyl proton hfcc's of H_{6A} en H_{6B} are largely affected by their position. They show a somewhat sinusoidal behaviour in function of the torsional angle. The experimentally measured isotropic hfcc values are also displayed in this figure (thick solid lines), and we easily observe that eight conformations may possibly lead to a fair reproduction of the experimental results. We will first compare the theoretical results with the couplings of the experimental F1 species. The large F1_β1 coupling of 96.6 MHz most likely corresponds to the H_4 hfcc, which fluctuates about 90 MHz throughout the rotation of the hydroxymethylgroup. The H_{1A} and H_{1B} proton hfcc's remain practically constant during the rotation (roughly 8 MHz and –3 MHz respectively), but the H_{1B} proton displays a smaller coupling than H_{1A}. If we assign the H_{1A} hfcc to the experimental F1_β3 coupling (9.3 MHz), it is clear that one of the hydroxymethyl proton hfcc's should correspond with the F1_β2 coupling (37.3 MHz) while the other should be close to zero and consequently not detectable experimentally. Figure 8.3 reveals that only four conformations succeed in reproducing the three experimental signals of F1 theoretically:

- a torsional angle of 49° yields an H_{6A} hfcc of 37.8 MHz corresponding with the experimental F1_β2 coupling of 37.3 MHz;
- a torsional angle of 92° meets the H_{6B} hfcc of 37.8 MHz with the experimental estimate;

- at 234° a correspondence is found for the H_{6A} hfcc (36.8 MHz), while
- at 270° the H_{6B} hfcc yields 37.6 MHz.

The four proposed cases all predict an hfcc for the counterpart proton (H_{6A} or H_{6B}) below 6 MHz agreeing with the fact that these signals have not been detected experimentally. This observation of four possible conformations is quite analogous to the conclusion of an earlier, preliminary study on fructose [139].

To disentangle between these four proposed conformations, a detailed study was made of the anisotropic components of the calculated hyperfine coupling tensors and their corresponding spatial directions. The anisotropic components of the hyperfine tensor, however, were all in close agreement with the experimental results and did not differ significantly from each other. So, in order to single out the conformations that correspond with reality, it is necessary to look at the direction cosines of the associated eigenvectors.

The three principal axes of the experimental hyperfine tensors are specified by their corresponding direction cosines with respect to the reference frame, which usually coincides with the crystal axes (schematically shown in Figure 8.4(a)). The experimental values for the two observed radicals F1 and F2 are reported in Table 8.1. Since the crystalline environment was not simulated in the present single molecule calculations, it is impossible to insert the same reference axis system as was done in the experiment. To solve this ambiguity, we adopt a relative method for analysing these EPR parameters, as explained in section 4.2.1. This requires that the mutual angles between the calculated proton tensor axes are compared with the mutual angles between the experimental principal axes of the observed radicals, as illustrated in Figure 8.4(b) for the β1 and β3 signals in radical F1.

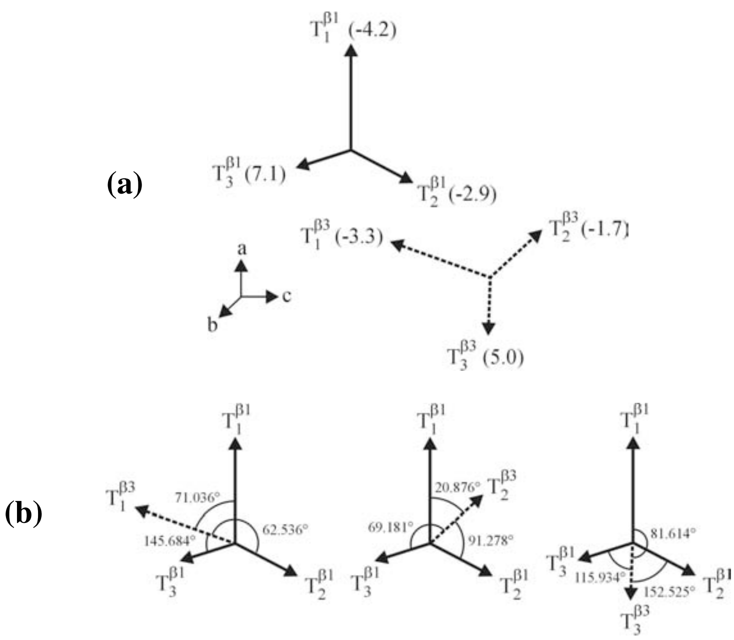

Figure 8.4: **(a)** The principal axes of the experimental β1 and β3 signals as given by their direction cosines with respect to the *abc* reference frame. **(b)** displays the mutual angles; the principal axes of the hyperfine tensors are specified by their corresponding anisotropic value (in MHz).

In this way we eliminate the choice of the reference axis system and we obtain an additional reliable tool to differentiate between the four conformations proposed by the theory. It should be stressed that there is still some ambiguity in fixing the relative angles (φ or π-φ) due to the fact that the absolute sign of the experimental direction cosines cannot be determined. Furthermore, it was not determined in the experiment whether all reported proton tensors refer to the same magnetically distinguishable site in the crystal lattice. In the case of fructose, there are four such sites, as the orthorhombic unit cell contains four molecules. Consequently, we must take into account that the tensor eigenvectors can be located in different spatial quadrants. These ambiguities were taken into consideration in our analysis of the relative angles, which are reported in Table 8.2 along with their calculated counterparts.

			F1_β1		
	Aiso		96.9		
		Taniso	-4.2	-2.9	7.1
F1_β3	9.3	-3.3	71.036	62.536	145.684
		-1.7	20.876	91.278	69.181
		5	81.614	152.525	115.934

			F1_β1		
	Aiso		96.9		
		Taniso	-4.2	-2.9	7.1
F1_β2	37.3	-4.1	81.124	156.700	68.618
		-2.4	37.917	96.143	127.248
		6.6	53.510	67.617	44.947

			F1_β2		
	Aiso		37.3		
		Taniso	-4.1	-2.4	6.6
F1_β3	9.3	-3.3	132.387	45.039	102.461
		-1.7	72.890	58.379	36.969
		5	47.316	61.648	124.127

			F2_β1		
	Aiso		87.5		
		Taniso	-3.6	-3.2	6.8
F2_β2	43.1	-3.9	90.213	150.479	60.465
		-2.7	32.147	105.333	117.490
		6.5	57.834	65.468	42.471

			H4		
	Aiso		87.410		
		Taniso	-2.005	-5.274	7.279
H1A	7.864	-4.309	84.201	75.447	164.286
		-2.886	10.147	83.388	82.338
		7.195	81.705	163.958	103.634

			H4		
	Aiso		87.410		
		Taniso	-2.005	-5.274	7.279
H6A	36.768	-4.678	76.356	125.998	39.295
		-2.979	35.393	108.291	119.132
		7.657	58.060	41.787	66.103

			H6A		
	Aiso		36.768		
		Taniso	-4.678	-2.979	7.657
H1A	7.864	-4.309	124.991	50.963	121.595
		-2.886	66.230	39.317	60.729
		7.195	44.502	86.029	134.223

Table 8.2: Comparison of the angles between the calculated principal axes of the F_A proton hyperfine tensors (calculated for a torsional angle of 234°) and the angles between their experimental counterparts.

It is found that the angles between the principal axes, calculated for the conformation at 234° are in close agreement with the angles between the experimental F1 signals. The other conformations do not succeed by far in reproducing the experimental findings. It should be noted, however, that the smallest two anisotropic components for the H_4 proton have been switched to allow for a fair comparison. This means that, for the conformation at 234°, the eigenvector for the –2.0 MHz anisotropic component of H4 matches with the eigenvector of the –4.2 MHz experimental component of F1 and likewise the –5.3 MHz eigenvector of H_4 matches with the –2.9 MHz F1 experimental component. This interchange is not dramatic since both components can be considered near degenerate, and is supported by a theoretical analysis of the angles formed by the H_4 principal axes with those of the two other protons H_{6A} and H_{1A}. The reason for this switch between the two low anisotropic component axes can be attributed to the fact that the present calculations did not involve any simulation of the molecular environment. Apart from this interchange, all anisotropic and isotropic proton hyperfine couplings in experimental species F1 are in close agreement with the coupling values in model radical F_A, as summarized in Table 8.3.

	Conformation at 234°							Experimental Match
	6-311G*			EPR-III			Δdirection	
	Aiso	Taniso	A	Aiso	Taniso	A		
H1A	7.9	-4.3	3.6	8.5	-4.4	4.1	1.489	F1_β3
		-2.9	5.0		-2.7	5.8	1.495	
		7.2	15.1		7.1	15.6	0.172	
H1B	-2.4	-3.1	-5.5	-2.7	-3.0	-5.7	5.348	
		-2.6	-5.0		-2.5	-5.2	5.352	
		5.7	3.3		5.6	2.9	0.183	
H4	87.4	-2.0	85.4	94.9	-2.2	92.7	3.656	F1_β1
		-5.3	82.1		-5.2	89.7	3.652	
		7.3	94.7		7.4	102.3	0.343	
H6A	36.8	-4.7	32.1	39.5	-4.8	34.7	1.002	F1_β2
		-3.0	33.8		-2.9	36.6	1.026	
		7.7	44.5		7.7	47.2	0.212	
H6B	1.7	-5.1	-3.4	2.0	-5.3	-3.3	4.972	
		-4.0	-2.3		-4.0	-2.0	4.978	
		9.1	10.8		9.3	11.3	0.285	

Table 8.3: Summary of calculated proton hyperfine tensor components for the F_A conformation with a torsional angle of 234°. The A_{iso}, T_{aniso} and A values (in MHz) are reported for a 6-311G* and an EPR-III basis. No direction cosines are given, but anisotropic values are ordered in comparison with their experimental counterparts in Table 1. $\Delta_{direction}$ is the difference (in degrees) between the anisotropic principal axes calculated with both basis sets.

The fair reproduction of the mutual angles between the anisotropic principal axes strengthens the identification of the experimental species F1 as having a radical structure conform model F_A and with a hydroxymethyl torsional angle of 234° for O_6-C_6-C_5-C_4. An additional calculation was performed on this conformation to assess the choice of the basis set used in the calculation of the EPR parameters. EPR parameters calculated with an (extended) EPR-III basis – which has been constructed by Barone for specific use in this field [34] – are compared to those obtained with a 6-311G* basis (Table 8.3). We notice only small discrepancies, apart from the H_4 coupling which is substantially higher in the (EPR-III) large basis and is in fact in much better agreement with the experimental β1 hfcc (Table 1). The anisotropic principal values are nearly identical for both basis sets and the relevant principal directions diverge with a maximum of some 4°. So, only for the isotropic hyperfine couplings, a better agreement with experimental data is obtained for the EPR-III basis. However, since the hfcc's of H_{6A} and H_{6B} change only in a minor way with respect to the 6-311G* calculation, the use of a larger basis set has no effect on the final identification of the hydroxymethyl torsional angle at 234°.

The experimental F2 species also shows three β-type couplings in the EI-EPR spectrum that are very similar to the first F1 species. However, only two β-type couplings could be determined unambiguously with ENDOR. From Figure 8.3 it is clear that the experimental isotropic hyperfine coupling constants of F2 are reproduced at four possible conformations of F_A, differing from the previous four conformations by only a small fraction of the hydroxymethyl torsional angle (about 4°). This minor difference is due to the extreme sensitivity of the isotropic hfcc's to slight changes in the relative position of the hydroxymethyl protons with respect to the unpaired spin density on the sp^3-like lobe of C_5. A study of the anisotropic hyperfine eigenvectors is again required to disentangle the four conformations. In F2 however, only the mutual angles between the β1 and β2 anisotropic components are available for comparison with calculated results (also taken up in Table 8.2). In addition, there is a striking resemblance between these values and those between the β1 and β2 signals in radical F1. This indicates that the F2 conformation is very similar to the F1 conformation. A detailed investigation of the experimental data reveals that the difference in spatial direction of the observed anisotropic components are very small (Table 8.4) and are almost all of the same magnitude for β1 and β2. Due to the missing β3 signal in F2, there is insufficient ground to make an essential difference between the two experimentally observed F1 and F2 species and we sustain the conclusion that both exhibit the same radical structure according to the proposed F_A configuration, but with slightly altered conformations.

	F1_β1			F1_β2		
Aiso	96.6			37.3		
Taniso	-4.2	-2.9	7.1	-4.1	-2.4	6.6
Angle	7.5	6.7	8.9	13.7	10.1	9.2
Taniso	-3.6	-3.2	6.8	-3.9	-2.7	6.5
Aiso	87.5			43.1		
	F2_β1			F2_β2		

Table 8.4: Angles between corresponding principal axes for both β1 and β2 tensors in experimental radicals F1 and F2; A_{iso} and T_{aniso} values are in MHz.

8.4.2 Model structures F_B and F_C

By hydrogen abstraction from C_2 and C_3 respectively, the model radicals F_B and F_C are formed. In both optimized radical geometries, the unpaired electron is predominantly located on the carbon atoms – C_2 and C_3 have spin densities of 0.80 and 0.81, respectively – but is to some extent delocalised over the attached oxygen atoms O_2 and O_3 with respective spin densities 0.15 and 0.13. Both optimized radical geometries display a carbon radical center that retains its original sp^3 hybridisation for the larger part. In F_B, C_2 has an out of plane deviation of 23.3° versus 34.7° in the crystal, as measured by the angle between the planes O_2-C_3-C_1 and C_3-C_1-C_2. The radical center in F_C is also far from planar with an angle of 20.5° between the planes O_3-C_4-C_2 and C_4-C_2-C_3 versus 33.9° in the crystal.

Since in both F_B and F_C, the radical center is not located near the hydroxymethyl group, rotation about the C_5-C_6 axis has little or no effect on the spin density distribution throughout the radicals and consequently on the proton hfcc's. This degree of freedom can therefore be totally eliminated. On the other hand, rotation of the hydroxygroup about the C_2-O_2 and C_3-O_3 axes in F_B and F_C respectively does influence the spin density distribution. The isotropic hyperfine coupling constants of the principal protons are therefore plotted in Figure 8.5 as a function of these degrees of freedom. Both plots display a striking similarity for the hfcc's of the hydroxyprotons (H_{O2} and H_{O3}) as a function of hydroxygroup rotation. The two large maxima in each plot are encountered when the hydroxyproton is either coplanar or antiperiplanar to the orbital containing the unpaired electron. The asymmetry in both maxima is due to the non-planarity of the radical center and the largest maximum is found when the hydroxyproton is antiperiplanar to the partial sp^3 lobe of the orbital with the unpaired electron. While in only two conformations of model radical F_B the experimental results are possibly reproduced, model radical F_C has eight possible conformations.

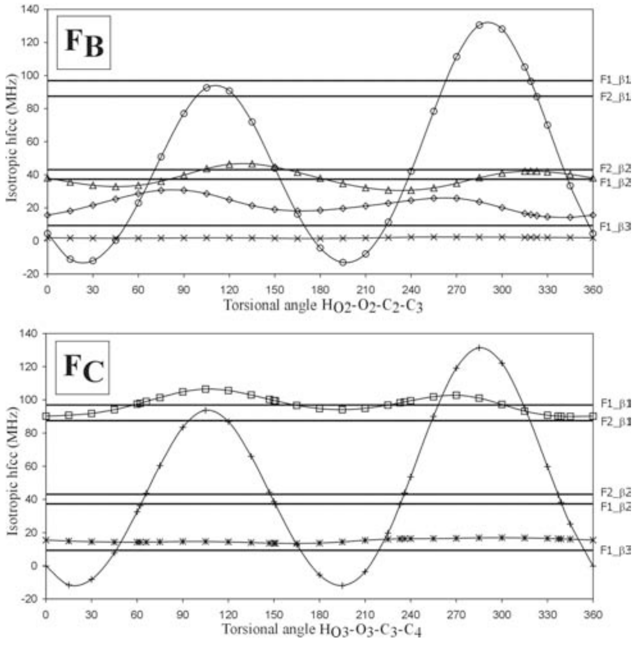

Figure 8.5: Isotropic proton hfcc's in model radicals F_B and F_C as a function of the hydroxygroup rotation (● H_{1A}; × H_{1B}; ∗ H_2; ○ H_{O2}; H_3; + H_{O3}; □ H_4; all other proton hfcc's were close to zero throughout the rotation and are therefore not included). The experimental hfcc values are indicated by thick solid lines.

In F_B, three proton hfcc's vary significantly upon rotation of the hydroxygroup. The hyperfine coupling constants of H_{1A}, H_{O2} and H_3 show a sinusoidal pattern, while that of H_{1B} remains practically constant throughout the rotation. In the search for a conformation that possibly reproduces the experimental results, H_3 most likely can account for the β2 signals in both F1 and F2, and H_{1A} can be associated with the β3 signal in F1. However, because H_{1A} becomes rather large (up to 30 MHz) at some conformations, only the region between 300° and 360° seems acceptable. In this interval, the conformation at 319° displays a H_{O2} hfcc in accordance with the β1 signal of the experimentally observed F1 radical. Even though experimentally no F2_β3 signal was quantitatively detected, Vanhaelewyn et al. [138] report a third hyperfine coupling for F2 similar to the β3 coupling in F1. It is therefore safe to assume that a conformation in accordance with F2 must be searched for in the same region between 300° and 360°. At a H_{O3}-O_3-C_3-C_4 torsional angle value of 323° a conformation is found that conclusively exhibits an H_{O2} hfcc in close agreement with the β1 signal of the F2 radical.

The model radical F_C only has three protons with significant hfcc values. The H_4 proton hfcc corresponds with the β1 signals of F1 and F2 and fluctuates around 100 MHz. The hfcc of H_2 remains more or less constant throughout the hydroxygroup rotation and accords with the β3 signal of F1. At four conformations – with H_{O3}-O_3-C_3-C_4 torsional angles of 62°, 151°, 233° and 339° – the H_{O3} hfcc accords with the F1_β2 signal. Similarly, four conformations can be found that have an H_{O3} hfcc in agreement with the F2_β2 signal – at 66°, 147°, 236° and at 337°.

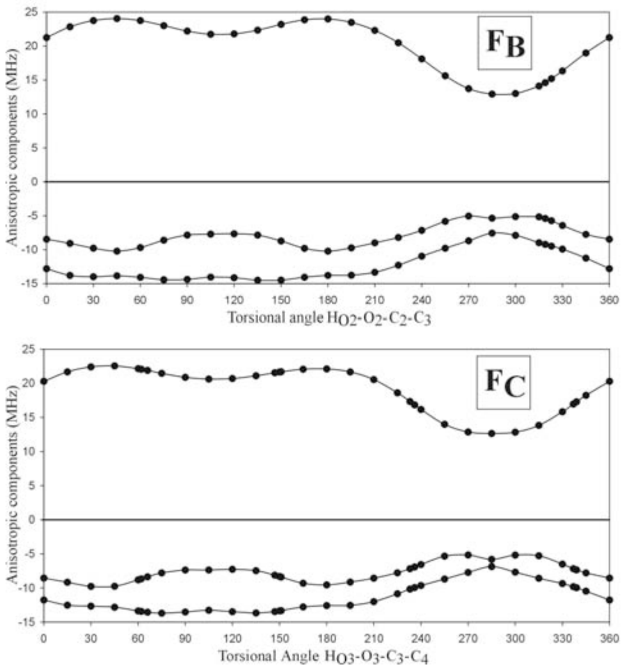

Figure 8.6: Anisotropic components of hydroxyproton hyperfine tensors in model radicals F_B and F_C as a function of the hydroxygroup rotation.

However, particularly large anisotropic components for the hydroxyproton hyperfine tensors in all conformations of both F_B and F_C instructed us to further examine these components. Figure 8.6 shows the variation of the anisotropic hydroxyproton components as a function of the hydroxygroup rotation. The largest component in both charts fluctuates at 20-25 MHz and only drops to 12-13 MHz in the region where the hydroxyproton is antiperiplanar to the unpaired electron sp^3 orbital. Similarly, the smaller anisotropic components display couplings of -10 and -15 MHz respectively, and rise to –5 and –7 MHz in the antiperiplanar region. Comparison with the experimental anisotropic components in Table 8.1 clearly shows that the theoretical predictions are far too high. Even in conformations where the hydroxyproton is more or less antiperiplanar to the unpaired electron orbital, the predicted anisotropic components are roughly twice the experimental values. This is most likely due to the high spin density on the hydroxygroup oxygen, which assigns the hydroxyproton with some α-proton character.

Despite the large anisotropic components, a number of conformations of both F_B and F_C was further analysed on the basis of the hyperfine coupling tensor direction cosines. The F_B conformations with a H_{O2}-O_2-C_2-C_3 torsional angle of 319° and 323° were examined, as were the F_C conformations at 233°, 236°, 337° and 339° for the H_{O3}-O_3-C_3-C_4 torsional angle. In all of these conformations, the hydroxyproton is more or less antiperiplanar to the unpaired electron orbital and the hydroxyproton anisotropic components bear at least some resemblance with the experimental components. However, evaluation of the mutual angles between the calculated proton tensor components and the angles between the experimental tensor components led to no comparison at all. For no conformation theoretical angles were obtained that were in agreement with the experimental ones. This fact, together with the overestimated anisotropic components, led us to the conclusion that model radicals F_B and F_C are not realistic models for the experimental radicals F1 and F2.

8.4.3 Model structures F_D

F_D is the smallest of all model radicals examined and is created by abstraction of the hydroxymethyl group from (undamaged) fructose. The unpaired spin is mainly located on the C_5 carbon atom with a spin density of 0.80, but is to some extent delocalised to the O_5 atom (0.12 spin density). Surprisingly, little or no spin density resides on the ring oxygen O_1, in contrast with the ring oxygen in model radical F_A, where the unpaired electron was also mainly located on C_5, but partially delocalised to O_1. This is probably due to the large sp^3 hybridisation character of the C_5 radical center in F_D. The out of plane deviation of this center, as expressed by the angle between the planes O_5-C_4-O_1 and C_4-O_1-C_5, is 24.7° in the model radical versus 34.5° in the fructose crystal.

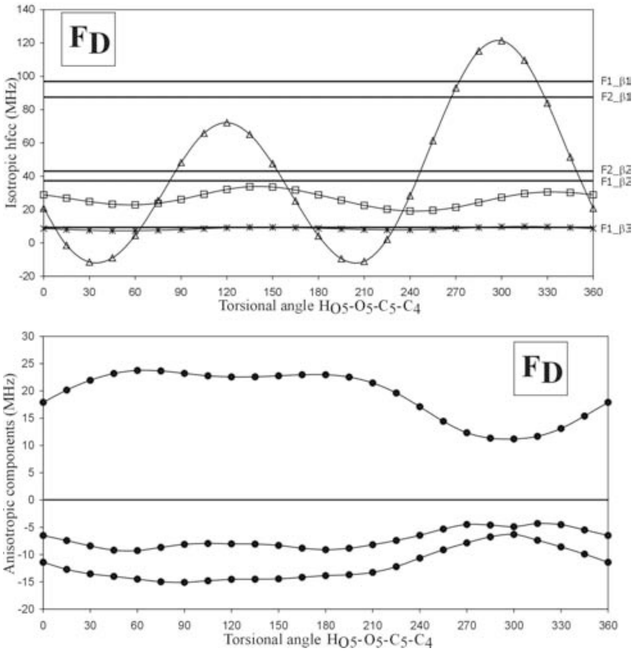

Figure 8.7: Isotropic hfcc's and H_{O5} hydroxyproton anisotropic hyperfine tensor components in model radical F_D as a function of the hydroxygroup rotation (∗ H_2; □ H_4; H_{O5}; all other proton hfcc's were close to zero throughout the rotation and are therefore not included). The experimental hfcc values are indicated by solid lines.

As was the case in F_B and F_C, the hydroxygroup rotation is the relevant degree of freedom that must be examined in the search for a conformation that suitably reproduces the experimental data. In Figure 8.7, the significant proton hfcc's are plotted as a function of the rotation of the hydroxygroup about the O_5-C_5 axis (as expressed by the torsional angle H_{O5}-O_5-C_5-C_4). Surprisingly, the H_2 proton yields a considerable hfcc of about 10 MHz throughout the hydroxygroup rotation, while the H_{1A} and H_{1B} protons do not generate substantial isotropic hfcc's. These proton couplings amount to –3 MHz at best and they were therefore not included in Figure 8.7. This is altogether quite remarkable since the H_{1A} and H_{1B} protons are in a γ-position with respect to the radical center at C_5, while the H_2 proton is in a δ-position. So, only three protons produce a significant hfcc that can be matched with the experimental values. The H_2 proton hfcc is in accordance with the F1_β3 signal throughout the plot and conformations can be found (for instance, at about 270° and 320°) where the H_{O5} proton hfcc could correspond with the β1 coupling of either F1 or F2. The H_4 proton hfcc however, fluctuates at about 25 MHz, which is quite small in comparison with the experimental F1_β2 and F2_β2 isotropic couplings (37.3

MHz and 43.10 MHz respectively). In addition, we found that the anisotropic components of the H_{O5} proton hyperfine tensor are far too large in comparison with β1. In Figure 8.7, a plot of these components is also presented as a function of the hydroxygroup torsional angle. The similarity with both charts in Figure 8.6 is obvious. As a result, no further analysis of the hyperfine tensor eigenvectors was conducted and it was concluded that model radical F_D is not consistent with the experimental results.

8.5 CONCLUSIONS

In this study single molecule DFT calculations were used to identify the structure of the radiation-induced radicals in solid-state β-D-fructose. Four tentative structures were proposed and EPR calculations were performed on the optimized geometries. In all four model radicals, the main degrees of freedom – rotation of the hydroxymethylgroup or hydroxygroup – were selectively varied and isotropic hyperfine coupling constants were recalculated at each point. From these plots, insight was gained on the conformations of which hfcc's were in possible accordance with the experimental values. Analysis of the anisotropic hyperfine tensor components for all significant protons conclusively led to the elimination of model radicals F_B, F_C and F_D. The relevant anisotropic components in model radical F_A were however in close agreement with experiment.

Subsequently, four possible F_A conformations were selected with isotropic and anisotropic hfcc's conform the experimental values of radical species F1. Based on the analysis of the tensor direction cosines of these four conformers, one structure was identified that closely matched the experimental direction cosines. The EPR parameters of this conformation, with a torsional angle O_6-C_6-C_5-C_4 of 234°, correspond quite accurately with those of the experimental F1 radical species, both for the isotropic and anisotropic hyperfine components as well as for the relative directions of the principal axes.

By comparison of the experimental information on the spatial orientation of the measured hyperfine axes between the two radical species F1 and F2, this study is not able to differentiate both and sustains the conclusion that the F1 and F2 species are in fact manifestations of the same radical, with a structure conform F_A, but with slightly altered conformations. To further assess this difference, four conformations were examined, which were in close accordance with the F2 experimental data, both for the isotropic and anisotropic hfcc's. However, due to the high sensitivity of the isotropic hydroxymethyl proton hfcc's for small changes of the O_6-C_6-C_5-C_4 torsional angle, these conformers are very close to the previous conformers associated with F1, which is not surprising. On the basis of the experimental isotropic values, only minor conformational changes are found (about 4º) which are not of that extent to further differentiate between radical species F1 and F2, based on the single molecule approach. We therefore conclude that both radical species F1 and F2, found in the experiments of Vanhaelewyn et al. [138], can be identified as having the radical structure F_A, possibly with a O_6-C_6-C_5-C_4 torsional angle at about 234°.

Since the absence of a reference axis system introduces an ambiguity in the above results, further calculations are necessary to make a clear distinction between F1 and F2 in relation to their conformations. A preliminary attempt has already been made, adopting a more advanced ONIOM cluster methodology [141]. However, even though it initially confirms the findings made in this work, still no clear differentiation between both radical species is reported possible. This is most likely connected with the occurrence of severe convergence problems in the ONIOM approach. Consequently, a periodic approach is perhaps preferable to distinguish between F1 and F2.

Chapter 9. Radiation-induced radicals in α-D-glucose

REFERENCE: [142].

9.1 BACKGROUND

The α-D-glucose crystal [143, 144] was already analysed in the early eighties by Madden & Bernhard, with a combination of EPR and ENDOR techniques. Aside from transient paramagnetic species, four stable radicals have been identified in solid-state glucose: two carbon-centered radicals (species I and II), for which both EPR and ENDOR data were obtained, and two minor oxygen-centered radicals, for which only EPR data were determined. From their experiments, structures were suggested for species I and II, based mainly on the near concurrence of some hyperfine principal directions in the radical with atom-atom directions in the undamaged glucose crystal structure. These proposed structures are represented in Figure 9.1 and correspond respectively with the RI-A and RII-C models in Figure 9.2, which will be discussed later on.

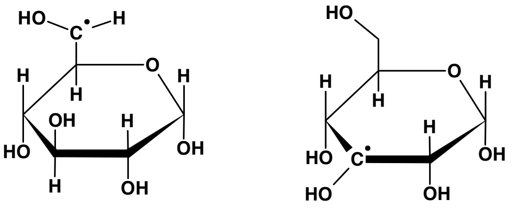

I I

Figure 9.1: Species I and II, as proposed by Madden & Bernhard.

The objective of this study is to assess the validity of these models for the carbon-centered radicals proposed by Madden and Bernhard using DFT methods. As no previous theoretical works exist on this matter, we will use – as a first step – a single molecule approach to calculate the EPR parameters for the experimentally suggested hypothetical structures. Since the required ENDOR data are available for the glucose radicals, special attention will be paid to the analysis of the principal axes for the calculated hyperfine tensors in addition to the hyperfine coupling constants.

9.2 MODEL SELECTION

The crystalline structure of α-D-glucose was obtained from a neutron diffraction study by Brown & Levy [145], which is visualized in the center of Figure 9.2. Starting from the assumption that the radiation-induced radicals in glucose are neutral and that their pyranose ring structure is not broken, several radical models can be proposed that could meet the experimental EPR and ENDOR requirements. Altogether, seven models were obtained for radical species I and five for radical species II, considering all the possible homolytic cleavages of the glucose ring substituents. They are all displayed in Figure 9.2.

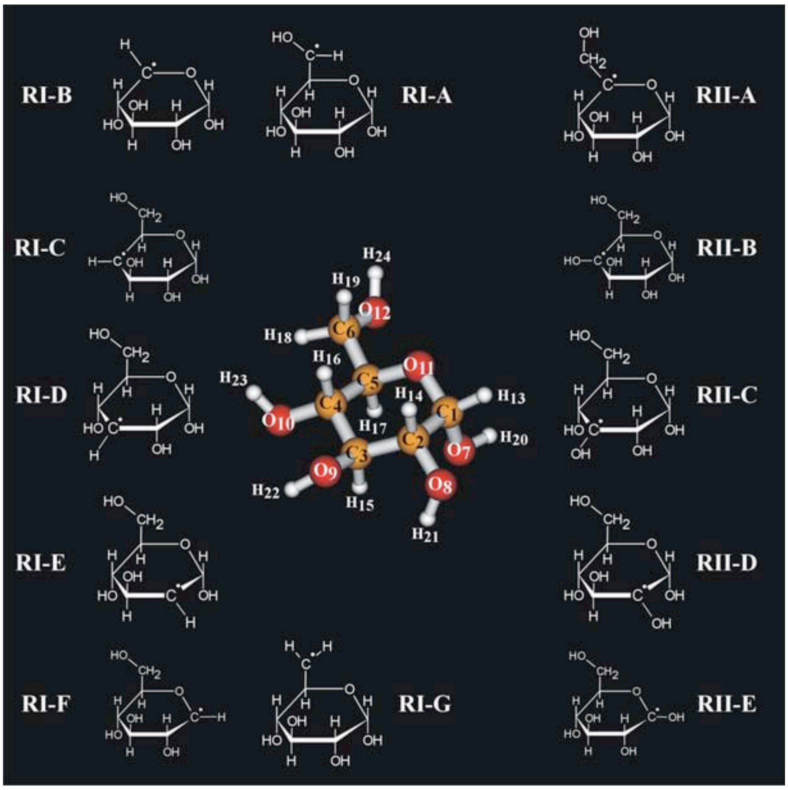

Figure 9.2: Molecular structure of crystalline α-D-glucose and all proposed model radicals.

Species I is characterised by one α-type and one β-type proton coupling besides a weak coupling attributed to a hydroxyproton. The relevant experimental data from [144] is listed in Table 9.1(a). To display a similar coupling pattern, a model radical structure must contain one proton bound directly to the carbon with an unpaired electron and (at least) one other proton further away. The most evident way to obtain such a model is to remove a single hydroxygroup. This gives rise to models RI-C, RI-D, RI-E, RI-F and RI-G, which are formed by removing an hydroxygroup from respectively C_4, C_3, C_2, C_1 and C_6. Yet, other groups or atoms can be removed to produce a model structure that meets the experimental prerequisites. If we homolytically cleave the C_5-C_6 bond, model radical RI-B results. Finally, model RI-A is obtained through simple H_{18} hydrogen abstraction from C_6.

In a similar fashion, model structures can be created with similar characteristics as the experimental **species II**. For this radical, two large β-type proton couplings have been identified and no α-type couplings. This pattern is consistent with a partial structure CH_a-$C^{\bullet}OH$-CH_b where H_a and H_b provide both β-couplings. This substructure is present in radical models RII-A through RII-D, which have been created by removing a hydrogen atom from the crystal structure on radical centers C_5 through C_2, respectively. RII-E appears to have only one β-proton, but in an earlier study [137] it was found that the unpaired electron on a carbon atom adjacent to the ring oxygen often delocalises over the oxygen. This fact makes RII-E also a valid candidate as it imparts proton H_{17} with some β character.

(a)

Signal	Aiso	Taniso	Axes vs. <oabc>		
I_α	(-)57.8	(+)-31.4	0.096	0.156	0.983
		(+)-2.2	0.974	0.190	-0.125
		(-)34.8	-0.206	0.969	-0.134
I_β	19.3	-5.7	-0.100	0.760	0.640
		-4.2	0.990	0.110	0.040
		10.0	0.040	-0.638	0.769
II_β1	95.3	-4.8	0.370	0.880	0.320
		-2.0	0.240	-0.420	0.880
		6.7	0.898	-0.240	-0.370
II_β2	89.4	-5.1	0.770	0.430	0.470
		-1.6	-0.630	0.380	0.680
		7.1	-0.120	0.815	-0.570

(b)

Partial Optimisation					
Proton	Aiso	Taniso	Axes vs. <oabc>		
RI-A H19	-32.1	36.9	-0.175	0.197	0.965
		-2.7	0.981	0.114	0.155
		-34.2	-0.079	0.974	-0.213
RI-A H17	3.5	-6.0	0.063	0.725	0.686
		-4.1	0.996	0.002	-0.093
		10.2	0.069	-0.689	0.722
RI-A H24	-12.4	-14.9	-0.1476	0.3287	0.9328
		-9.8	0.9845	-0.0417	0.1704
		24.6	0.0949	0.9435	-0.3175
RII-C H14	83.4	-4.9	0.416	0.840	0.350
		-2.4	0.297	-0.489	0.821
		7.3	0.860	-0.237	-0.452
RII-C H16	78.9	-4.9	0.695	0.543	0.472
		-3.1	-0.706	0.386	0.595
		8.0	-0.141	0.746	-0.651
Full Optimisation					
Proton	Aiso	Taniso	Axes vs. <oabc>		
RI-A H19	-30.3	35.7	-0.201	0.151	0.968
		-2.6	0.973	0.148	0.179
		-33.1	-0.116	0.977	-0.177
RI-A H17	3.3	-6.0	0.063	0.746	0.663
		-4.0	0.998	-0.036	-0.054
		10.0	0.016	-0.665	0.747
RI-A H24	-13.4	-15.4	-0.1537	0.3851	0.91
		-9.7	0.9756	-0.0871	0.2016
		25.1	0.1569	0.9188	-0.3623
RII-C H14	84.6	-4.7	0.418	0.849	0.323
		-2.4	0.181	-0.426	0.887
		7.1	0.890	-0.312	-0.332
RII-C H16	80.1	-4.8	0.690	0.523	0.500
		-3.0	-0.698	0.299	0.650
		7.8	-0.191	0.798	-0.572

Table 9.1: **(a)** review of the experimental data published in [144] **(b)** Overview of the calculated EPR parameters for radical models RI-A and RII-C. Results are given for both the "Partial Optimization" and "Full Optimization" regimes. All isotropic constants (A_{iso}) and anisotropic couplings (T_{aniso}) are given in MHz. Hyperfine principal axes are always specified as direction cosines with respect to the crystal axes <a>, <b> and <c>, respectively.

9.3 COMPUTATIONAL DETAILS

Single molecule DFT calculations were performed on these 12 models using the Gaussian 98 software package [30]. Molecular orbitals were expanded in a triple-ζ 6-311G basis augmented with single d and p polarisation functions [33] and the B3LYP functional [28] was used. Initial geometries for the radical models were obtained by removing the corresponding atoms from the glucose crystal structure. Geometry optimization calculations were then performed on the single molecules within two computational regimes. In the first, "**Partial Optimization**" scheme, only the atoms of the substituent groups that are connected with the carbon-centered radical are allowed to relax alongside with the involved carbon itself. In the case of RII-A, for instance, this means that C_5, C_6, O_{12}, H_{18}, H_{19} and H_{24} are allowed to relax, while all other atoms of the molecule are kept fixed at their original position in the crystal structure. As the unpaired electron is located on a carbon atom outside the glucose ring, an exception was made for model RI-A, where also C_5 was allowed to relax during optimization, next to C_6, O_{12}, H_{19} and H_{24}. The second, "**Full Optimization**" scheme simply imposes no restrictions on the number of atoms allowed to relax.

Subsequently, isotropic and anisotropic components of the hyperfine tensor, as well as the associated eigenvectors were calculated for the (partially) optimized structures, adopting the same level of theory. To allow for the determination of the hyperfine tensor principal directions, both (partial) geometry optimizations and EPR calculations were performed within the Fixed Axes approximation, as outlined in section 4.2.1. For glucose, this restriction specifically implies that the orientations of the different radicals are constrained to be similar to that of the undamaged sugar in the crystal. This way, the calculated tensor directions can also be evaluated with respect to crystal axes, albeit those taken from the undamaged crystal structure [145].

9.4 ASSESSMENT OF MODEL RADICAL STRUCTURES BASED ON EPR HYPERFINE PARAMETERS

In Figure 9.3, the results of the EPR calculations are summarised for all radical models. For each model, the hyperfine coupling constants (in MHz) of the relevant protons are mentioned at the top. The deviation (in degrees) of the three calculated hyperfine principal directions with the three corresponding experimental directions is schematically presented at the bottom. For the radiation-induced radicals of glucose, we have primarily concentrated on a correct reproduction of the hyperfine tensor principal axes and the deviation from their experimental counterparts. We consider the hyperfine coupling constants to be somewhat less reliable when dealing with the solid state, as the presence of a Fermi contact term in the expression of the hfcc (see section 3.6), makes this parameter very sensitive to the level of theory. The principal axes on the other hand do not depend on this term and the requirement of complicated, high-level calculations with extended basis sets (e.g. EPR-III [34]) can be eliminated.

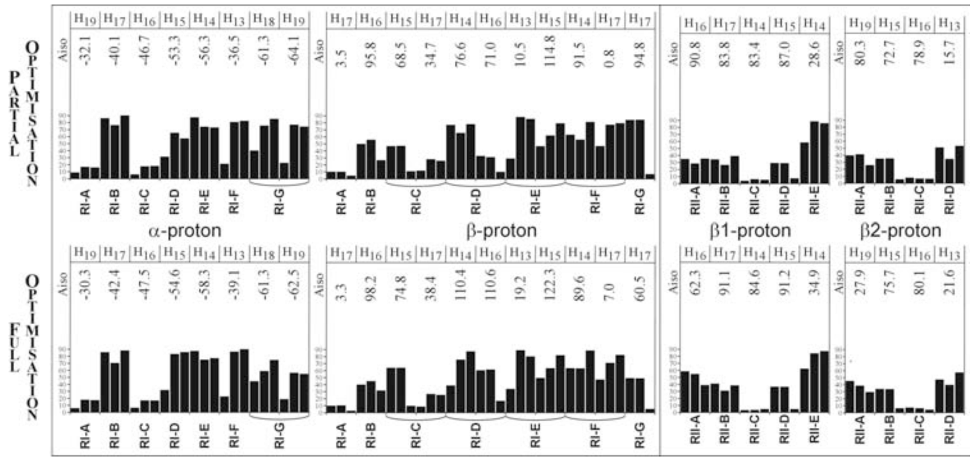

(a) **(b)**

Figure 9.3: **S**ummary of the results for the EPR calculations with reference to **(a)** radical species I and **(b)** radical species II. The deviation (in degrees) of the experimental hyperfine principal axes from the calculated ones is visualised as a black bar for each eigenvector with – from left to right – minor, intermediate and major anisotropic eigenvalue. The hfcc (in MHz) for the coupling proton involved is indicated at the top.

9.4.1 Radical species I

Taking into consideration the quality of the calculated principal directions for the "**partial optimization**" scheme, two radical models can be found for which the deviations from the experimental directions are lower than 30° for the α-proton: model RI-A characterised by one α coupling (-32.1 MHz) and one β coupling (3.5 MHz), and model RI-C with also one α coupling (-46.7 MHz), but with two β-type couplings (68.5 MHz and 34.7 MHz). All other model structures produce hyperfine principal directions that deviate more than 30° from the experimental α-proton axes. Therefore, based on these EPR properties, model structures RI-B, RI-D, RI-E and RI-G can be rejected as candidates for species I. The principal directions for H_{19} of RI-A and H_{16} of RI-C closely match those of the I_α signal, although the theoretical predictions for the hfcc's are not agreeing quite well with the experimental (-)57.8 MHz value. With respect to the I_β signal, the principal directions for H_{17} of RI-A deviate not more than 10°, while the average deviation for H_{17} in model RI-C is more than double. Also taking into account that for this latter model, one other, rather large β coupling is predicted (H_{15} with 68.5 MHz), and only one small β coupling is observed in the experiment, we come to the conclusion that model RI-C can no longer be retained. Model RI-A on the other hand is a viable candidate for species I and the agreement with experimental data is even more apparent in Table 9.1(b). Apart from the hyperfine coupling constants, most values are in close agreement with their experimental counterparts in Table 9.1(a).

The corresponding graph for the "**full optimization**" scheme in Figure 9.3(a) is almost identical to the "partial optimization" graph. Consequently, we come to the same conclusion that experimental species I can be identified as having a structure conform model I-A. No significant improvement for the hyperfine coupling constants is attained in comparison with the "partial optimization" scheme, as is apparent from Table 9.1(b).

Apparently, the reorientations of side chain groups in the "full optimization" scheme have no drastic impact on the EPR parameters of glucose. This explains the small difference between the calculated parameters in both optimization schemes.

9.4.2 Radical species II

The theoretical results are visualized in Figure 9.3(b) and it is quite obvious that only for one radical model the calculated hyperfine principal directions are in accordance with experiment. For RII-C, the deviation of all proton tensor components stays below 10°, in contrast with the other radical models, where deviations are systematically larger. This observation can be made in both the "partial optimization" and "full optimization" schemes, and is corroborated by the hyperfine coupling constants that are in good agreement with the experimental values. This conclusively gives evidence that model RII-C presents the actual structure for radical species II.

We note for this specific case the predictive power of the hyperfine tensor principal axes. In fact, if only hfcc's were considered, models RII-B and RII-D would also be viable candidates for species II. Analysis of the calculated direction cosines however unambiguously refutes these models.

9.5 CONCLUSIONS

In 1979, Madden & Bernhard [144] suggested structure RI-A for the experimental species I and structure RII-C for species II. In this work, we have confirmed these suggestions, by performing single molecule DFT calculations on several possible radical models and comparing the resulting theoretical parameters with experimental values. Conclusive support for models RI-A and RII-C was found based on the accuracy of reproducing the hyperfine principal axes rather than focussing on the exact prediction of the isotropic coupling constants. This criterium is found to be highly suitable for the validation of radical models, especially since it is not as dependent on the level of theory as the hfcc.

The case of the radiation-induced radicals of glucose smartly illustrates that single molecule calculations within a fixed axes approximation can be quite accurate for the calculation and analysis of the hyperfine principal axes. Also, given the fact that these calculations are straightforward and very fast, this method can offer a cost-effective tool for a preliminary, quick-and-easy identification or verification of organic radicals in the solid state. However, it is only applicable when radical and undamaged sugar molecule are much alike, both in structure and in overall orientation with respect to the crystal axes.

Chapter 10. Radiation-induced radicals in α-L-sorbose

REFERENCE: [146].

10.1 BACKGROUND

In a recent combined EPR, ENDOR and EI-EPR study, the paramagnetic adducts of irradiated α-L-sorbose were examined [146]. The molecular structure of this sugar is shown in Figure 10.1.

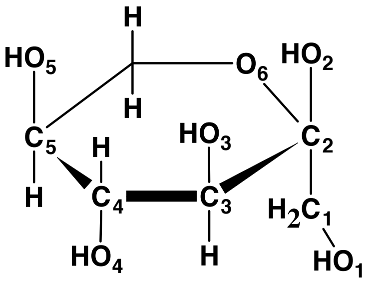

Figure 10.1: The molecular structure and numbering scheme for α-L-sorbose.

At 120 K, this system reveals a multitude of radiation-induced radicals, even though these species are of a transient nature and decay upon long time storage or upon increasing the temperature. ENDOR and EI-EPR have effectively uncovered that at least 10 stable radical species contribute to the spectra, which are consequently quite complex due to multiple signal overlap. Immediately after irradiation, a doublet was found most prominent in the spectra, and this feature was examined in more detail. ENDOR revealed that this doublet was in fact due to three very similar β-type hyperfine interactions, but it was only possible to quantitatively analyze two of the three tensors with EI-EPR. From Table 10.1, it is clear that both are very much alike with regard to couplings and tensor axes.

These interactions can be explained by either the presence of one radical species that produces both β-type couplings or by the occurrence of two (similar) radicals R1 and R1’ within the crystal matrix that account for one hyperfine interaction each. The second explanation was eventually favored, based on the combination of experimental data and DFT calculations, the latter of which are presented in this work.

	Aiso	Taniso	Eigenvectors		
			a	b	c
R1	67,1	-4,6	0,77	0,14	-0,62
		-2,4	0,55	-0,64	0,54
		7,0	0,32	0,76	0,57
R1'	70,0	-4,6	0,63	0,28	-0,73
		-2,4	0,70	-0,60	0,38
		7,0	0,33	0,75	0,57

Table 10.1: Experimental hyperfine coupling constants and direction cosines of suggested radicals R1 and R1' as determined in [146]. A_{iso}, T_{aniso} and A values are in MHz; direction cosines are referred to the *abc* reference axis system of the crystal.

10.2 MODEL SELECTION

The α-L-sorbose crystal is orthorhombic, with space group symmetry $P2_{\perp}2_{\perp}2_{\perp}$ and per unit cell (dimensions a=6.545 Å, b=18.062 Å and c=6.310 Å) four molecules occur, all in a pyranose form [147]. Crystalline disorder has been found for the orientation of the sorbose primary alcohol group between two of three possible staggered positions. Consequently, two sorbose molecular conformations A and B exist in the lattice, each exhibiting one of the two orientations for the primary alcohol (O_2-H(O_2)). This is apparent in Figure 10.2, where also the Newman projections along the C_1-C_2 bonds are given for both conformers.

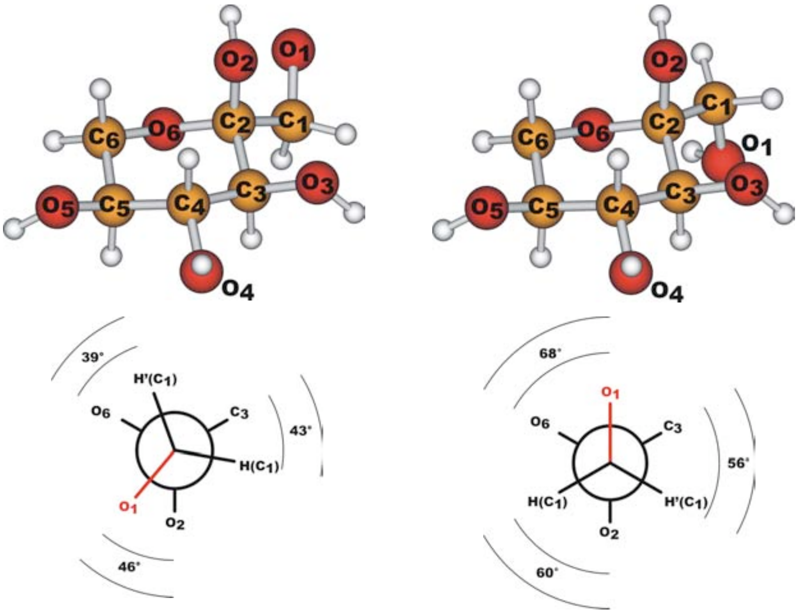

Figure 10.2: A and B conformations of the sorbopyranose molecules, illustrating the disorder in the structure (top) and Newman projections along the C_1-C_2 bond (bottom).

The occupancy of the A and B conformations in crystalline sorbose is 0.625:0.375 proportionally. This implies that two hydrogen-bonding arrangements of comparable energy are possible in the crystal.

Starting from the α-L-sorbopyranose structures in Figure 10.2, a few plausible radical models can be proposed to account for the R1 and R1' hyperfine data. Since no α-proton hyperfine couplings are observed in the measurements, only radical models that lead to β-couplings are relevant. In Figure 10.3, five such radical models are proposed, in the supposition that their pyranose ring structures remain intact. Radicals formed by hydrogen abstraction at C_3, C_4 and C_5 have been referred to as S-I, S-II and S-III, respectively. Also, the irradiation products formed by hydroxyl abstraction (model S-IV) or even by hydroxymethylgroup abstraction at C_2 (model S-V) can be considered.

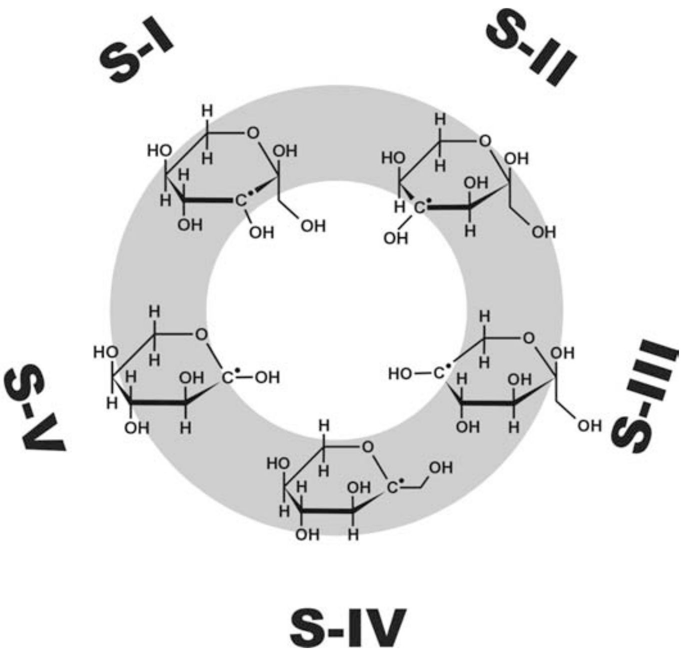

Figure 10.3: Possible radical models by net hydrogen, hydroxyl and hydroxymethylgroup abstraction from the intact sorbose molecule.

10.3 COMPUTATIONAL DETAILS

Using the Gaussian 98 software package [30], DFT calculations were performed within the single molecule approach. The B3LYP functional [28] was employed and molecular orbitals were expanded in a triple-ζ 6-311G basis augmented with single d and p polarization functions [33]. Initial geometries for the five radical models were first generated by removing the atoms involved from the sorbose crystal structure.

Geometry optimizations were then performed on these geometries using all three optimization schemes mentioned under section 4.2.1 and EPR parameters were subsequently determined at the same level-of-theory, using the fixed axes approximation. Applied to sorbose, the first “**No Optimization**” scheme implies that EPR parameters are just calculated for the initial geometries. Conversely, no geometrical restrictions whatsoever have been implied during optimization in the “**Full Optimization**” scheme. In the intermediate “**Partial Optimization**” scheme on the other hand, only the atoms of the substituent groups that are connected with the carbon-centered radical are allowed to relax alongside with the involved carbon itself.

Since two conformations A and B occur in the crystal, all stated calculations have been performed for both conformations and are labeled accordingly.

10.4 ASSESSMENT OF MODEL RADICAL STRUCTURES BASED ON EPR HYPERFINE PARAMETERS

Using the results of the “No Optimization” calculations, an initial assessment was made of the validity of the five proposed model radicals. This constitutes just the advantage of this primitive approach: to quickly examine all models in an attempt to more or less reproduce the experimental data. In table 10.2, the in this way calculated isotropic hyperfine coupling constants are presented for all relevant protons of the model radicals.

No Optimization		Aiso	
		A	**B**
S-I	H_{16}	76.8	77.5
S-II	H_{15}	70.6	75.1
	H_{17}	68.0	67.9
S-III	H_{16}	68.4	68.3
	H_{18}	80.9	80.1
	H_{19}	28.9	28.9
S-IV	H_{13}	0.0	6.3
	H_{14}	50.8	1.0
	H_{15}	64.3	69.2
S-V	H_{16}	12.8	12.8

Table 10.2: Isotropic hyperfine coupling constants (in MHz) for all model radicals, obtained through the “No Optimization” scheme.

It is clear from these “No Optimization” calculations that radical models S-III, S-IV and S-V are incompatible with the experimental observation of two similar β-type proton couplings. While S-III displays three couplings in both conformations A and B, S-IV shows only two of significant magnitude, of which, however, one is consistently too low (H_{14} for conformation A and H13 for conformation B) to measure up to the experimental 70 MHz. The same applies for S-V where only one coupling of a mere 13 MHz is predicted for both A and B conformations in the crystal.

This just leaves S-I and S-II. These radical models were a priori deemed interesting as the crystallographic C_3---H(C_4) and C_4---H(C_3) directions are quite close to the experimental eigenvectors associated with the major anisotropic components of both β-type hyperfine tensors, as illustrated in Figure 10.4. Hence, if an unpaired electron were mainly located on carbons C_3 or C_4 (as in radical models S-I and S-II), this could result in a hyperfine tensor for H(C_4) and H(C_3) in which the eigenvector corresponding to the major anisotropic component would match either of both mentioned experimentally observed eigenvectors. This, of course, will only be the case if this particular fragment of the radical geometry is nearly identical to that in the crystal structure.

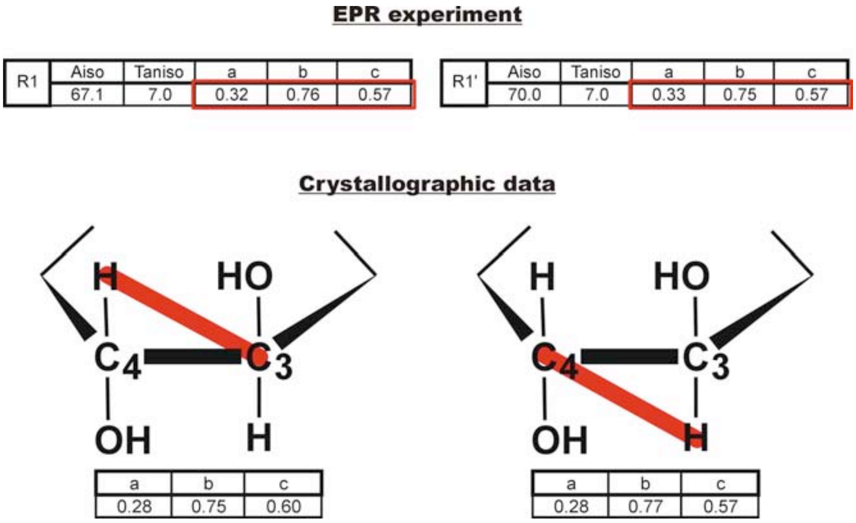

EPR experiment

R1	Aiso	Taniso	a	b	c
	67.1	7.0	0.32	0.76	0.57

R1'	Aiso	Taniso	a	b	c
	70.0	7.0	0.33	0.75	0.57

Crystallographic data

a	b	c
0.28	0.75	0.60

a	b	c
0.28	0.77	0.57

Figure 10.4: The eigenvectors corresponding to the major anisotropic components of R1 and R1’ closely resemble the crystallographic C_4-H(C_3) and C_3-H(C_4) directions, both presented as direction cosines with respect to the crystal axes.

10.4.1 Radical model S-II

For radical model S-II, all calculations predict two β-interactions with similar, large isotropic couplings in the range of 70-80 MHz. The difference between conformations A and B with regard to the calculated EPR parameters is negligible and hence we have limited this discussion to conformation A. Disregarding the experimental bias towards the occurrence of two distinct radical species, it is conceivable that the hyperfine interacting protons H(C_3) and H(C_5) might account for the measured R1 and R1' signals. In view of the similar magnitudes of both experimental and calculated hyperfine coupling constants (the latter presented in Figure 10.5(a)), two assignments can be carefully considered: H(C_3)→R1 and H(C_5)→R1', or H(C_3)→R1' and H(C_5)→R1. To verify their possible validity, the orientations of the experimental hyperfine principal axes were compared with the axes calculated within the three different optimization schemes.

In Figure 10.5(b), this deviation (in degrees) is schematically presented as a black bar for each eigenvector with – from left to right – minor, intermediate and major anisotropic eigenvalues. For all optimization schemes, an equivalent pattern can be observed. With a deviation lower than 10°, the axis corresponding to the major anisotropic component of H(C_3) is always quite close to that of either R1 or R1'. The match between the minor anisotropic component axis of H(C_5) and that of R1' is also quite good but considerably worse with R1. In spite of these moderate agreements, all other tensor axes of both H(C_3) and H(C_5) are way off their experimental counterparts with deviations up to 70°. Hence, these dramatic discrepancies imply that – regardless of any possible assignment – model S-II must be ruled out as a viable candidate for the radiation-induced radical in sorbose. Consequently, the potential presence of one radical species that would account for both observed β-couplings can also be indisputably rejected, in accordance with the experimental postulation.

(a)

Aiso		
$H(C_3)$	$H(C_5)$	Optimization
70.6	68.0	No
78.4	74.3	Partial
82.2	81.4	Full

(b)

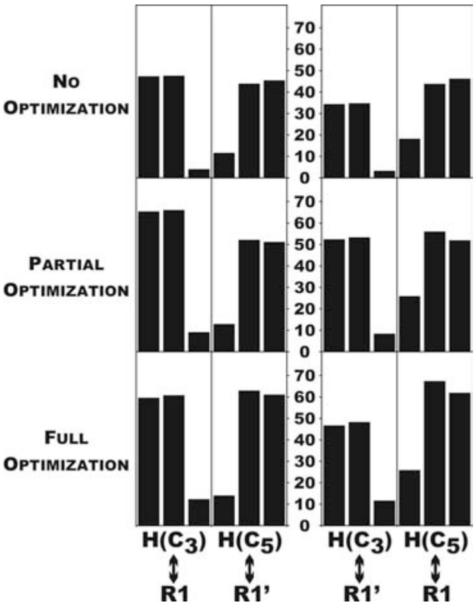

Figure 10.5: (**a**) Summary of the hyperfine coupling constants (in MHz) for model radical S-II obtrained with all optimization schemes. (**b**) Schematic of the deviation (in degrees) between the experimental and predited hyperfine principal axes, presented for the two possible assignments.

10.4.2 Radical model S-I

As Table 10.2 substantiates for the "No Optimization" scheme, both the A and B conformations of S-I are characterized by a single, relatively large β-coupling which can be assigned to either R1 or R1'. Given that the similarity of the experimental hyperfine tensors suggests the occurrence of two comparable radical species, it could be further hypothesized that their near identical structures are associated with the conformational disorder in the sorbose crystal. Such a link between the R1 and R1' radical species and the A and B crystal conformations would also be detectable, since the intensity ratio of the experimental spectra should then correspond to about 0.625:0.375. Unfortunately, the ENDOR intensity ratio could not be reliably determined, and this possibility can hence only be evaluated by way of molecular modeling.

Accordingly, the hyperfine coupling constants as well as the principal tensor directions for the A and B conformations of S-I were cross-referenced with the measured data of either R1 and R1', as represented in Figure 10.6. For all optimization schemes, the calculated isotropic couplings are given at the top for conformation A and at the bottom for conformation B. Conform Figure 10.5(b), the deviation (in degrees) between experimental and predicted principal axes is schematically presented as a black bar for each eigenvector with – from left to right – minor, intermediate and major anisotropic eigenvalues.

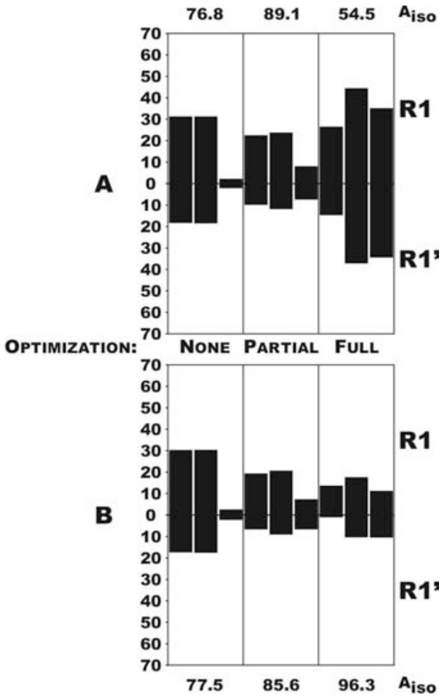

Figure 10.6: Summary of the results for the EPR calculations with reference to radical model S-I. Calculated hyperfine principal axes are cross-referenced with the experimental axes from either R1 and R1'. The deviation (in degrees) is visualised as a black bar for each eigenvector. The hfcc's (in MHz) for the H_3 proton in both conformations are indicated at the top and bottom.

The EPR parameters of the **not optimized** structure are already in quite good agreement with experiment. Not only are the coupling constants (76.8 MHz and 77.5 MHz) very close to those of R1 and R1', there is an extremely good match between the experimental principal axis with major eigenvalue and the calculated axis direction. The latter agreement is of course due to the near coincidence of the $H(C_4)$-C_3 direction in the crystal with the concerned R1 or R1' eigenvectors, as argued earlier. For both the A and B conformers, a better overall correspondence is obtained with the R1' experimental data, for which all axis deviations are well below 20°.

This accordance in particular is even improved in the **partially optimized** structure, where calculated and experimental axes now scarcely deviate 10° at most. The predicted isotropic coupling constants, on the other hand, gravely exceed the experimental 67-70 MHz. This can mainly be attributed to the conformational changes the radical geometry has undergone during (partial) optimization. In both A and B, the C_3-C_2-C_4-O_3 improper torsional angle – which can be considered as a measure for the planarity of the C_3 carbon atom – is reduced from 33.5° in the crystal to about 19°. This clearly shows that the atom on which the unpaired electron is mainly located – while still far from planar – already indicates some sp^2 character. Consequently, it can be expected that the spin density in the LEO, the "Lone Electron Orbital" virtually perpendicular to the C_2-C_4-O_3 plane and containing the unpaired electron for the most part, is increased in the "Partial Optimization" structure as compared to that of the "No Optimization" scheme. This effect can explain the enlarged isotropic couplings, through the relation specified in Chapter 3 for β-coupling protons. Again, the experimental data of R1' best fit the calculated results of both the A and B conformers, with axis deviations not surpassing 10°.

In the **fully optimized** A and B structures, the planarity of the C_3 center is further enhanced with C_3-C_2-C_4-O_3 angles of 12.3° and 10.7°, respectively. Yet, only for the B conformation, a matching increase in the hyperfine coupling constant is apparent. The absence of such an increment in the case of A is the result of a drastic structural alteration, which is apparent in Figure 10.7, where the latter conformation is visibly distorted from the partially optimized structure (also presented). This change is brought about by the formation of an intramolecular hydrogen bond between $H(O_3)$ and O_2, which transforms the original chair conformation of the pyranose ring into an envelope conformation. Such an interaction would of course hardly occur within the solid state, where intermolecular hydrogen bonds retain a firm grasp on the orientations of the side chains. The obvious failure of the "Full Optimization" scheme in this particular case is further indicated by the deviation between the experimental and theoretical hyperfine tensor axes: differences of more than 40° are recorded. For B, on the other hand, the optimization scheme is successful but no major changes are observed for the axes with respect to the "Partial Optimization" structure.

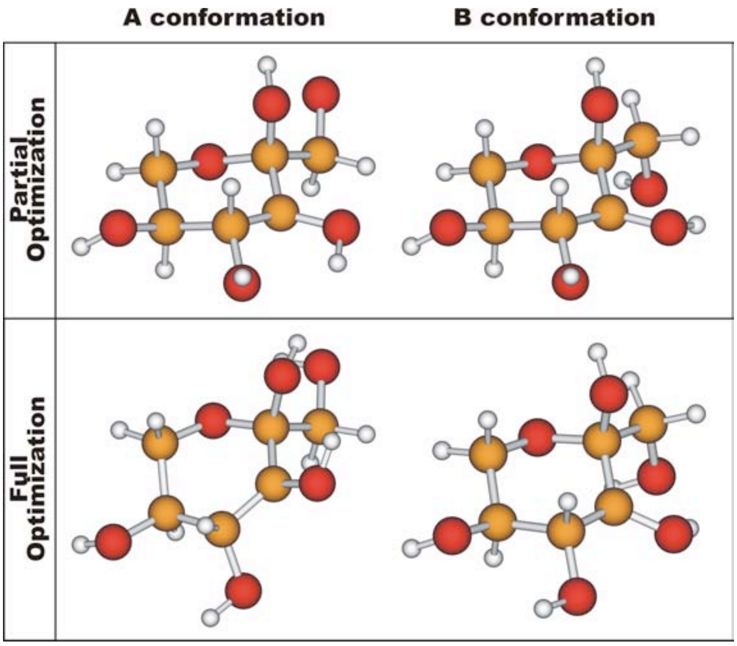

Figure 10.7: Geometry of the A and B radical conformations after "Partial Optimization" and "Full Optimization".

In conclusion, it is clear that radical model S-I can account for the experimentally observed radiation-induced radicals in α-L-sorbose. Since all calculations on the A and B conformations yield EPR parameters that are in slightly better agreement with R1' than with R1, a direct link between the conformational disorder in the crystal and the two measured hyperfine interactions is not very likely. Instead, it is more probable that the distinction between R1 and R1' is caused by the close association of the radical with one or more neighboring molecules within the crystal lattice. This association can be covalent in nature (i.e. bond rearrangements between radical and molecule(s)), but is more likely due to altered hydrogen bonds or Van der Waals interactions.

Under the assumption that a connection could occur between the radical and only one molecule of the crystal lattice, four possible radical-molecule pairs (A-A, A-B, B-A and B-B) can be considered. Their occurrence is a mere result of the crystal disorder, which is present throughout the lattice. Hence, not only the radical species can take on either A or B crystal conformations, but also the molecule(s) of the crystal surrounding. Taking into account the A:B ratio of occupancy in the crystal (see above), the probabilities for the occurrence of the radical-molecule pairs can be easily derived: 0.391% for A-A, 0.234% for A-B and B-A, and 0.141% for B-B. As the radical structures in these four pairs can be assumed to show minute differences, four distinct hyperfine interactions can be expected. Such an interpretation may explain the initial experimental observation of more than two β-interactions in the ENDOR spectra: the A-A, A-B and B-A pairs can account for the three observed β-couplings, while the B-B pair is likely to remain undetected due to its lower probability.

However, it must be emphasized that such an argumentation is completely hypothetical and must be thoroughly checked. More advanced calculations on this matter are duly necessary, in which the model space will be extended to include at least some molecules of the crystal environment. Cluster or periodic calculations are the obvious choice, since they are highly suitable to take into account the complex hydrogen-bonding network of the sorbose crystal (Figure 10.8). Hence, these methods are likely to provide a better insight into the possible association of the radical with one or more molecules of the crystal lattice.

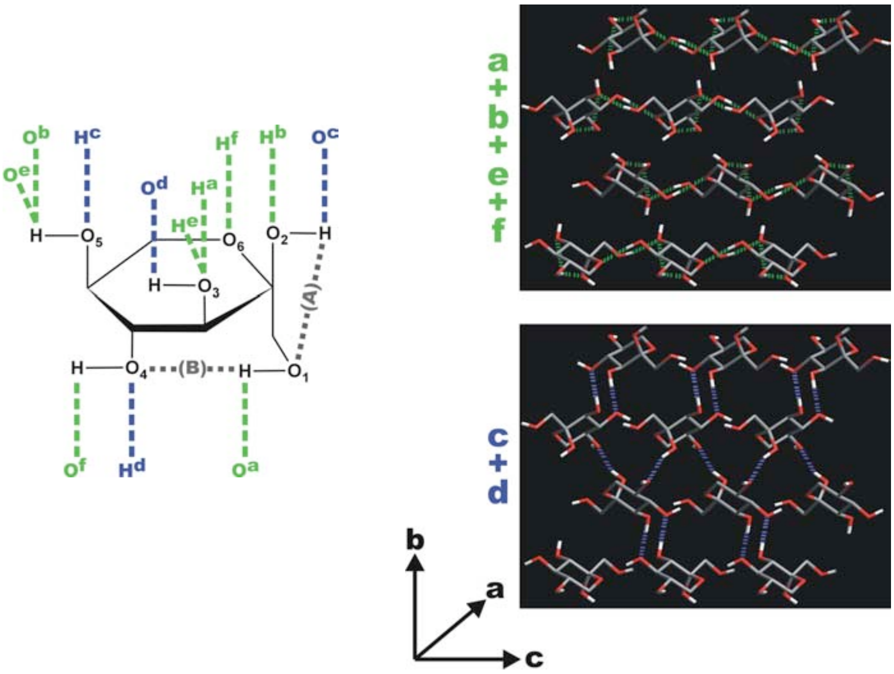

Figure 10. 8: Six types of hydrogen bond interactions occur in crystalline α-L-sorbose. Interactions a, b, e and f generate layers within the lattice, perpendicular to the b axis. These are held together by the “infinite hydrogen bonding scheme” of interactions c and d [147].

10.5 CONCLUSIONS

Using single molecule DFT calculations on several possible radical models, the identity of one of the radiation-induced radicals in α-L-sorbose was established. Both theory and experiment accord on the existence of two separate radicals in the sorbose crystal lattice, with identical structures but with slightly different conformations. The observed R1 and R1’ species were thus assigned a structure conform radical model S-I. Although the specific conformational difference was not addressed, it is assumed that this is related to the occurrence of crystal disorder in solid-state α-L-sorbose. Hence, the theoretically predicted EPR parameters of a radical with either conformation A or B were compared with the R1 and R1’ spectroscopic data, and were consistently found in slightly better agreement with the latter. As this rules out a direct link between the crystal disorder and the radical site, it is likely that the R1-R1’ difference is due to the association of one or more A/B molecules of the crystal lattice with the radical site. However, modeling techniques with a larger model space will be required to assess the validity of that assumption.

The single molecule calculations on sorbose radicals once more confirm their validity and usefulness to reproduce the experimental EPR parameters to a certain degree of accuracy. Even the simplest “No Optimization” scheme can render results that are valuable. Still, great care should be taken in the selection and execution of an optimization scheme, as illustrated by the failure of the “Full Optimization” scheme for conformation A of S-I.

Chapter 11. General conclusions

In this work, we have given an overview of how computational methods can help to reveal the identity of radiation-induced radicals in organic crystals. We have specifically focused on two types of molecular systems: sugars and amino acids. Both types of biomolecules have diverse applications and their associated radicals have an equal importance in biochemistry. In addition, several industrial applications exist that rely on these paramagnetic systems, especially when they occur within a solid-state crystal lattice.

Whereas these radical species are usually studied with the aid of Electron Paramagnetic Resonance experiments, we have adopted a reverse methodology and calculated the EPR spectroscopic parameters on theoretical grounds. To this end, a **general strategy** was first stipulated that allows a good description of the radical geometry and its associated spectroscopic characteristics. This methodology – consisting of the four successive steps “radical model selection”, “geometry optimization”, “EPR calculation” and “analysis” – relies mainly on ab-initio Density Functional calculations.

This strategy was applied to examine the radiation-induced radicals in five solid-state molecular systems: two amino acids (L-α-alanine and α-glycine) and three carbohydrates (β-D-fructose, α-D-glucose and α-L-sorbose). In the treatment of these systems, special attention was paid to the construction and extent of the model space. The latter refers to the ensemble of the radical and the part of its solid-state environment that is explicitly accounted for in the calculations. It was established in this work that the treatment of this model space has a significant impact on the accuracy of both the optimized radical geometry and its associated EPR parameters and, accordingly, must be carefully considered in a computational study of radicals in the solid state. Three main model space approaches were introduced, differing by the size and level of theory treatment of the model space. In a **“single molecule” approach**, the solid-state environment of the radical is completely neglected, as only the latter paramagnetic molecule is considered. In a **“cluster“ approach**, an explicit part of the crystal lattice is taken up in the model space, by placing discrete molecules around the target radical. Finally, the full periodicity of the entire crystal is accounted for in the **“periodic” approach**, in which the radical defect is embedded in an artificially enlarged unit cell.

Several issues must be carefully resolved in each model space approach with regard to the “geometry optimization” step. In the single molecule approach a suitable optimization scheme (No-, Partial- or Full Optimization) must be selected to overcome the lack of a crystalline environment. A cluster calculation not only requires the choice of a suitable level of theory (semi-empirical, hybrid or full ab-initio) but also a physically relevant selection criterion for determining the cluster size. Such an arbitrary choice is not necessary in a periodic treatment, but care must be taken that the radical is embedded in large enough a supercell so that the mutual interactions between the paramagnetic defects can be neglected.

After the geometry optimization step, the EPR calculations may be tackled. Although two main types of spectroscopic EPR parameters are usually obtained from experimental studies, we have concentrated on a theoretical reproduction of the complete hyperfine tensor, because the g-tensor for the considered amino acids and sugars is always found to be nearly isotropic and close to the free electron value. Consequently, only the former parameter presents a sensitive probe. Even though most theoretical studies in literature concentrate mainly on a correct reproduction of the isotropic hyperfine coupling constants, in this work the eigenvalues and principal axes of the anisotropic hyperfine tensors often proved an additional informative parameter for an accurate identification of radical structures. However, the model space also plays an important role in the calculation of these EPR parameters and this concept is seldomly considered in literature. Intermolecular interactions will have an influence both on the isotropic coupling constants as well as on the orientations of the principal axes for a hyperfine tensor. Such effects can – at least for now – only be revealed by performing EPR calculations within a cluster approach, because the calculation of spectroscopic properties is not yet implemented in any periodic code. Single molecule EPR calculations, on the other hand, present a fast and easy alternative from the computational point of view. Only when the optimized radical geometry was obtained from an earlier single molecule optimization, a problem arises, since no information is available on the crystal axes, to which the hyperfine tensor directions are referenced. This can be bypassed by either analyzing these tensor directions with respect to each other, in a "relative" approach, or by maintaining the original reference frame from the undamaged crystal in a "Fixed Axes" approximation. Although the latter method is not as generally applicable as the former – the approximation is in fact only valid when the radical is very much alike the undamaged molecule in the crystal – it allows for a much easier analysis.

Both amino acids and sugars exhibit in the solid state a dense hydrogen bond network within their crystal lattice. As a result, the geometry and spectroscopic properties of an induced radical will be largely determined by these hydrogen bonds and it could be suggested that a similar computational approach should apply to both systems. However, amino acids differ significantly from sugars in the sense that they adopt a zwitterionic form in the solid state. The former systems are therefore rather delicate, since spin and charge polarization effects will be much more important for these partially charged species. Also, they will be more sensitive to the extent of the model space and the level of theory. Further taking into account that amino acids have been extensively characterized and are well documented, we have first examined the alanine and glycine systems, with the additional aim of validating the different model space approaches. For both amino acids, the more advanced methods – cluster- and periodic approaches – proved preferable for a good description of the radical geometry and its EPR parameters. This way, the sometimes artificial adjustments in the single molecule approach, such as intramolecular restraints and rotations or solvent models to keep the radical in its zwitterionic form, can also be avoided. Yet, the preferred methods still have shortcomings. The periodic approach, for one, utterly failed to correctly describe the weak intermolecular forces in the glycine crystal lattice. This failure is probably related to the fact that hybrid (hyper-GGA) functionals are not generally implemented in periodic software packages. Although progress may be expected in the near future, for the time being, this model space approach is unsuitable to handle the glycine system. Cluster methods, on the other hand, often suffer from convergence problems, which make it difficult to obtain a geometry that corresponds to the absolute minimum on the energy hypersurface of the radical within its cluster environment. Nevertheless, using either method, we were able to refine existing structural information for the radical models of alanine and glycine. In this respect, the observation of a non-planar radical backbone in both amino acids is remarkable and points to the existence of vibrational and/or temperature effects in these lattices, as argued in Chapters 5 and 6.

Carbohydrate crystals are basically held together by hydrogen bonds, but the individual sugar molecules also occur in a neutral form in vacuum. Due to absence of complicating structural features, such as a zwitterionic form, and bearing in mind that sugars require more computational resources than amino acids, only single molecule calculations have been performed for these species. However, even such a fairly simple model space approach rendered good qualitative results for the geometry and EPR parameters of the radiation-induced sugar radicals. In the case of the glucose radicals, the agreement between experiment and calculation was even quantitatively very good. Contrary to the work on amino acids, the main goal in the study of sugar systems was not a validation of a proposed methodology, but rather the identification and verification of radical structures that were proposed from the experiment. For this purpose, a single molecule approach turns out more than sufficient. In the study of the radiation-induced radicals in β-D-fructose and α-D-glucose, the model structures previously proposed by experimentalists were properly verified. Moreover, for α-L-sorbose, a completely new radical structure was put forward, as the result of a successful synergy between theory and experiment.

The “Fixed Axes” approximation within the single molecule approach proved valid in the case of glucose and sorbose. This indicates that each of these sugar radicals closely resembles the undamaged molecular structure in the crystal. For fructose, in contrast, this assumption was not applicable and a relative treatment of the anisotropic hyperfine tensor axes was required. This distinction is clearly related to the location of the unpaired electron in the pyranose ring of the sugar involved. Whereas for glucose and sorbose, the paramagnetic electron is primarily located on a framework carbon center of the six-membered ring, it is situated on a side-chain carbon for fructose. The side-chain in the latter system evidently has much more degrees of freedom while the former two sugar radicals are rather restricted in their conformation. This is corroborated by the success of the “Partial Optimization” scheme and – to a lesser degree – of the “No Optimization” routine in these cases.

A remarkably similar conclusion is obtained for two sugars: both the F1 and F2 radicals in fructose and the R1 and R1’ species in sorbose are identified as having an identical structure, but with slightly different conformations. Yet, the single molecule approach proved inadequate to address this conformational difference. For sorbose the distinction between R1 and R1’ was hypothetically attributed to the association of the radical site with one or more intact molecules of the surrounding. Due to the crystal disorder in the sorbose crystal, such a connection could potentially result in different “associated” radical sites to be observed. But in the fructose lattice, no such crystal disorder has been observed so far. If now the foundation for the occurrence of similar radicals is the same in fructose and sorbose, it must be concluded that either the hypothesis postulated for sorbose is false, or else that crystal disorder nevertheless must occur in the fructose crystal. These speculations must however be verified with calculations in a more advanced model space approach.

It might be expected that the different methodologies and model space approaches outlined in this work are suitable for the study of other organic radicals in the solid state, and perhaps even in solutions, where intermolecular interactions are also present in abundance. Hence, they present a powerful tool, complementary to the EPR experiment, because the true identity of an experimentally observed paramagnetic species can be linked directly to the structural characteristics of a proposed theoretical model. Still, it is not easy to propose a generally applicable methodology, since this would depend to a large extent on the nature of the molecular system concerned. Probably the most efficient way is to start out with a single molecule approach (perhaps even using the “No Optimization” scheme) and gradually adopting more complicated model space approaches, depending on the desired accuracy for the structural or spectroscopic data.

Bibliography

[1] Szabo, A.; Ostlund, N. S. in "*Modern Quantum Chemistry: Introduction to Advanced Electronic Structure Theory*", McGraw-Hill, **1989**.

[2] Waroquier, M. in "*Kwantumtheorie van de chemische binding (Moleculaire Modellering)*", Keuzecursus voor licentie natuurkunde, Universiteit Gent.

[3] Levine, I. N. "*Quantum Chemistry*", Prentice Hall, New Jersey, **1991**.

[4] Koch, W.; Holthausen, M. C. "*A Chemist's Guide to Density Functional Theory*", second edition, Wiley-VCH Verlag, **2001**.

[5] Weiner, S. J.; Kollman, P. A.; Case, D. A.; Singh, U. C.; Ghio, C.; Alagona, G.; Profeta, S.; Weiner, P. *J. Am. Chem. Soc.* **1984**, *106*, 765.
Cornell, W. D.; Cieplak, P.; Bayly, C. I.; Gould, I. R.; Merz, K. M. Ferguson, D. M.; Spellmeyer, D. C.; Fox, T.; Caldwell, J. W.; Kollman, P. A. *J. Am. Chem. Soc.* **1995**, *117*, 5179.

[6] Allinger, N. L. *J. Am. Chem. Soc.* **1977**, *99*, 8127.
Allinger, N. L.; Yuh, Y. H.; Lii, J. J. *J. Am. Chem. Soc.* **1989**, *111*, 8551.

[7] Barone, V. ; Capecchi, G. ; Brunel, Y.; Andries, M. D.; Subra, R. *J. Comput. Chem.* **1997**, *18*, 1720.

[8] Perdew, J. P. in "*Density Functional Theory: A bridge between Chemistry and Physics*", Ed. P. Geerlings, F. De Proft, W. Langenaker, VUB University Press, **1998**.

[9] Van Speybroeck, V. "*Density Functional Theory versus Hartree-Fock in Moleculaire Systemen*", master thesis **1996-1997**, unpublished.

[10] Van Speybroeck, V. "*Ab-initio static and dynamic molecular methods: A useful tool in the study of chemical reactions*", PhD thesis **2001-2002**, unpublished.

[11] Peirs, K. "*Ab initio Study of Density Functional Theory from the Perspective of the Green's Function Fromalism*", PhD thesis **2002-2003**, unpublished.

[12] Hemelsoet, K. "*Theoretische studie van reactiviteitsindices binnen het DFT formalisme*", master thesis **2001-2002**, unpublished.

[13] Parr, R. G.; Yang, W. "*Density-Functional Theory of Atoms and Molecules*", Ed. R. Breslow, J. B. Goodenough, J. Halpern, J. S. Rowlinson, Oxford University Press, New York, **1989**.

[14] Fermi, E. *Rend. Accad. Lincei* **1927**, *6*, 602.
Thomas, L. H. *Proc. Camb. Phil. Soc.* **1927**, *23*, 542.

[15] Hohenberg, P. ; Kohn, W. *Phys. Rev. B* **1964**, *136*, 864.

[16] Kohn, W.; Sham, C. J. *Phys. Rev. A* **1965**, *140*, 1133.

[17] Perdew, J. P. lecture at "*10th International Conference on the Applications of Density Functional Theory in Chemistry and Physics*", **2003**.

[18] Perdew, J. P.; Schmidt, K. in "*Density Functional Theory and its Applications to Materials*", Ed. V. E. VanDoren, K. Van Alsenoy, P. Geerlings, American institure of Physics.

[19] Vosko, S. J.; Wilk, L.; Nusair, M. *Can. J. Phys.* **1980**, *58*, 1200.

[20] Perdew, J. P. in "*Electronic Structure of Solids*", Ed. P. Ziesche and H. Eschrig, Akademie Verlag, Berlin, **1991**.
Burke, K.; Perdew, J. P.; Wang, Y. in "*Electronic Density Functional Theory. Recent Progress and New Directions*", Ed. J. F. Dobson and G. Vignale, Das MP Plenum Press, New York, **1998**.

[21] Becke, A. D. *Phys. Rev. A* **1988**, *38*, 3098.

[22] Lee, C. T.; Yang, W. T.; Parr, R. G. *Phys. Rev. B* **1988**, *37*, 785.
Miehlich, B.; Savin, A.; Stoll, H.; Preuss, H. *Chem. Phys. Lett.* **1989**, *157*, 200.

[23] Perdew, J. P.; Zunger, A. *Phys. Rev. B* **1981**, *23*, 5048.

[24] Perdew, J. P. *Phys. Rev. B* **1986**, *33*, 8822.

[25] Becke, A. D. *J. Chem. Phys.* **1992**, *96*, 2155.

[26] Perdew, J. P.; Burke, K.; Ernzerhof, M. *Phys. Rev. Lett.* **1996**, *77*, 3865.
Perdew, J. P.; Burke, K.; Ernzerhof, M. *Phys. Rev. Lett.* **1997**, *78*, 1396.

[27] Staroverov, V. N.; Scuseria, G. E.; Tao, J. M.; Perdew, J. P. *J. Chem. Phys.* **2003**, *119*, 12129.

[28] Becke, A. D. *J. Chem. Phys.* **1996**, *104*, 1040.

[29] ADF 1999
Baerends, E. J.; Ellis, D. E.; Ros, P. *Chem. Phys.* **1973**, *2*, 41.
Versluis, L.; Ziegler, T. *J. Chem. Phys.* **1988**, *88*, 322.
te Velde, G.; Baerends, E. J. *J. Comput. Phys.* **1992**, *99*, 84.
Guerra, F. C.; Snijders, J. G.; te Velde, G.; Baerends, E. J. *Theor. Chem. Acc.* **1998**, *99*, 391.

[30] Gaussian 98, Revision A.7, M. J. Frisch, G. W. Trucks, H. B. Schlegel, G. E. Scuseria, M. A. Robb, J. R. Cheeseman, V. G. Zakrzewski, J. A. Montgomery, Jr., R. E. Stratmann, J. C. Burant, S. Dapprich, J. M. Millam, A. D. Daniels, K. N. Kudin, M. C. Strain, O. Farkas, J. Tomasi, V. Barone, M. Cossi, R. Cammi, B. Mennucci, C. Pomelli, C. Adamo, S. Clifford, J. Ochterski, G. A. Petersson, P. Y. Ayala, Q. Cui,K. Morokuma, D. K. Malick, A. D. Rabuck, K. Raghavachari, J. B. Foresman, J. Cioslowski, J. V. Ortiz, A. G. Baboul, B. B. Stefanov, G. Liu, A. Liashenko, P. Piskorz, I. Komaromi, R. Gomperts, R. L. Martin, D. J. Fox, T. Keith, M. A. Al-Laham, C. Y. Peng, A. Nanayakkara, C. Gonzalez, M. Challacombe, P. M. W. Gill,

B. Johnson, W. Chen, M. W. Wong, J. L. Andres, C. Gonzalez, M. Head-Gordon, E. S. Replogle, and J. A. Pople, Gaussian, Inc., Pittsburgh PA, **1998**.

[31] Gaussian 03, Revision B.03, Frisch, M. J.; Trucks, G. W.; Schlegel, H. B.; Scuseria, G. E.; Robb, M. A.; Cheeseman, J. R.; Montgomery Jr., J. A.; Vreven, T.; Kudin, K. N.; Burant, J. C.; Millam, J. M.; Iyengar, S. S.; Tomasi, J.; Barone, V.; Mennucci, B.; Cossi, M.; Scalmani, G.; Rega, N.; Petersson, G. A.; Nakatsuji, H.; Hada, M.; Ehara, M.; Toyota, K.; Fukuda, R.; Hasegawa, J.; Ishida, M.; Nakajima, T.; Honda, Y.; Kitao, O.; Nakai, H.; Klene, M.; Li, X.; Knox, J. E.; Hratchian, H. P.; Cross, J. B.; Adamo, C.; Jaramillo, J.; Gomperts, R.; Stratmann, R. E.; Yazyev, O.; Austin, A. J.; Cammi, R.; Pomelli, C.; Ochterski, J. W.; Ayala, P. Y.; Morokuma, K.; Voth, G. A.; Salvador, P.; Dannenberg, J. J.; Zakrzewski, V. G.; Dapprich, S.; Daniels, A. D.; Strain, M. C.; Farkas, O.; Malick, D. K.; Rabuck, A. D.; Raghavachari, K.; Foresman, J. B.; Ortiz, J. V.; Cui, Q.; Baboul, A. G.; Clifford, S.; Cioslowski, J.; Stefanov, B. B.; Liu, G.; Liashenko, A.; Piskorz, P.; Komaromi, I.; Martin, R. L.; Fox, D. J.; Keith, T.; Al-Laham, M. A.; Peng, C. Y.; Chen, W.; Wong, M. W.; Gonzalez, C.; Pople, J. A., Gaussian, Inc., Pittsburgh PA, **2003**.

[32] Hariharan, P. C.; Pople, J. A. *Theor. Chim. Acta* **1973**, *28*, 213.
Francl, M. M.; Pietro, W. J.; Hehre, W. J.; Binkley, J. S.; Gordon, M. S.; DeFrees, D. J.; Pople, J. A. *J. Chem. Phys.* **1982**, *77*, 3654.

[33] Krishnan, R.; Binkley, J. S.; Seeger, R.; Pople, J. A. *J. Chem. Phys.* **1980**, *72*, 650.
McLean, A. D.; Chandler, G. S. *J. Chem. Phys.* **1980**, 72, 5639.

[34] Barone, V. in "*Recent Advances in Density Functional Methods, Part I*"; Chong, D. P., Ed.; World Scientific Publishing Co.: Singapore, **1995**; Chapter 8.

[35] Dewar, M. J. S.; Zoebisch, E. G.; Healy, E. F.; Stewart, J. J. P. *J. Am. Chem. Soc.* **1985**, *107*, 3902.

[36] Stewart, J. J. P. *J. Comput. Chem.* **1989**, *10*, 209.
Stewart, J. J. P. *J. Comput. Chem.* **1989**, *10*, 221.

[37] Leach, A. R. in "*Molecular Modeling, principles and applications*", Addison Wesley Longman Limited, **1996**.

[38] Atherton, N. M. in "*Principles of Electron Spin resonance*", Ellis Horwood, Prentice Hall, **1993**.

[39] Box, H. C. in "*Radiation Effects: ESR and ENDOR Analysis*", Academic Press, London, **1977**.

[40] Gordy, W. in "*Theory and Applications of Electron Spin Resonance*", Ed. A. Weissberger, Wiley, New York, **1980**.

[41] Weil, J. A.; Bolton, J. R.; Wertz, J. E. in "*Electron Paramagnetic Resonance: Elementary Theory and Practical Applications*", Wiley, New York, **1994**.

[42] Malkin, V. G.; Malkina, O. L.; Eriksson, L. A.; Salahub, D. R. in "*Modern Density Functional Theory: A Tool for Chemistry*", Ed. J. M. Seminario and P. Politzer, Elsevier, **1995**.

[43] Zavoisky, E. *J. Phys. U. S. S. R.* **1945**, *9*, 211.

[44] Gerlach, W.; Stern, O. *Z. Phys.* **1921**, *8*, 110.

[45] Uhlenbeck, G. E.; Goudsmit, S. *Naturwissenschaften* **1925**, *13*, 953.

[46] McWeeny, R. in "*Methods of Molecular Quantum Mechanics*", Academic Press, **1989**, Chapter 11.

[47] Levitt, M. H. in "*Spin dynamics: Basics of Nuclear Magnetic Resonance*", Wiley, **2001**.

[48] Vanhaelewyn, G. "*Fundamental magnetic resonance study of materials relevant for EPR applications (dosimetry, dating, food irradiation)*", PhD thesis **2000-2001**, unpublished.

[49] Bersohn, R. *J. Chem. Phys.* **1956**, *24*, 1066.
Jarrett, H. S. *J. Chem. Phys.* **1956**, *25*, 1289.
McConnell, H. M. *J. Chem. Phys.* **1956**, *24*, 764.
Weissman, S. I. *J. Chem. Phys.* **1956**, *25*, 890.

[50] Petrenko, T. L. J. Phys. Chem. A 2002, 106, 149.

[51] For example:
Gauld, J. W.; Eriksson, L. A.; Radom, L. *J. Phys. Chem. A* **1997**, *101*, 1352.
Adamo, C.; Cossi, M.; Barone, V. *J. Mol. Struct. (THEOCHEM)* **1999**, *493*, 145.
Batra, R.; Giese, B.; Spichty, M.; Gescheidt, G.; Houk, K. N. *J. Phys. Chem.* **1996**, *100*, 18371.

[52] Eriksson, L. A.; Wang, J.; Boyd, R. J. *Chem. Phys. Lett.* **1993**, *211*, 88.
Zhu, W.; Jiang, H.; Gu, J.; Chen, J.; Shen, J.; Chen, K.; Ji, R.; Cao, Y. *J. Mol. Struct. (THEOCHEM)* **1999**, *488*, 21.
Ban, F. Q.; Gauld, J. W.; Boyd, R. J. *J. Phys. Chem. A* **2000**, *104*, 8583.
Lahorte, P.; De Proft, F.; Callens, F.; Geerlings, P.; Mondelaers, W. *J. Phys. Chem. A* **1999**, *103*, 11130.

[53] Almlöf, J.; Wahlgren, U. *Theor. Chim. Acta* **1973**, *28*, 161.
Zyss, J.; Berhier, G. *J. Chem. Phys.* **1982**, *77*, 3635.
Krijn, M. P. C. M.; Feil, D. *J. Chem. Phys.* **1988**, *89*, 4199.
Popelier, P.; Lenstra, A. T. H.; Van Alsenoy, C.; Geise, H. J. *J. Am. Chem. Soc.* **1989**, *111*, 5658.

[54] Saebo, S.; Klewe, B.; Samdal, S. *Chem. Phys. Lett.* **1983**, *97*, 499.

[55] Almlöf, J.; Kvick, A.; Thomas, J. O. *J. Chem. Phys.* **1973**, *59*, 3901.
Bridet, J.; Fliszár, S.; Odiot, S.; Pick, R. *Int. J. Quantum Chem.* **1983**, *24*, 687.
Mombourquette, M. J.; Weil, J. A.; Mezey, P. G. *Can. J. Chem.* **1984**, *62*, 21.
Ángyán, J. G.; Silvi, B. *J. Chem. Phys.* **1987**, *86*, 6957.
Helgaker, T. U.; Klewe, B. *Acta Chem. Scand. A* **1988**, *42*, 269.
Popelier, P.; Lenstra, A. T. H., Van Alsenoy, C.; Geise, H. J. *Acta Chem. Scand. A* **1988**, *42*, 539.
Popelier, P.; Lenstra, A. T. H., Van Alsenoy, C.; Geise, H. *J. Struct. Chem.* **1991**, *2*, 3.
de Dios, A. C.; Pearson, J. G.; Oldfield, E. *Science* **1993**, *260*, 1491.
de Dios, A. C.; Laws, D. D.; Oldfield, E. *J. Am. Chem. Soc.* **1994**, *116*, 7784.
[56] Ferré, N.; Ángyán, J. G. *Chem. Phys. Lett.* **2002**, *356*, 331.
Yatsenko, A. V.; Paseshnichenko, K. A. *Chem. Phys.* **2000**, *262*, 293.
[57] For an example, see:
Leitão, A. A.; Vugman, N. V.; Bielschowsky, C. E. *J. Phys. Chem. A* **2002**, *106*, 9569.
[58] Fülscher, M. P.; Mehler, E. L. *J. Comp. Chem.* **1991**, *12*, 811.
Liao, M.; Zhang, Q. *J. Solid State Chem.* **1999**, *146*, 239.
[59] Peeters, A.; Van Alsenoy, C.; Lenstra, A. T. H.; Geise, H. J. *Int. J. Quantum Chem.* **1993**, *46*, 73.
Peeters, A.; Van Alsenoy, C.; Lenstra, A. T. H.; Geise, H. J. *J. Chem. Phys.* **1995**, *103*, 6608.
Rousseau, B.; Keuleers, R.; Desseyn, H. O.; Geise, H. J.; Van Alsenoy, C. *Chem. Phys. Lett.* **1999**, *302*, 55.
Swerts, B.; Van Droogenbroeck, J.; Peeters, A..; Van Alsenoy, C. *J. Phys. Chem. A* **2002**, *106*, 4245.
[60] Plazanet, M.; Johnson, M. R.; Kearley, G. J. *Physica B* **2000**, *276*, 228.
Orendt, A. M.; Facelli, J. C.; Grant, D. M. *Chem. Phys. Lett.* **1999**, *302*, 499.
Kuklja, M. M.; Kunz, A. B. *J. Apll. Phys.* **1999**, *86*, 4428.
[61] Cai, S. H.; Yu, X. Y.; Chen, Z.; Wan, H. L. *Magn. Reson. Chem.* **2003**, *41*, 902.
[62] Stevens, F.; Vrielinck, H.; Callens, F.; Pauwels, E.; Waroquier, M. *Phys. Rev. B* **2002**, *66*, 134103.
[63] Kölmel, C.; Ewig, C. *J. Phys. Chem. B* **2001**, *105*, 8538.
Mallia, G.; Orlando, R.; Roetti, C.; Ugliengo, P.; Dovesi, R. *Phys. Rev. B* **2001**, *63*, 235102.
[64] For an example, see:

Rydberg, H.; Lundqvist, B. I.; Langreth, D. C.; Dion, M. *Phys. Rev. B* **2000**, *62*, 6997.

[65] Van Alsenoy, C. *J. Comp. Chem.* **1988**, *9*, 620.

[66] Maseras, F.; Morokuma, K. *J. Comp. Chem.* **1995**, *16*, 1170.
Svensson, M.; Humbel, S.; Froese, R. D. J.; Matsubara, T.; Sieber, S.; Morokuma, K. *J. Phys. Chem.* **1996**, *100*, 19357.
Humbel, S.; Sieber, S.; Morokuma, K. *J. Chem. Phys.* **1996**, *105*, 1959.
Matsubara, T.; Sieber, S.; Morokuma, K. *Int. J. Quantum Chem.* **1996**, *60*, 1101.
Dapprich, S.; Komaromi, I.; Byun, K. S.; Morokuma, K.; Frisch, M. J. *J. Mol. Struct. (THEOCHEM)* **1999**, *462*, 1.

[67] Ciccotti, G.; Hoover, W. G. in "*Molecular Dynamics Simulations of Statistical Mechanical Systems*", North-Holland: Amsterdam, **1986**.
Ciccotti, G.; Frenkel, D.; McDonald, I. R. in "*Simulation of Liquids and Solids*", North-Holland: Amsterdam, **1987**.

[68] The CP code employed in this work is under development by Dr. Franco Buda at the Free University of Amsterdam, the Netherlands.

[69] Hutter, J.; Ballone, P.; Bernasconi, M.; Focher, P.; Fois, E.; Goedecker, S.; Parrinello, M.; Tuckermann, M. E., CPMD V3.7. Copyright IBM Corp. 1990-2003, Copyright MPI fuer Festkoerperforschung Stuttgart 1997-2001.

[70] Car, P.; Parrinello, M. *Phys. Rev. Lett.* **1985**, *55*, 2471.

[71] Pauwels, E.; Van Speybroeck, V.; Lahorte, P.; Waroquier, M. *J. Phys. Chem. A* **2001**, *105*, 8794.

[72] Pauwels, E.; Van Speybroeck, V.; Waroquier, M. *Int. J. Quantum. Chem.* **2003**, *91*, 511.

[73] McLaughlin, W. L.; Taylor, D. M. *Appl. Radiat. Isot.* **1996**, *47*, 1.
Regulla, D. F.; Deffner, U. *Appl. Radiat. Isot.* **1982**, *33*, 1101.

[74] Muto, H.; Iwasaki, M. *J. Chem. Phys.* **1973**, *59*, 4821.
Kuroda, S.; Miyagawa, I. *J. Chem. Phys.* **1982**, *76*, 3933.
Itoh, K.; Miyagawa, I. *J. Mol. Struct.* **1988**, *190*, 85.
Vanhaelewyn, G. C. A. M.; Mondelaers, W. K. P. G.; Callens, F. *Radiat. Res.* **1999**, *151*, 590.
Vanhaelewyn, G. C. A. M.; Amira, S. A.; Mondelaers, W. K. P. G.; Callens, F. *Spectrochim. Acta A* **2000**, *56*, 387.

[75] Simmons, J. A. *J. Chem. Phys.* **1962**, *36*, 469.
Arber, J. M.; Sharpe, P. H. G.; Joly, H. A.; Morton, J. R.; Preston, K. F. *Appl. Radiat. Isotop.* **1991**, *42*, 665.
Ciesielski, B.; Wielopolski, L. *Radiat. Res.* **1994**, *140*, 105.

[76] van Roggen, A.; van Roggen, L.; Gordy, W. *Bull. Am. Phys. Soc.* **1956**, *1*, 266.

[77] Miyagawa, I.; Gordy, W. *J. Chem. Phys.* **1960**, *32*, 255.

[78] Miyagawa, I.; Itoh, K. *J. Chem. Phys.* **1962**, *36*, 2157.
Matsuki, K.; Miyagawa, I. *J. Chem. Phys.* **1982**, *76*, 3945.
Pilbrow, J. R.; Hutton, D. R.; Zhong, Y. C.; Noble, C. J.; Song, R. *Appl. Radiat. Isot.* **1996**, *47*, 1257.

[79] Sagstuen, E.; Hole, E. O.; Haugedal, S. R.; Nelson, W. H. *J. Phys. Chem. A* **1997**, *101*, 9763.

[80] Malinen, E.; Hult, E. A.; Hole, E. O.; Sagstuen, E. *Radiat. Res.* **2003**, *159*, 149.
Malinen, E.; Heydari, M. Z.; Sagstuen, E.; Hole, E. O. *Radiat. Res.* **2003**, *159*, 23.
Heydari, M. Z.; Malinen, E.; Hole, E. O.; Sagstuen, E. *J. Phys. Chem. A* **2002**, *106*, 8971.

[81] Bugay, A. A.; Onischuk, V. A.; Petrenko, T. L.; Teslenko, V. V. *Appl. Radiat. Isot.* **2000**, *52*, 1189.

[82] Ban, F.; Wetmore, S. D.; Boyd, R. J. *J. Phys. Chem. A* **1999**, *103*, 4303.

[83] Lahorte, P.; De Proft, F.; Vanhaelewyn, G.; Masschaele, B.; Cauwels, P.; Callens, F.; Geerlings, P.; Mondelaers, W. *J. Phys. Chem. A* **1999**, *103*, 6650.

[84] Tortonda, F. R.; Pascual-Ahuir, J. L.; Silla, E.; Tuñon, I. *Chem. Phys. Lett.* **1996**, *260*, 21.
Tarakeshwar, P.; Manogaran, S. *J. Mol. Struct. (THEOCHEM)* **1997**, *417*, 255.
Rega, N.; Cossi, M.; Barone, V. *J. Am. Chem. Soc.* **1998**, *120*, 5723.
Tortonda, F. R.; Pascual-Ahuir, J.; Silla, E.; Tuñon, I.; Ramirez, F. J. *J. Chem. Phys.* **1998**, *109*, 592.
Sambrano, J. R.; de Sousa, A. R.; Queralt, J. J.; Andres, J.; Longo, E. *Chem. Phys. Lett.* **1998**, *294*, 1.
Gontrani, L.; Mennucci, B.; Tomasi. J. *J. Mol. Struct. (THEOCHEM)* **2000**, *500*, 113.
Nobrega, G. F.; Sambrano, J. R.; de Souza, A. R.; Queralt, J. J.; Longo, E. *J. Mol. Struct. (THEOCHEM)*, **2001**, *544*, 151.

[85] Ding, Y.; Krogh-Jespersen, K. *Chem. Phys. Lett.* **1992**, *199*, 261.

[86] Stepanian, S. G.; Reva, I. D.; Radchenko, E. D.; Adamowicz, L. *J. Phys. Chem. A* **1998**, *102*, 4623.

[87] Barone, V.; Adamo, C.; Grand, A.; Subra, R. *Chem. Phys. Lett.* **1995**, *242*, 351.

[88] Onsager, L. *J. Am. Chem. Soc.* **1936**, *58*, 1486.
Wong, M. W.; Frisch, M. J.; Wiberg, K. B. *J. Am. Chem. Soc.* **1991**, *113*, 4776.
Wong, M. W.; Wiberg, K. B.; Frisch, M. J. *J. Chem. Phys.* **1991**, *95*, 8991.
Wong, M. W.; Wiberg, K. B.; Frisch, M. J. *J. Am. Chem. Soc.* **1992**, *114*, 523.
Wong, M. W.; Wiberg, K. B.; Frisch, M. J. *J. Am. Chem. Soc.* **1992**, *114*, 1645.

[89] Lehmann, M. S.; Koetzle, T. F.; Hamilton, W. C. *J. Am. Chem. Soc.* **1972**, *94*, 2657.

[90] For an example of a reference work, see:
Levine, I. N. in "*Quantum Chemistry*", Prentice Hall: New Jersey, **1991**, Chapter 16.

[91] See for example:
Elsässer, C.; Fähnle, M.; Chan, C. T.; Ho, K. M. *Phys. Rev. B* **1994**, *49*, 13975.
Warren, R. W.; Dunlap, B. I. *Chem. Phys. Lett.* **1996**, *262*, 384.

[92] Wong, M. W.; Radom, L. *J. Phys. Chem. A* **1998**, *102*, 2237.
Parker, C. L.; Cooksy, A. L. *J. Phys. Chem. A* **1998**, *102*, 6186.
Smith, D. M.; Nicolaides, A.; Golding, B. T.; Radom, L. *J. Am. Chem. Soc.* **1998**, *120*, 10223.
Lynch, B. J.; Fast, P. L.; Harris, M.; Truhlar, D. G. *J. Phys. Chem. A* **2000**, *104*, 4811.
Van Speybroeck, V.; Van Neck, D.; Waroquier, M.; Wauters, S.; Saeys, M.; Marin, G. B. *J. Phys. Chem. A* **2000**, *104*, 10939.

[93] The CP code employed in this work is under development by Dr. Franco Buda at the Free University of Amsterdam, the Netherlands.

[94] Car, P.; Parrinello, M. *Phys. Rev. Lett.* **1985**, *55*, 2471.

[95] Stich, I.; Car, R.; Parrinello, M.; Baroni, S. *Phys. Rev. B* **1989**, *39*, 4997.

[96] Ryckaert, J. P.; Ciccotti, G.; Berendsen, H. J. C. *J. Comput. Phys.* **1997**, *23*, 327.

[97] Vanderbilt, D. *Phys. Rev. B* **1990**, *41*, 7892.

[98] Meier, R. J.; van Doremaele, G. H. J.; Iarlori, S.; Buda, F. *J. Am. Chem. Soc.* **1994**, *116*, 7274.
Tarazona, A.; Koglin, E.; Buda, F.; Coussens, B. B.; Renkema, J.; van Heel, S.; Meier, R. J. *J. Phys. Chem. B* **1997**, *101*, 4370.

[99] Batra, R.; Giese, B.; Spichty, M.; Gescheidt, G.; Houk, K. N. *J. Phys. Chem.* **1996**, *100*, 18371.

[100] Pauwels, E.; Van Speybroeck, V.; Waroquier, M. submitted to *J. Phys. Chem. A* **2004**.

[101] Van Speybroeck,V.; Pauwels, E.; Stevens, F.; Callens, F.; Waroquier, M. accepted for publication in *Int. J. Quantum Chem* **2004**.

[102] Gordy, W.; Ard, W. B.; Shields, H. *Proc. N. A. S.* **1955**, *41*, 983.

[103] Combrisson, J.; Uebersfeld, J. *Compt. Rend.* **1954**, *238*, 1397.
Uebersfeld, J.; Erb, E. *Compt. Rend.* **1956**, *243*, 478.

[104] Ghosh, D. K.; Whiffen, D. H. *Mol. Phys.* **1959**, *2*, 285.

[105] Morton, J. R. *J. Am. Chem. Soc.* **1964**, *86*, 2325.

[106] Collins, M. A.; Whiffen, D. H. *Mol. Phys.* **1966**, *10*, 317.

[107] Symons, M. C. R. *J. Chem. Soc.* **1959**, 277.

[108] Box, H. C.; Freund, H. G.; Budzinski, E. E. *J. Am. Chem. Soc.* **1966**, *88*, 658.
Teslenko, V. V.; Gromovoi, Y. S.; Krivenko, V. G. *Mol. Phys.* **1975**, *30*, 425.

[109] Deigen, M. F.; Krivenko, V. G.; Pulatova, M. K.; Ruban, M. A.; Teslenko, V. V.; Kayushin, L. P. *Biofizika* **1973**, *18*, 235.
Iwasaki, M.; Muto, H. *J. Chem. Phys.* **1974**, *61*, 5315.
Nunome, K.; Muto, H.; Toriyama, K.; Iwasaki, M. *J. Chem. Phys.* **1976**, *65*, 3805.
Muto, H.; Iwasaki, M.; Takahashi, Y. *J. Chem. Phys.* **1977**, *66*, 1943.
Smith, C. J.; Poole, C. P.; Farach, H. A. *J. Chem. Phys.* **1981**, *74*, 993.
Syutkin, V. M.; Tolkatchev, V. A. *Chem. Phys. Lett.* **1985**, *122*, 201.
Chis, V.; Brustolon, M.; Morari, C.; Cozar, O.; David, L. *J. Mol. Struct.* **1999**, *483*, 283.

[110] Brustolon, M.; Chis, V.; Maniero, A. L.; Brunel, L.-C. *J. Phys. Chem. A* **1997**, *101*, 4887.

[111] Neta, P.; Fessenden, R. W. *J. Phys. Chem.* **1971**, *75*, 738.

[112] Turecek, F.; Carpenter, F. H. *J. Chem. Soc. Perk. T. 2* **1999**, *11*, 2315.
Turecek, F.; Carpenter, F. H.; Polce, M. J.; Wesdemiotis, C. *J. Am. Chem. Soc.* **1999**, *121*, 7955.

[113] Hedberg, A.; Ehrenberg, A. *J. Chem. Phys.* **1968**, *48*, 4822.

[114] Sanderud, A.; Sagstuen, E. *J. Phys. Chem. B* **1998**, *102*, 9353.

[115] Ding, Y.; Krogh-Jespersen, K. *Chem. Phys. Lett.* **1992**, *199*, 261.

[116] Barone, V.; Adamo, C.; Grand, A.; Subra, R. *Chem. Phys. Lett.* **1995**, *242*, 351.

[117] Ban, F.; Gauld, J. W.; Boyd, R. J. *J. Phys. Chem. A* **2000**, *104*, 5080.

[118] Rega, N.; Cossi, M.; Barone, V. *J. Am. Chem. Soc.* **1998**, *120*, 5723.

[119] Onsager, L. *J. Am. Chem. Soc.* **1936**, *58*, 1486.

Wong, M. W.; Frisch, M. J.; Wiberg, K. B. *J. Am. Chem. Soc.* **1991**, *113*, 4776.

Wong, M. W.; Wiberg, K. B.; Frisch, M. J. *J. Chem. Phys.* **1991**, *95*, 8991.

Wong, M. W.; Wiberg, K. B.; Frisch, M. J. *J. Am. Chem. Soc.* **1992**, *114*, 523.

Wong, M. W.; Wiberg, K. B.; Frisch, M. J. *J. Am. Chem. Soc.* **1992**, *114*, 1645.

[120] Destro, R.; Roversi, P.; Barzaghi, M.; Marsh, R. E. *J. Phys. Chem. A* **2000**, *104*, 1047.

[121] A new version of the CPMD code will shortly become available, that will include the B3LYP functional. For further details, we refer to the website http://www.cpmd.org.

[122] Ghosh, D. K.; Whiffen, D.H. *J. Chem. Soc.* **1960**, 1869.

[123] Sanderud, A. private communication.

[124] CEN/TC 275/WG 8 European Standard EN 1786: Detection of irradiated food containing bone - Method by ESR spectroscopy (**1996**).

[125] CEN/TC 275/WG 8 European Standard EN 1787: Detection of irradiated food containing cellulose by ESR spectroscopy (**2000**).

[126] CEN/TC 275/WG 8 European Standard EN 13708: Detection of irradiated food containing crystalline sugar by ESR spectroscopy (**2001**).

[127] Fattibene, P.; Duckworth, T. L.; Desrosiers, M. F. *Appl. Radiat. Isotopes* **1996**, *47*, 1375.

Nakajima, T.; Otsuki, T.; Hara, H.; Nishiwaki, Y.; Matsuoka, M. *Radiat. Prot. Dosim.* **1990**, *34*, 303.

Tchen, A.; Greenstock, C. L.; Trivedi, A. *Radiat. Prot. Dosim.* **1993**, *46*, 119.

[128] Bardsley, J.; Baugh, P. J.; Phillips, G. O. *J. Chem. Soc. Perkin Trans. 2* **1975**, 614.

Gilbert, B. C.; King, D. M.; Thomas, C. B. *J. Chem. Soc. Perkin Trans. 2* **1983**, *5*, 675.

Triolet, J.; Thiery, C.; Agnel, J. P.; Battesti, C.; Raffi, J.; Vincent, P. *Free Radical Res. Commun.* **1990**, *10*, 57.

Triolet, J.; Thiery, C.; Battesti, C.; Agnel, J. P.; Raffi, J.; Vincent, P. *J. Chim. Phys. Phys-Chim. Biol.* **1991**, *88*, 1237.

Triolet, J.; Raffi, J.; Agnel, J. P.; Battesti, C.; Thiery, C.; Vincent, P. *Magn. Reson. Chem.* **1992**, *30*, 1051.

Triolet, J.; Thiery, C.; Agnel, J. P.; Battesti, C.; Raffi, J.; Vincent, P. *Free Radical Res. Commun.* **1992**, *16*, 183.

[129] Derouane, E. G.; Vedrine, J. C. *Chem. Phys. Lett.* **1974**, *29*, 222.

[130] Shields, H.; Hamrick, P. *J. Chem. Phys.* **1962**, *37*, 202.
Lomaglio, G. C. R. *Seances Acad. Sci. B* **1967**, *264*, 1637.

[131] Gräslund, A.; Löfroth, G. *Acta Chem. Scand. B* **1975**, *29*, 475.

[132] Sagstuen, E.; Lund, A.; Awadelkarim, O.; Lindgren, M.; Westerling, J. *J. Phys. Chem.* **1986**, *90*, 5584.
Vanhaelewyn, G.; Sadlo, J.; Callens, F.; Mondelaers, W.; De Frenne, D.; Matthys, P. *Appl. Radiat. Isotopes* **2000**, *52*, 1221.

[133] Wetmore, S. D.; Boyd, R. J.; Eriksson, L. A. *J. Phys. Chem. B* **1998**, *102*, 7674.
Close, D. M. *Radiat. Res.* **1997**, *147*, 663.
Debije, M. G.; Bernhard, W. A. *Radiat. Res.* **2001**, *155*, 687.

[134] Becker, D.; Sevilla, M. D. *Adv. Radiat. Biol.* **1993**, *17*, 121.

[135] von Sonntag, C. *The Chemical Basis of Radiation Biology*, Taylor and Francis: New York, 1987.

[136] Becker, D.; Bryant-Friedrich, A.; Trzasko, C.; Sevilla, M. D. *Radiat. Res.* **2003**, *160*, 174.

[137] Pauwels, E.; Lahorte, P.; Vanhaelewyn, G.; Callens, F.; De Proft, F.; Geerlings, P.; Waroquier, M. *J. Phys. Chem. A* **2002**, *106*, 12340.

[138] Vanhaelewyn, G.; Lahorte, P.; De Proft, F.; Mondelaers, W.; Geerlings, P.; Callens, F. *Phys. Chem. Chem. Phys.* **2001**, *3*, 1729.

[139] Lahorte, P. in “*Quantum chemical study of EPR spectroscopic properties in radiation-induced bioradicals*”, PhD thesis **2000-2001**, unpublished

[140] Takagi, S.; Jeffrey, G. A. *Acta Cryst. B* **1977**, *33*, 3510.
Takagi, S.; Jeffrey, G. A. *Acta Cryst. B* **1978**, *34*, 1048.

[141] Yoshimi, T. “*DFT-berekeningen op suikerradicalen: de invloed van de kristalomgeving*”, master thesis **2001-2002**, unpublished.

[142] Pauwels, E.; Van Speybroeck, V.; Vanhaelewyn, G.; Callens, F.; Waroquier, M. accepted for publication in *Int. J. Quantum Chem.* **2004**.

[143] Madden, K. P.; Bernhard, W. A. *J. Phys. Chem. US* **1982**, *86*, 4033.

[144] Madden, K. P.; Bernhard, W. A. *J. Phys. Chem. US* **1979**, *83*, 2643.

[145] Brown, G. M.; Levy, H. A. *Acta Cryst. B* **1979**, *35*, 656.

[146] Vanhaelewyn, G.; Jansen, B.; Pauwels, E.; Sagstuen, E.; Waroquier, M.; Callens, F. *J. Phys. Chem. A* **2004**, *108*, 3308.

[147] Kim, S. H.; Rosenstein, R. D. *Acta Cryst.* **1967**, *22*, 648.
Nordenson, S.; Takagi, S.; Jeffrey, A. *Acta Cryst. B* **1979**, *35*, 1005.